ÉCOLE DE TECHNOLOGIE SUPÉRIEURE
UNIVERSITÉ DU QUÉBEC

MASTER'S THESIS
PRESENTED TO
ÉCOLE DE TECHNOLOGIE SUPÉRIEURE

IN PARTIAL FULFILLMENT OF THE REQUIREMENTS FOR
MASTER'S DEGREE IN MECHANICAL ENGINEERING
M. Eng.

BY
Matin TIREH DAST

FINITE ELEMENT MODELING OF THE HEAT SOURCE DURING WELDING OF 415 STEEL JOINTS (13%CR-4% NI) WITH THE ROBOTIC FCAW

MONTREAL, JULY 29 2015

BOARD OF EXAMINERS

THIS THESIS HAS BEEN EVALUATED

BY THE FOLLOWING BOARD OF EXAMINERS

Mr. Henri Champliaud, Thesis Supervisor
Mechanical Engineering department at École de technologie supérieure

Mr. Jacques Lanteigne, Thesis Co-supervisor
Researcher – Institut de recherche d'Hydro-Québec

Mr. Mohammad Jahazi , Chair, Board of Examiners
Mechanical Engineering department at École de technologie supérieure

Mr. Ngan Van Lê, Member of the jury
Mechanical Engineering department at École de technologie supérieure

Mr. Jean-Benoît Lévesque, External Evaluator
Researcher - Institut de recherche d'Hydro-Québec

THIS THESIS WAS PRENSENTED AND DEFENDED

IN THE PRESENCE OF A BOARD OF EXAMINERS AND THE PUBLIC

JUNE 22 2015

AT ÉCOLE DE TECHNOLOGIE SUPÉRIEURE

ACKNOWLEDGMENTS

First and foremost, I would like to sincerely thank my supervisors, Professors Henri Champliaud and Jacques Lanteigne for giving me the opportunity to work on this project. I want to express my gratitude for their inspiration, support and patience.

Besides my advisors, I would take this opportunity to thank to all my colleagues at IREQ (Institut de recherche d'Hydro-Québec). Special thank goes to Jean-Benoit Lévesque for his great support towards cracking the obstacles, Daniel Paquet for all those instructive discussions, Carlo Baillargeon for his assistance and guidance in experimental procedures.

This project would not have been undertaken without the financial support of CReFARRE and IREQ.

I would like to thank all my friends who have supported me over the last few years in Montreal.

I am also grateful to my boyfriend, Shervin, who has supported me through good and bad times.

Last but most importantly, I would like to express my gratitude to my family, to my sister for her genuine love and support in every single moment of my life, to my parents, who supported me unconditionally.

MODÉLISATION PAR ÉLÉMENT FINIS DE LA SOURCE DE CHALEUR LORS DU SOUDAGE DE L'ACIER 415 (13%CR-4%NI) AVEC LE PROCÉDÉ ROBOTISÉ FCAW

Matin TIREH DAST

RÉSUMÉ

Les contraintes résiduelles constituent le problème le plus connu durant le processus de soudage en industrie, et a pour conséquence de réduire la durabilité de la partie soudée. Le modèle d'éléments finis peut prédire la distribution thermique le long de la pièce, induite par le processus de soudage et la distribution de contraintes résiduelles. Plusieurs approches ont été développées pour simuler la variation de température et des contraintes résiduelles pendant le soudage.

Malgré tous les efforts faits par les universitaires pour prédire le champ thermique dans le processus de soudage, le manque de précision reste encore un problème dans le voisinage de la zone affectée par la chaleur. Cette étude est menée dans le but de précisément calculer le champ thermique dans et au voisinage de la zone affectée par la chaleur en utilisant la méthode des éléments finis. Un code thermique d'éléments finis, développé à l'IREQ, est utilisé afin d'obtenir le champ thermique au sein du soudage multi-passe. Ce code a été modifié, afin de considérer les propriétés thermiques de l'Acier inoxydable martensitique 415 comme matériau de base, pour obtenir une simulation plus fiable de la transmission de chaleur. Ensuite, la capacité du code à prédire la distribution de température est évaluée aux nœuds donnés sur la plaque, pendant le soudage multi-passe, dans le but de la comparez avec les données expérimentales. Dans notre simulation, le mouvement d'une source de chaleur de Goldak est appliqué dans le code pour prendre en compte l'énergie thermique induite dans la pièce par le processus de soudage. De plus, la méthode naissance des éléments est employée pour modéliser le dépôt du métal d'apport. Afin de relier les résultats expérimentaux et analytiques, 20 thermocouples sont installés sur la plaque pendant le processus du soudage, dans le but de mesurer le changement de la température.

Une cartographie de la micro-dureté et de la microstructure des sections transversales sont analysées pour comparer avec la configuration prédite de la zone affectée par la chaleur. Enfin, la micro-dureté de petits spécimens est comparée à la mesure expérimentale de l'histoire thermique, simulée analytiquement, sur le spécimen, à la micro-dureté d'un nœud pour la même position sur la pièce.

La comparaison des résultats obtenus par le code et expérimentaux, avec les thermocouples, du profil thermique montrent que le modèle peut prédire justement le profil de température durant les processus de chauffage et de refroidissement pour le processus de soudage multi-passe. L'erreur moyenne calculée est inférieure à 10°C pour les trois passes de soudure.

Mots-Clés: Soudage multi-passe, Éléments finis, Acier 415

FINITE ELEMENT MODELING OF THE HEAT SOURCE DURING WELDING OF STEEL 415 (13%CR-4% NI) WITH THE ROBOTIC FCAW

Matin TIREH DAST

ABSTRACT

Residual stress is one of the most known problems through welding process in industry, as it caused the durability of welded part to reduce. Finite element analysis can predict the thermal distribution induced by welding process along the part, thereby calculating the residual stress. Several approaches have been developed to simulate the temperature variation and the residual stresses during welding.

Despite all the efforts carried out by scholars to predict the temperature field within the welding processes, the lack of accuracy still remains an issue in the neighbouring of the heat-affected zone. This study was intended to precisely calculate the thermal field within and in the vicinity of the heat affected zone through multi-pass welding using finite element analysis. A developed thermal finite element code at IREQ (Institut de recherche d'Hydro-Québec) was employed to calculate the thermal field within the multi-pass welding process. The program was modified to consider thermal properties of martensitic stainless steel 415 as the base material in order to offer a more reliable simulation of the heat transfer. Then, the capability of the program to predict the temperature distribution was evaluated at given nodes in the plate during multi-pass welding through comparison with the experimentally collected data. Goldak's moving heat source was applied in the program to consider the induced thermal energy to the part by the welding process into the simulation. Furthermore, the element birth and death method were employed to model the deposition of the filler metal. In order to link the experimental and the numerical results, 20 thermocouples were installed in the plate, and thereby the temperature variation was monitored during welding process.

The map of micro hardness and microstructure of cross-sections were analyzed to compare with the predicted configuration of the heat-affected zone in the simulation. At last in this study, the micro-hardness of small specimens were compared upon experimentally reproduction of the analytically simulated thermal history on the specimen, to the micro-hardness of the node of the welded part model corresponding to this thermal history.

The comparison of the calculated and the experimentally measured thermal profile through the thermocouples demonstrate that the model can fairly predict the temperature profile during the heating and the cooling processes for the multi-pass welding process. The calculated average error was less than 10°C within the three pass welding, which is negligible compared to welding temperature.

Keywords: Multi-pass welding, Finite element analysis, Stainless steel 415

TABLE OF CONTENTS

LIST OF TABLES

Page

LIST OF FIGURES

Page

INTRODUCTION

Welding is a popular industrial process to join materials in countless applications, such as manufacturing of turbines, pipelines, and shipbuilding [1, 2]. Residual stress and distortion have been known as the most common problems in the welding process severely influencing the mechanical properties of the welded parts. These have been assigned to the temperature gradient induced by the welding process and the subsequent phase transformation across the weld zone [3]. This leads to the reduction of welded part durability due to the deterioration of geometrical arrangement derived from the residual stress and distortion [4].The analysis of residual stress becomes even more complicated through the multi pass welding compared to single pass, due to the relatively large thickness of plates, which are conducted to the multi pass welding [5].

Several numerical models have been suggested to predict the residual stress and the distortion induced through the multiple thermal cycles on the welded parts during the multi pass welding process [6,7,8]. However, it has been demonstrated that an accurate analysis of the thermal cycle is required to predict the residual stress of welding [7]. This is crucial to consider heat input from a moving heat source, temperature dependency of material properties and metal deposition to develop a realistic model to simulate the welding process [8].

Goldak's heat source for welding simulation exhibited certain advances in welding simulation, as a moving heat source through the Gaussian distribution inside a double ellipsoidal volume [9]. It is of great interest to ascertain thermal dependency of material properties, such as specific heat and conductivity coefficients, to perform a reliable simulation of a welding process [10]. Furthermore, the deposition of filler metal should be involved into the simulation. Subsequently, numerous methods have been offered to consider the contribution of filler metal to the modeling procedure, such as element birth technique and element movement technique [5, 11].

In this research, the element birth technique was applied through activation and deactivation of the elements. The main objective of this study is to accurately calculate the thermal field within and in the vicinity of the heat affected zone for the multi-pass flux cored arc welding of stainless steel 415.

A three-dimensional finite element model was used to address this objective, including measured specific heat and conductivity coefficient of stainless steel 415. Subsequently, the predicted data through the simulation was compared to the experimental results.

This thesis is divided into five chapters:

The first chapter presents a comprehensive literature review on any subject, which one might run across within the main objective, consists of welding, moving heat source, deposition of filler metal in modeling and thermal properties of stainless steel 415. The second chapter explains the research main objective, specific objectives and hypothesis. The third chapter includes the methodology and the experiments in order to validate the predicted results of the simulation. In the fourth chapter, the thermal history associated with welding process was simulated using the finite element model. This chapter elaborates the heat source model, deposition of filler metal and characterizing of thermal properties in this research. The fifth chapter presents the collected results, analysis of data, and their discussion. The major conclusions of this work are summarized in chapter 6, followed by the recommendations for the future works.

CHAPTER 1

LITERATURE REVIEW

1.1 Welding

Welding is a widely used industrial process for joining metal parts [1]. Welding has been extensively employed in manufacturing process of pipelines, heavy buildings, ships and turbines. Various welding processes have been developed based on the manner of applying heat and type of equipment [2]. A heat source is always required to provide high temperature to melt the material during a welding process [3]. It has been shown that the heat source could be either an arc, electron beam, laser beam or a torch. Generally, the molten weld metal is protected from atmospheric oxidation using a shield gas.

Tungsten inert gas arc welding (TIG), gas metal arc welding (GMAW), flux cored arc welding (FCAW) are the most popular welding processes, with their own advantages and limitations. Therefore, the appropriate welding process is chosen depending on the application and the alloys to be joined.

1.1.1 Gas tungsten arc welding

The use of filler metal rod is optional in gas tungsten arc welding (GTAW) or tungsten inert gas welding (TIG) [4]. Nevertheless, this process can be conducted without filler metal while, the base metal provides the weld material. This process is gas shield protected using inert gasses such as Helium, Argon or a mixture of them [5]. Less deposition rate, lower productivity have been recognized as the disadvantages of gas tungsten arc welding compared to gas metal arc welding [3]. GTAW is usually recommended for the welding of thin plates of steel and other alloys such as aluminum and magnesium. The welding quality is influenced by welding current, arc length, wire-feeding rate, and welding speed [4].

1.1.2 Gas metal arc welding

Gas metal arc welding (GMAW) process is one of the most popular welding processes owing to its low cost and high productivity. Continuous wire feeding allows to have long weld beads without stopping the process [6].

GMAW is a complex process, consisting in several interrelated parameters, that influence the quality of welding joint such as welding current, welding voltage, travel speed and arc efficiency [7]. In this process, an electric arc is established between a consumable wire electrode and the work piece to be joined. The heat generated by the electric arc melts the filler metal and the work piece surface. The arc and the molten pool are protected from the atmosphere and oxidation by an external gas [8]. Running of the external shielding gas is considered as a major disadvantage during the GMAW process.

1.1.3 Flux-cored arc welding

The equipment, which is employed in flux-cored arc welding (FCAW), is similar to that of the gas metal arc welding [2]. Flux-cored arc welding can be either gas shielded or self-shielded [9]. The self-shielded welding is a major privilege of FCAW compared to the other processes, arising from a flux in the core of the filler wire [2]. A continuous filler metal is used in this process. It is striking that, the high deposition rate as well as the high productivity of FCAW caused the operator to enable performing the arc welding with less experience and skill, compared to that of GMAW. This can be also assumed as an advantage of FCAW process [10, 11]. This is worth noticing that GTAW process leads to obtain a more efficient impact strength and fracture toughness than FCAW and GMAW, despite the low productivity rate [12].

1.2 Residual stresses

During a welding process, heating and cooling result in a development of thermal stresses in the plate, due to an inhomogeneous temperature distribution along the plate [13]. It is noteworthy, that the stresses can be either residual or temporary. The temporary stresses are formed at the specific time scale during the welding and they release afterward. However, the residual stresses remain in the welded plate at ambient temperature [14].

Welding stresses are subdivided into two main categories based on the nature of the stresses; thermal stresses and phase transformation stresses [15]. These two categories will be explained in section 1.2.1 and 1.2.2.

1.2.1 Thermal stresses

Thermal stresses derive from a non-uniform temperature distribution during welding process. Regions nearby the weld arc are heated up to thousand centigrade degrees, then cooling down to room temperature. Temperature variations result in the development of thermal stress, arising from a volumetric change. The thermal expansion of the region nearby the weld arc is impeded through the surrounded cold metal. Therefore, a compressive stress is generated in the vicinity of the weld metal. The developed compressive longitudinal stress enhances with an increase of the temperatures up to the yield stress of material. In the cooling process, the temperature of work piece reaches ambient temperature. The surrounding cold metal restrains the welded area from retraction and consequently, at the end of cooling, the residual stresses will be tensile in the weld region.

Subsequent to cooling when theses stresses have reached or overcome the yield stress, the residual stress is developed [16]. It is noteworthy that stress can be affected by the micro-structural changes in the materials. Phase transformation causes expansion in martensitic filler metal during cooling. Therefore, a transition from tensile stress to compression stress occurs due to expansion of filler metal [14].

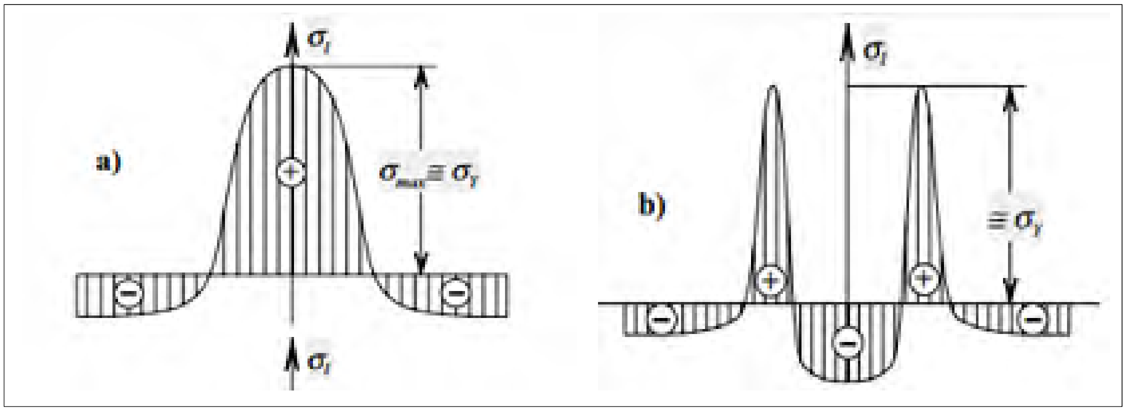

Figure 1.1 Example of longitudinal stress a) mild steel b) high alloy steel with martensitic filler metal
Taken from Pilipenko (2001)

1.2.2 Phase transformation stress

Residual stress can be also caused by the phase transformation during welding [16]. Phase transformation occurs in the plate as the welded plate is cooled down to room temperature, corresponding to the chemical composition of the plate. The phase transformation also leads to a volume change in the work piece.

A martensitic stainless steel 13% Cr- 4%Ni is employed as the main material in this study. This material is known as a martensitic stainless steel owing to its microstructure, which includes a martensite (M) phase. The microstructure depends on the applied thermal cycle, during the welding process and the post weld heat treatment (PWHT). Nearly 100% fresh martensite is obtained in the absence of a post weld heat treatment in 13%Cr-4%Ni. PWHT will give rise to tempered martensite (around 85%) and a mixture of retained austenite and reformed austenite (around 15%) [17].

The face centered cubic lattice structure of austenite (γ) transforms during cooling into a martensitic structure with body center tetragonal crystalline lattice. This phase transformation causes a distortion of the material through an increase of the volume and subsequently a decrease of the density of the material. The confinement of the carbon in the martensite microstructure decreases the mobility of the dislocations in the crystal structure, improving the hardness compared to the austenite phase [18]. Figure 1.2 shows a schematic of martensite and austenite lattices.

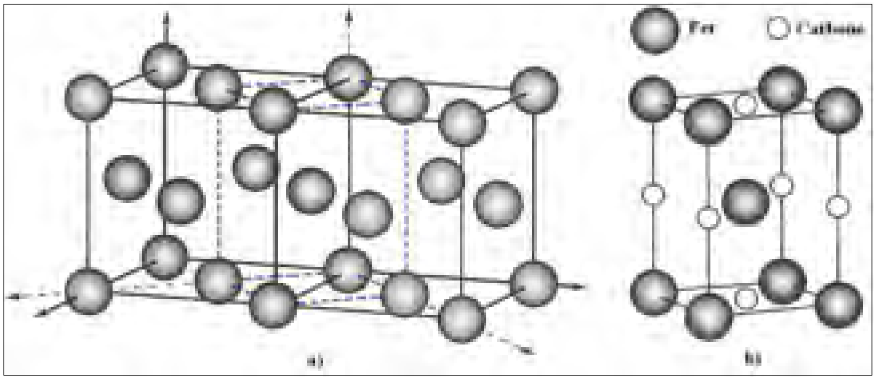

Figure 1.2 a) forming a body centered tetragonal lattice from two face centered cubic network b) martensite network
Taken from Porter (1992)

It was discussed that the volume changes following the transformation of the austenite structure to martensite, elevating the internal stresses. A shear stress is imposed to the structure of the austenite, due to this transformation. The shear stress and the variation of volume are shown schematically during transformation in the Figure 1.3.

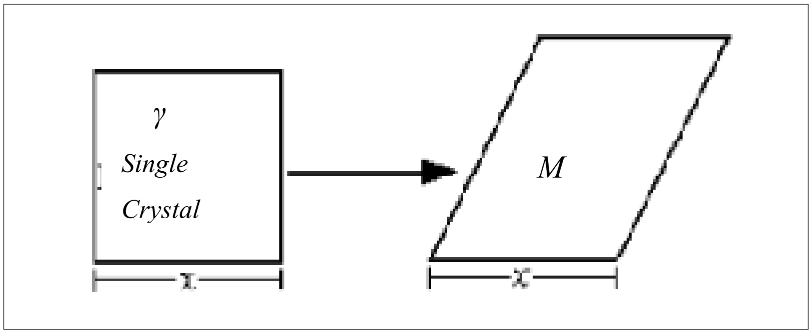

Figure 1.3 Schematic picture of shear stress and increased volume of atomic lattice during the transformation γ → M
Taken from Bhadeshia (2002)

Consequently, inhomogeneous heating of the area nearby the arc welding resulted in the development of various microstructures in the heat affected zone, in comparison with the rest of work piece i.e. base metal. This creates a continuous variation of the microstructure, as illustrated in Figure 1.4.

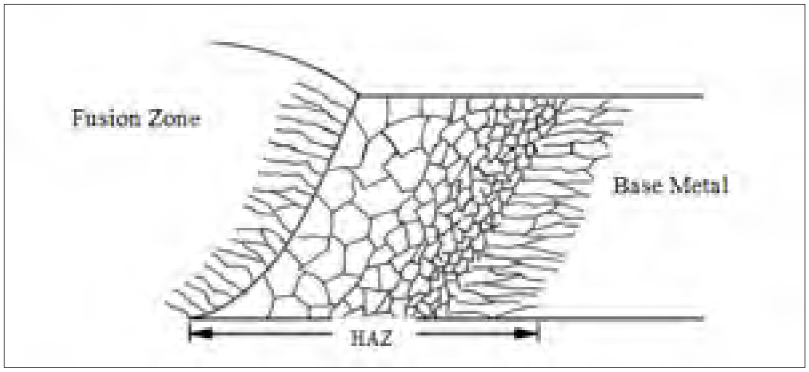

Figure 1.4 Microstructure variation diagram in the heat affected zone
Taken from Bhadeshia (2002) [20]

1.3 Finite element method

Finite element method (FEM) is a numerical technique to solve partial differential equations. The whole object is divided into several structural elements in finite element method. Therefore, a complex geometry is simplified into simpler subdivisions. In this case, the equation of changes is derived individually for a distinct subdivision to predict the objective variation. Subsequently, the predicted value, in the distinct subdivisions, is extended to the whole geometry. Finite Element method is a well-known numerical approach, providing an accurate prediction of thermal and stress variations and their combination.

1.3.1 Modeling of filler material

The addition of filler metal is an important issue in the welding model. Several authors such as Krutz [1] did not deposit the filler metal in their model to reduce the complexity of simulation. It leads to some level of errors in the welding simulation since the surface of the model was changed due to deposition of a new material. Furthermore, as filler metal starts melting, heat loss through radiation becomes predominant at the high temperatures (>1000

°C) compared to heat loss due to convection. This is well-established that the convection mechanism of heat transfer is dominant at low temperature (< 200°C). Therefore, a comprehensive heat loss modeling is required. However, more accurate outcome is envisaged as the deposit filler metal applied in element birth technique and element movement technique, rather than no-deposit techniques [21, 22].

1.3.1.1 Element birth technique

The element birth technique is the most conducted method for deposition of the filler material [23, 24]. This method is based on deactivation and activation of the filler metal elements. These groups of elements are initially deactivated by assigning the physical properties of the ambient air to them. In order to simulate a weld pass deposition, the physical properties of the weld pool are gradually altered to the filler metal material properties and deactivated elements are progressively activated as the heat source moves along the welding line [22, 23]. The combination of element birth and lumped (grouped) weld passes technique has been suggested by Hong to reduce the simulation time and complexity of multi-pass welding [23]. A minimum of two weld passes are considered as a layer in lumped pass technique in simulation of multi-pass welding ([25] cited by[23]).

1.3.1.2 Element movement technique

Fanous [22] pointed out a new technique for metal deposition using element movement instead of the addition of material. In this method, the elements corresponding to filler metal are discerned from the elements of the base metal through gap elements. At first, the properties of gap elements are evaluated to be close to zero. Then, the length of the gap elements decreases as the heat source moves. This process continues up to the superposition of the nodes of welding elements and the base material (Figure 1.5). This new technique takes less time to complete in 3D analysis, in comparison with “element birth” method despite of its lower accuracy [21].

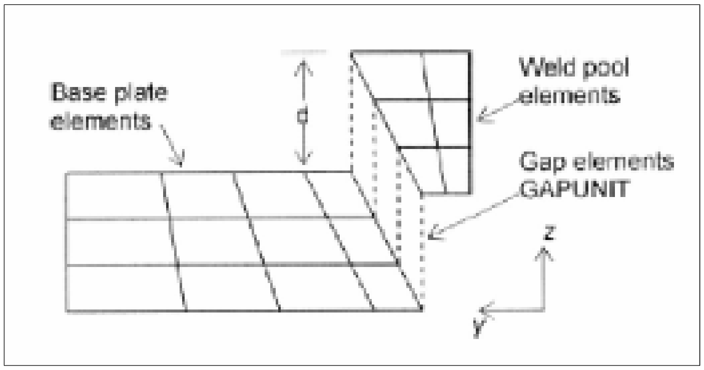

Figure 1.5 Element movement technique
Taken from Fanous (2003)

1.3.2 Heat input determination

The net heat input is calculated by equation 1.1, for all arc welding methods [26]

$$Q_{net} = \eta\, Q_{arc} \tag{1.1}$$

Where Q_{net}, Q_{arc} and η stand for the net heat input, the arc energy and the heat transfer efficiency, respectively.

Also arc energy can be calculated from equations 1.2 and 1.3 [26, 27].

$$Q_{arc} = E.I \tag{1.2}$$

Then

$$Q_{net} = \eta . E.I \tag{1.3}$$

Where E and I stand for the arc voltage and the arc current, respectively. Voltage and current of arc are the parameters of arc used in experimental process. Heat transfer efficiency η depends on the welding procedure and it reflects energy loss through the arc by radiation

[26]. Energy loss takes place mostly through radiation [28] and heat transfer efficiency is estimated between 70% -80% for FCAW process [26].

1.3.3 Heat transfer

During a welding process, the region nearby the arc is heated to a high temperature which is above the melting point of the filler metal, subsequently cooling down with a great rate. The heat transfer occurs through the plate and between the plate and environment during welding. Heat transfer mechanisms are conduction, convection and radiation. Heat is initially transferred through conduction and convection at the surface afterward the contribution of radiation to the heat transfer increases as filler metal begins to melt [29].

1.3.4 Thermal properties of material

Thermal properties of material, such as specific heat and thermal conductivity, are influenced by temperature and phase transformations [30]. Significant errors can emerge in the welding simulations if the variation of the physical properties is neglected. To avoid this problem, the temperature dependency of the material properties are applied to the simulation of the welding process [31].

1.3.4.1 Specific heat

Specific heat is a temperature dependent property, defined as the amount of heat needed to raise the temperature of a certain quantity of material [32]. A comprehensive literature review revealed that the specific heat values were not reported for stainless steel 415 [33-35]. A reasonable approach to tackle this issue could be to use the specific heat of similar materials [27]. Therefore, the specific heats of five steels that have similar chemical compositions were collected and then interpolated to approximate the specific heat of stainless steel 415. The compositions of five similar materials are presented in Table 1.1.

Table 1.1 Chemical compositions of CA6NM and five similar materials

Material	CA6NM	1	2	3	4	5
C	0.060	0.130	0.160	0.150	0.270	0.130
Ni	3,5/4,5	0.140	2.500	6,0/8,0	0.200	0.140
Cr	11,5/14	12.950	16.500	16,0/18,0	13.690	12.950
Mo	0,4/1					
Mn	1.000	0.025	0.200	2max	0.280	0.250
Si	1.000				0.180	
P	0.040					0.180
S	0.030					0.024
Cu	0.500					

Specific heat values of the mentioned materials versus temperature are plotted in Figure 1.6. As it can be observed, phase transformation of martensite → austenite in stainless steel can affect the specific heat in a temperature range of 600℃ to 800℃, whereas, the literature did not provide comprehensive information about the amount of heat specific for this phase transformation. Furthermore, the literature only provides data for increasing of the temperature. No information can be found for the austenitized material before developing of the martensite during the cooling. Therefore, further experimental investigations are needed to measure specific heat of stainless steel 415. The solid-state phase transformation was not observed within the DSC thermograph of material # 1 to 3 due to the absence of the exothermic. However, as it is shown in Figure 1.6, specific heat of material # 4 and 5 exhibited a change during the phase transformation. In this study, specific heat was measured distinctly during heating and cooling. This is discussed in section 4.5.

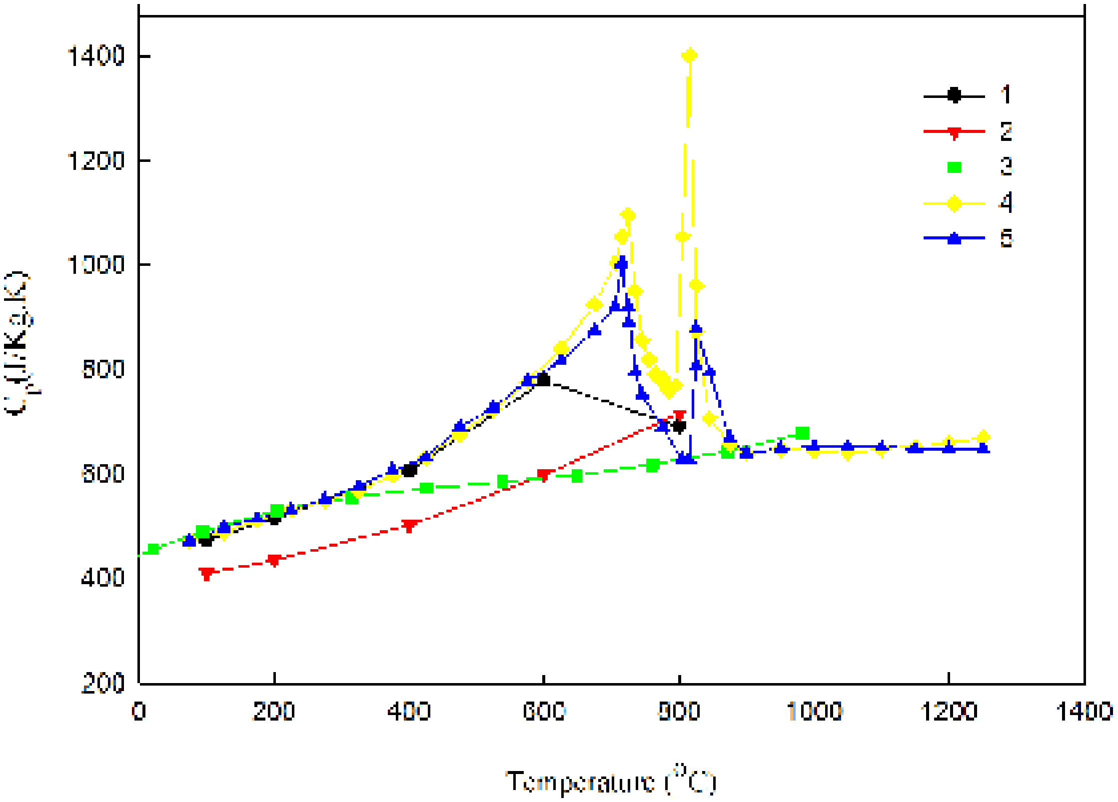

Figure 1.6 Specific heat vs. temperature for five different materials during heating

1.3.4.2 Thermal conductivity

Thermal conductivity is a material property characterizing the ability of material to conduct heat. Thermal conductivities of the materials in Table 1.1 are presented in Figure 1.7.

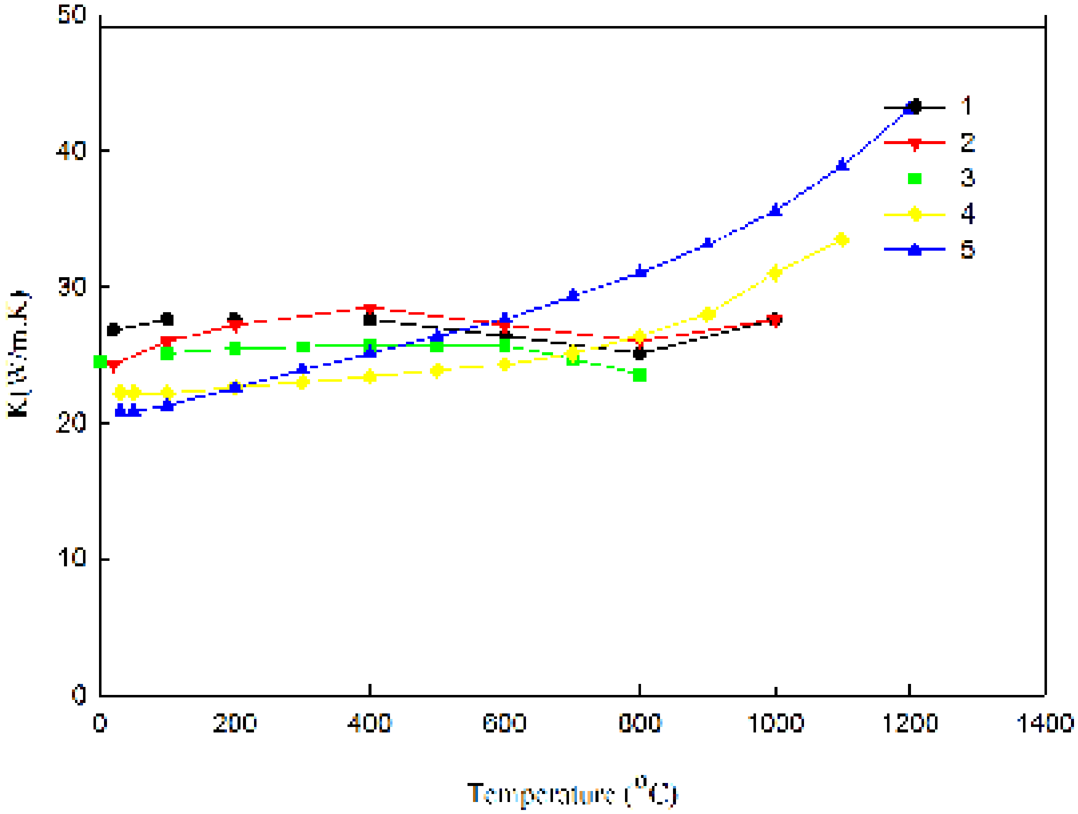

Figure 1.7 Thermal conductivity vs. temperature for five different materials

1.3.4.3 Convective heat transfer

Convective heat transfer coefficient is not a material property. Here, convection occurs between the metal surface and environment owing to the molecular mobility of the surrounding air. The convective heat transfer is estimated using equation (1.4) [29, 32].

$$q = h(T - T_s) \tag{1.4}$$

Where q, h, T and T_s stand for heat flux (W/m^2), convection heat transfer coefficient (W/m^2°C), material temperature (°C) and ambient temperature, respectively. The convective heat transfer coefficient, h, is considered to be 8 (W/m^2°C) according to the experimental work carried out at IREQ [36].

1.3.4.4 Radiation heat transfer

Radiation is the energy transported at the speed of light in the absence of material. Radiation depends on the forth power of the absolute temperature[37]. The contribution of the radiation heat transfer is assumed noticeable at high temperatures (1.5).

$$q = \sigma . \varepsilon . (T^4 - T_s^4) \tag{1.5}$$

Where q, σ, $\mathcal{E}$, T and T_s stand for heat flux (W/m^2), Stefan-Boltzmann constant ($5.67e - 8\ W/m^2K^4$), emissivity, material temperature (K) and ambient temperature (K).

Here, emissivity depends on surface oxidation and temperature variations [32]. The emissivity of steel 415 is presented in Figure 1.8.

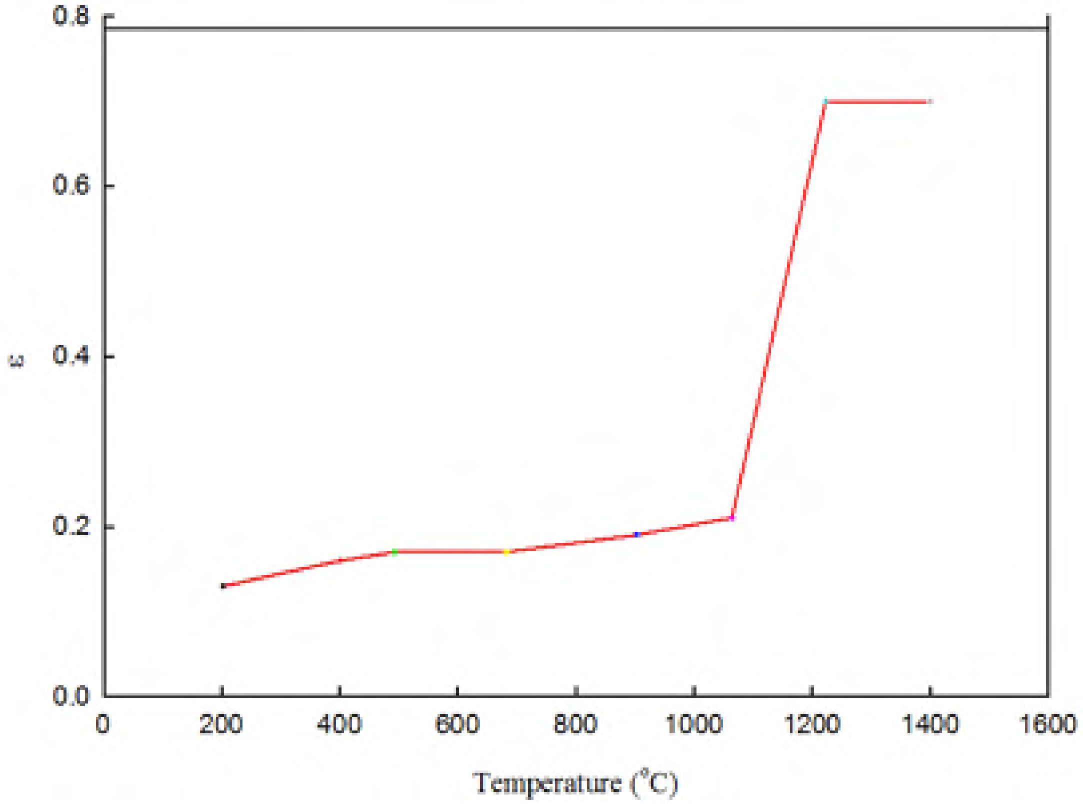

Figure 1.8 Variation of emissivity coefficient for stainless steel 415 as a function of maximum temperature

1.4 Heat source models

The input heat from welding causes a complex thermal cycle in the weldment. Subsequently, thermal stresses and microstructural variations result in the residual stress and distortion of the final product [7]. Residual stress and microstructural changes are predicted based on the welding thermal cycle. Moreover, the predicted thermal cycle provides information on the geometry of the heat-affected zone, the cooling rate as well as the weld penetration [38]. It has been demonstrated that a deep understanding of the thermal cycle is strongly required, particularly in a region nearby the heat source. Consequently, an accurate heat source model is needed in order to predict the exact temperature distributions [39]. To date, various methods have been developed to predict a thermal cycle precisely.

1.4.1 Rosenthal's analytical model

Rosenthal developed a mathematical theory of heat distribution using the conventional heat transfer differential equation. He presented a method for predicting cooling time and its rate in welding Rosenthal's analysis [40]. This method exhibited an analytical solution for the temperature distribution considering the heat source as a point, line, or plane [39]. Rosenthal's method is still the most popular analytical method to evaluate the thermal history of welds [41].

Rosenthal's theory was the first mathematical theory, capable of predicting the heat distribution of a moving heat source [42], However it was derived from a single formula [40]. For the first time, Rosenthal solution makes it possible to consider welding parameters such as current, voltage and welding speed in the analysis [31, 43]. Equation (1.6) presents Rosenthal's equation for temperature distribution around the moving sources of a two dimensional problem [44, 45].

$$(T - T_0) = \frac{Q}{2\pi K R} e^{\frac{-V(W+R)}{2\alpha}} \tag{1.6}$$

Where, T, T_0, Q, K, α, V, R and W stand for temperature at a point (K), original plate temperature (K), heat input per unit time (W), thermal conductivity ($W.m^{-1}.K^{-1}$), thermal diffusity ($m^2.s^{-1}$), welding speed ($m.s^{-1}$), distance to heat source (m) and distance along the weld center line (m), respectively.

Temperature field is predicted accurately far from the heat source using either point heat source, line heat source or surface heat source. However, this solution cannot predict temperature in or in the vicinity of fusion zone (FZ) and heat affected zone (HAZ). Furthermore, it is not either suitable for complex welding assemblies. This is a major drawback of this method, since this approach could not consider temperature-dependent properties of material as well as real boundary condition. Furthermore, the flux and temperature at the heat source have been assumed infinite in this model. These assumptions lead to considerable errors in estimation of temperature in comparison with experiments. In addition, Rosenthal's solution provides no information related to the weld pool [6, 39, 42-44, 46-50].

1.4.2 Numerical methods

Inherent assumptions made to derive the equations are known as a limitation of analytical approaches. Numerical models have been developed to overcome the limitations of analytical methods. Finite element methods (FEM) is among the most widely used numerical methods. The FEM can manage analyses of complex geometries and temperature dependant material properties [24].

Rykalin [51] applied Fourier's heat flow theory to a moving heat source to solve one and two dimensional heat flow problems using a numerical method [49]. The long running time had restricted the application of this model. Furthermore, either limited number of elements or coarse elements have been considered to overcome this drawback. This may sacrifice the accuracy of prediction in 1951 (cited by [43, 45]).

Westby prevailed the restriction of elements size and number as well as constant thermal properties by high performance computer in 1968 [43, 45].

Paley presented a computer program based on Westby work capable of analyzing non-rectangular cross sections such as V and U grooves using a non-uniform mesh.

Paley and Hibbert [43] and Westby [52] assumed that energy was distributed with a constant power density throughout the melted zone to reflect the digging effect of the arc with a finite difference analyses [6, 46, 47, 49, 53-55]. In 1975, Paley and Hibbert published a paper in which they described their model taking variable thermal properties into account and predicting actual weld shape and thermal history of the welding process [43]. However, in 1984 Goldak et al. demonstrated that this model was not able to predict complex geometry of welding pool because of using finite difference analyses. Furthermore, it did not present any criteria to predict the length of molten pool [6, 46, 49].

1.4.2.1 Disc model

Gaussian distribution of flux deposited on the surface of the work piece was proposed by Pavelic [56] for the first time. This distribution is described by equation (1.7).

$$q(r) = q_0 e^{-Cr^2} \tag{1.7}$$

Where $q(r)$, q_0, C and r stand for the surface flux at radius r (W/m^2), the maximum flux at the center of the heat source (W/m^2), the distribution width coefficient (m^{-2}) and the radial distance from the center of the heat source (m), respectively.

In disc model, the input energy is considered as the total energy of arc (Q). The uniform flux and C can be correlated where, q_0 is distributed in a circular disk, of diameter $d = {}^{2}/_{\sqrt{C}}$,

$$Q = q_0 \frac{\pi d^2}{4} \tag{1.8}$$

$$q_0 = \frac{QC}{\pi} \tag{1.9}$$

$$q(r) = \frac{QC}{\pi} e^{-cr^2} \tag{1.10}$$

C is related to the width of the heat source. Therefore, a more concentrated source such as laser beam shows a smaller diameter d and a larger C. Variation of C is shown in Figure 1.9.

In order to measure the value of C, it is assumed that the imposed heat flux in the circle with radius(r_d) is equal to 5% of the maximum heat flux at the center of heat source.

$$q(r_d) = q_0 e^{-Cr_d^2} \tag{1.11}$$

$$0.05q_0 = q_{0e^{-Cr_d^2}} \tag{1.12}$$

$$C = \frac{Ln(20)}{r_d^2} \approx \frac{3}{r_d^2} \tag{1.13}$$

Pavelic's distributed heat source model was explored by Krutz [1]. He applied a two dimensional finite element analysis to determine a relationship between temperature and time. He considered thermal conductivity and specific heat as a function of temperature and assumed a Gaussian distribution for heat flux.

It has been shown that the heat source model derived by Pavelic [56] and Krutz [1] can represent a precise prediction of temperature distribution. However, the arc penetration is as small as GTA welding since the contribution of arc digging action has been neglected in this model [6]. Thus, it increases the errors related to high power density sources, such as laser beam or electron beam.

Eagar and Tsai [44] presented a dimensionless solution for a traveling Gaussian distributed heat source in 1983. The same simplifications as Rosenthal's theory were assumed such as constant thermal properties and quasi-steady state semi-infinite. Eagar and Tsai successfully provided a first estimation of weld pool geometry based on fundamentals of heat transfer [39, 44]. Literally, this model demonstrated an accurate functional relation between both process and material parameters. Nonetheless, it cannot predict weld penetration accurately. Eagar and Tsai proposed to employ Myers [57] temperature enhancement factor to obtain better results.

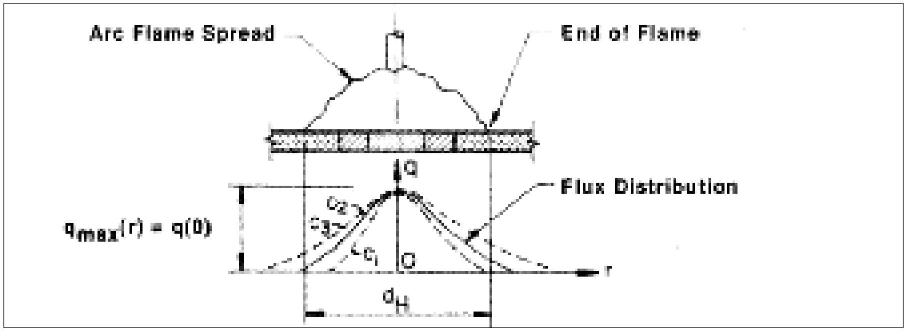

Figure 1.9 Schematic of disc model
Taken from Pavelic (1969)

1.4.2.2 Hemispherical power density distribution

As it was described earlier in 1.4.2.1, disc model is not an appropriate approach for the heat source with a high power density since the arc transports the heat under the surface. Hemispherical Gaussian distribution of power density has been suggested as a more realistic model for these types of heat sources. Hemispherical distribution is determined by equation (1.14) [46].

$$q(x,y,z) = \frac{6\sqrt{3}Q}{C^3\pi\sqrt{\pi}} e^{-3x^2/C^2} e^{-3Y^2/C^2} e^{-3z^2/C^2} \tag{1.14}$$

Where q, C and c stand for power density (W/m^3), distribution width coefficient (m^{-2}) and the radius of hemispher (m), respectively.

As a matter of fact, hemispherical heat source solves the problem of ignoring the arc penetration. Nevertheless, it shows some limitations in modeling of a heat source. It assumes heat source embedded in a spherical symmetry. Ellipsoidal volume source is proposed to figure out this limitation.

1.4.2.3 Double-ellipsoidal Model

All the aforementioned methods suffer from several serious restrictions. Goldak [6] initially proposed a semi-ellipsoidal heat source with Gaussian heat flux distribution. This model is more precise allowing controlling the arc penetration. Heat Gaussian distribution is determined inside the volume by the equation (1.15)

$$q(x,y,z) = q_0 e^{-Ax^2} e^{-By^2} e^{-Cz^2} \tag{1.15}$$

Where q_0 is maximum value of the power density at the center of ellipsoid and A, B and C are heat flow distribution coefficients.

The energy of arc is equal to the heat flux Q since heat flow is distributed inside the semi-ellipsoid volume. Heat flux is calculated by multiplying the voltage and current by a coefficient of 2. The coefficient is related to the overall applied energy in a half ellipsoid. Q is calculated as follow:

$$2Q = 2\eta VI = 8\int_0^\infty \int_0^\infty \int_0^\infty q(x,y,z)dxdydz = 8q_0(\frac{\sqrt{\pi}}{2\sqrt{A}})(\frac{\sqrt{\pi}}{2\sqrt{B}})(\frac{\sqrt{\pi}}{2\sqrt{C}}) \tag{1.16}$$

In the equation (1.16), η, V and I represent heat source efficiency, the voltage of the arc and current of the arc, respectively.

$$q_0 = \frac{2Q\sqrt{ABC}}{\pi\sqrt{\pi}} \tag{1.17}$$

It is speculated that power density on the surface of the ellipsoid with the spreading parameter of arc (a, b, c) is $0.05q_0$ [46]. So:

$$A = \frac{3}{a^2}, \qquad B = \frac{3}{b^2}, \qquad C = \frac{3}{c^2}$$

The experimental findings showed that the ellipsoid model could not precisely predict temperature gradient in front of the heat source. Double ellipsoidal source is suggested to overcome this limitation. The front half of the source is the quadrant of one ellipsoidal source, and the rear half is the quadrant of another ellipsoid. In this model, f_r and f_f are the rear fraction and front fraction of heat respectively, deposited in the front and rear quadrants, where $f_r + f_f = 2$. The power density distribution inside the front quadrant is:

$$q(x,y,z,t) = \frac{6\sqrt{3}f_f Q}{abc\pi\sqrt{\pi}} e^{-3x^2/a^2} * e^{-3Y^2/b^2} * e^{-3(z+v(\tau-t))/c^2} \tag{1.18}$$

The power density distribution is calculated in the rear quadrant similar to the front quadrant.

$$q(x,y,z,t) = \frac{6\sqrt{3}f_r Q}{abc\pi\sqrt{\pi}} e^{-3x^2/a^2} * e^{-3Y^2/b^2} * e^{-3(z+v(\tau-t))/c^2} \tag{1.19}$$

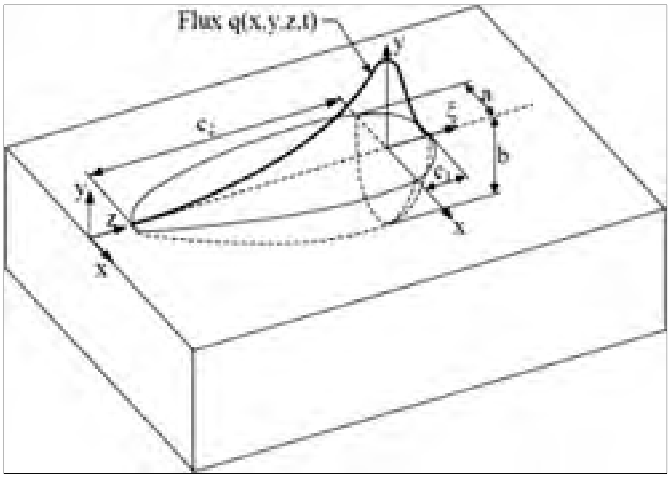

Figure 1.10 Double ellipsoid heat source configuration
Taken from Goldak (1984)

Recently, a research has been carried out on thermal analysis of the heat source. Lundbäck [58] suggested to combine conical heat source and ellipsoid heat source. This model is consistent for a welding with high penetration such as electron beam welding. This model can accurately predict the penetration, as it was demonstrated by the comparison of finite element results with the experiments. Nevertheless, full penetration has not been achieved in the finite element model. Hong proposed a combination of body heat power and surface heat flux [23] for modeling of gas metal arc welding. It is mentioned as a simple model for asymmetric multi pass welding. Hong's model has also been used for modeling of gas metal arc welding. The ratio of surface heat flux and body heat flux has been adjusted to achieve an accurate representation of fusion zone. In Hong's study [23], surface heat flux was assumed to be in the form of Gaussian thermal distribution while the body heat flux was assumed to be constant.

A split heat source has been suggested by Wahab [38] to consider the heat transfer through convective movement of the liquid weld pool. This fact was neglected in Goldak model. Wahab [38] developed two conduction models as a 2D model and a 3D finite element model. In his approach, the total heat is split into several parts and distributed. One part of the heat input arises from the inclusion of a deposited weld bead. Then, the remaining heat is divided into arc and drop sources. The part related to the arc is an ellipsoidal volume at the plate surface. The second part, from the drop is distributed below the plate surface at a depth proportional to the arc current. The result illustrates that the simple 2-section model and the 3D finite element conductive heat transfer models adequately simulate the gas metal arc welding.

In another study, Ohm divided the weld bead into N parts and sequentially deposited in time [59]. In this finite element analyses, the elements of weld bead have been activated at a specific time point, and then material properties and temperature were changed to bead material values. A constant temperature ($T_{solidus}$) is applied to all nodes. Thermal analysis is solved for the first weld bead then the temperature load is removed from the first weld bead. In final step, same process is frequently run for each N in a weld bead. This numerical model is used for a single bead weld on a steel plate. This approach revealed better results on prediction of residual stresses compared to the moving heat source while moving heat source can estimate the temperature distribution more precisely. However, the estimation of residual stress is strongly interconnected to the prediction of the temperature distribution. In other words, more precise temperature distribution is calculated, the more accurate residual stress.

1.5 Stainless steel 415

The application of chromium steel is limited, owing to the brittleness of precipitated chromium carbide at the grain boundaries during welding, poor weld ability and consequently its cold cracking sensitivity [60].

Stainless steel 415 is a modified chromium steel via the reduction of the percentage of carbon and the addition of 3-4 % Ni to improve corrosion resistance and toughness [60, 61]. Therefore, 13 % Cr and 4 %Ni are distinguished in stainless steel 415 to improve its resistance to corrosion, cavitation corrosion, excellent weld ability and high strength [17, 62, 63]. Manufacturing of hydraulic turbine is one application of this stainless steel [17, 61, 64].

Weldability is an important feature of stainless steel 415. Nonetheless, a crack-free weld is acquired in thick plate using a matched filler metal (12% Cr, 4-6% Ni) and preheating [60].

Delta ferrite forms during solidification of stainless steel 415 according to the phase diagram as it is presented in Figure 1.11. The phase transformation of delta ferrite to austenite occurs in a temperature range of 1200˚C-1300 ˚C. Subsequently, austenite (f.c.c) transformed into martensite (b.c.c) during the cooling step with a volumetric change. However, the final structure of stainless steel can contain delta ferrite in a range of 1-4 %.

The combination of strength and toughness is optimized through austenitizing and tempering of stainless steel [65]. Toughness increases by tempering heat treatment in a range of 600℃ - 620℃ accompanied with a decrease in the hardness of this material [60]. The microstructure of stainless steel is lath martensite after austenitizing. The variation of the volume fraction of the reformed austenite formation can occur in the tempering temperature range of 570℃-680℃ using different holding times. The formation of reformed austenite only depends on temperature as the tempering temperature reaches 680℃ [65].

Reformed austenite is distributed inter lath boundaries along the martensite. Accordingly, high toughness of stainless steel after tempering is due to distribution of reformed austenite. Reformed austenite causes softening through transformation to martensite near crack. Transformation of austenite (fcc) into martensite (bcc) absorbs energy and closes cracks by volume expansion resulted from phase transformation. Therefore, reformed austenite is thermally stable but not mechanically. Nevertheless, austenite transforms into martensite at even a low stress [17, 62, 66]

The reformed austenite is stable as it cools down to room temperature from the tempering temperature between 600℃-630℃. However, the reformed austenite produced in a tempering temperature above 630℃ is partially transformed to martensite during cooling [67]. It has been shown that the reformed austenite is enriched with Ni atoms and the segregation of Ni makes reformed austenite stable. An increase of temperature improves amount of reformed austenite decreasing the concentration of Ni [65]. It makes the reformed austenite less stable due to diminution amount of Ni atom [62].

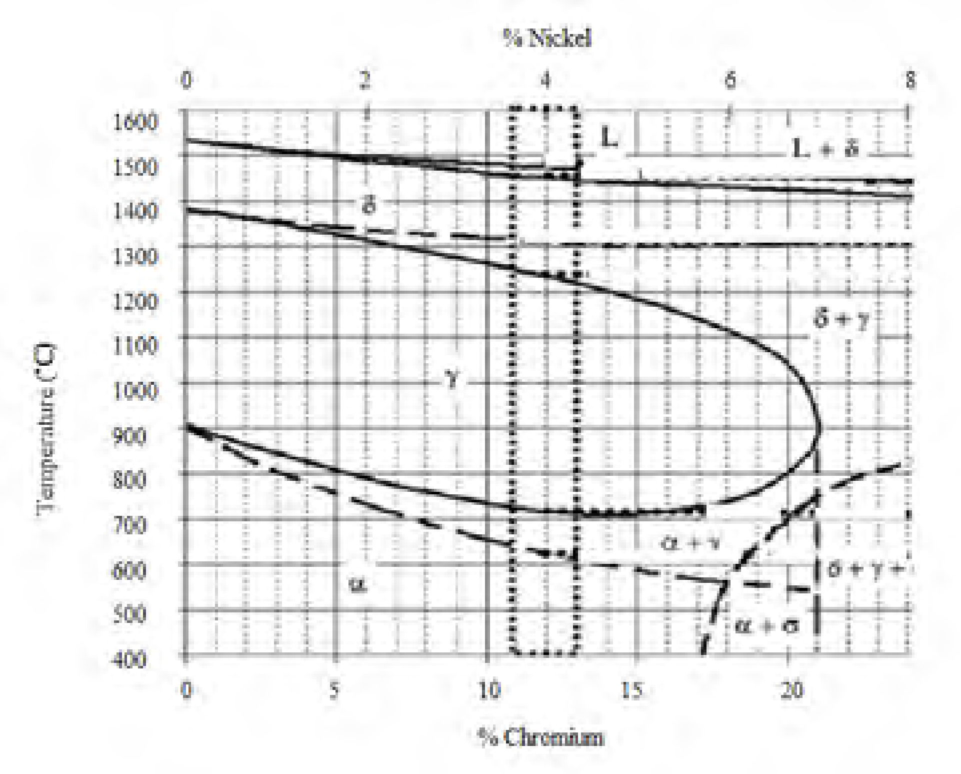

Figure 1.11 Phase diagram of stainless steel 415
Taken from Folkhard (1988)

1.6 Summary

In this chapter, a comprehensive literature review is carried out on base material's properties and different moving heat source models. This review would broaden our understanding of welding process and would help us to calculate the thermal field for multi-pass welding accurate.

CHAPTER 2

RESEARCH OBJECTIVES AND HYPOTHESIS

Welding is a useful industrial process in turbine manufacturing and shipbuilding. As the arc crosses the weld assembly, residual stresses are produced because of the very steep thermal gradient and subsequent phase transformation. A precise modeling of the welding can predict welding outcome without requiring costly pre-production. Furthermore, it provides a comprehensive understanding of the welding process [38]

Finite element method has shown promising results in the modeling of welding as it can be seen in the numerous published studies [21, 27]. Among different approaches, most studies used Goldak's moving heat source model to simulate temperature gradient. Moreover, element birth and death method has been suggested to consider deposition of filler metal in simulations.

After reviewing the literature relevant to the stainless steel 415, it is recognized that there is a lack of knowledge about thermal properties of this material such as specific heat and conductivity coefficient in different temperatures. Improvements in the understanding of the aforementioned material properties would lead to a significant contribution into simulation of welding process. Furthermore, a FEM which is able to predict the temperature contour with time within or nearby the heat affected zone is of high interest.

The global objective of this research is to accurately calculate the thermal field within and in the vicinity of the heat affected zone for multi-pass flux cored arc welding of stainless steel 415.

This study presents a three passes 410Nimo FCAW welding, performed on a triangular groove made on a AISI415 plate. Simulations were carried out using the thermal finite element code developed at IREQ to calculate the thermal field for multi-pass welding.

The research hypotheses of this thesis are:

- Temperature variations with time can be predicted within the heat-affected zone during a multi-pass welding process, using the developed FEM, with an average envisaged error less than 10% for the maximum temperature.

- Thermal conductivity and specific heat are considered as a function of temperature and a Gaussian distributed heat flux is used to determine temperature time relationships in this research.

To address the main objective, three specific objectives are defined:
Objective 1: To measure the specific heat and conductivity coefficients for stainless steel 415 by an experimental set up

Objective 2: To validate calculated thermal distributions during multi-pass welding through experimental investigation

Objective 3: To validate the finite element model by comparing the microstructure in small samples after applying the resultant thermal history from simulations with the experimental results.

CHAPTER 3

METHODOLOGY AND EXPERIMENTAL CHARACTERIZATION

3.1 Introduction

The purpose of this thesis is to develop a model to precisely predict the temperature profile nearby a heat source such as a welding zone. In order to validate the calculated results, temperature profiles were recorded through thermo-couples installed at different locations of a plate, during a multi-pass welding process. Furthermore, heat-affected zones (HAZ) were investigated using micro hardness measurements and micro-structural analysis of the plate cross section. Finally, experimental reproduction of thermal profile estimated at some nodes of the welded plate FEM model was carried out on base material samples, and micro hardness of these samples were compared to that of the actual welded plate at the same location. In this section, the characteristics of the installation, instrumentation and welding process are described.

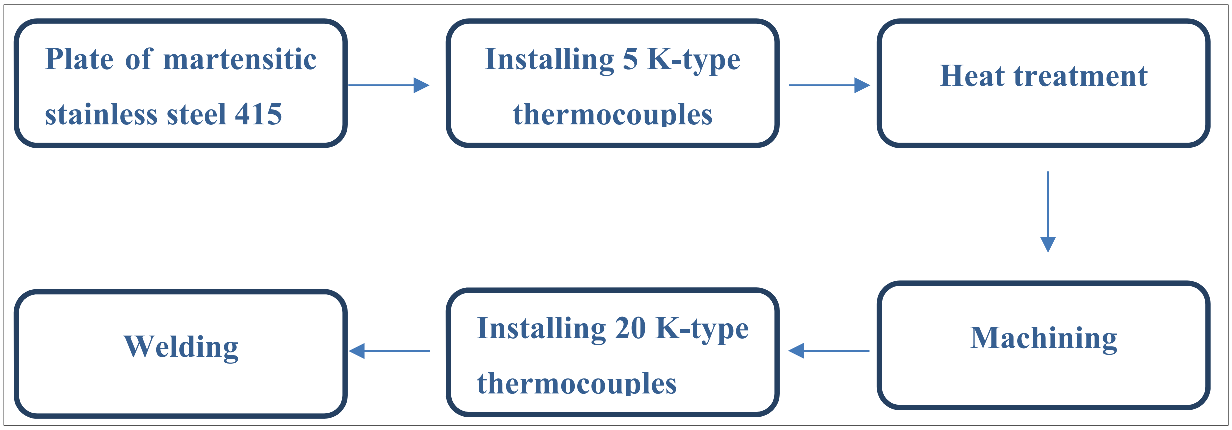

Figure 3.1 Experimental strategy

3.2 Base material

Heat treatment was required in order to prepare the plate for welding process as the first step of the experimental procedure. Initially, the property of the base material should be investigated. Martensitic stainless steel 13%Cr–4% Ni was employed as the base material in this study. This type of stainless steel contains Chromium, Nickel and a low percentage of Carbon. Furthermore, It is well-known for the high weld quality, high mechanical strength, and excellent corrosion resistance [17] as described in 1.5. The chemical composition of the base material and filler metal are presented in Table 3.1.

Table 3.1 Chemical composition of the base material and filler metal(wt%)

	% C	% S	% P	% Si	% Mn	% Cr	% Ni	% Mo	% V	% Cu
Base metal	0.017	0.001	0.015	0.47	0.8	12.0	4.2	0.58	0.02	0.17
Filler metal	0.02	0.005	0.01	0.38	0.4	12.4	3.9	0.52	0.02	0.05

The term “Martensitic” is designated to the base metal since the microstructure is mainly included martensite. Austenite, martensite and α-ferrite are the main components of martensitic stainless steel. The amount of austenite and martensite depends on the applied heat treatment. Moreover, the amount of α-ferrite was detected to be up to 5 vol % in the base material [17, 64].

3.3 Heat treatment

Heat treatment consists of heating a metal to a specific temperature, holding it at that temperature for a required time, and finally cooling it to ambient temperature [69]. Heat treatment has been recommended to optimise physical and mechanical properties of the materials and to obtain a desired metallurgical structure [70]. The structure of a metal can be influenced by maximum temperature, holding time, rate of cooling and heating [69]. Ultimate structure of a metal can be predicted by its phase diagram [70]. Annealing, normalizing, aging, stress relieving, quenching and tempering are different types of heat treatment. One of the most important applications of the heat treatment process is to soften and reduce the hardening and to increase the toughness as it is employed in this study.

Various temperatures and holding times were selected to heat treat small specimens of base material. Hardness measurement and microstructure analysis were performed to achieve minimum hardness in the absence of grain growth. The key aspect of using heat treatment was to reduce as much as possible the hardness of the base material in order to produce the largest range of microhardness in the heat affected zone of the welded plate. That would increase the resolution of the hardness map since the hardness would remain low in the base metal far from the weld and very high in the weld metal and HAZ, since austenization and martensitic transformation is attended to occur. Heat treatment steps to achieve this lowest hardness of the base metal are described in section 3.4 with more details.

3.4 Heat treatment steps

The hardness for the base material (prior to the heat treatment) was measured to be 26 HRC, respectively. This as-received condition from the steel supplier Carlson was achieved by austenitizing at 1050°C, followed by a double tempering heat treatment.

Samples, from the base metal, were prepared with a square cross section (38.1×38.1 mm^2) and a height of 76.2 mm. These were subjected to various heat treatment procedures.

The samples were put in a furnace and held for a sufficient period at a desired temperature. Subsequently, the samples were taken out and cooled rapidly to room temperature.

Heat treatment sequences and resulting hardness are presented in Table 3.2. After each step, hardness of the heat-treated samples were measured with a load of 150 kg on the Rockwell-C scale.

Heat treatments for samples #1 and #2 were triple tempering heat treatments added to the previous double-tempering given by the supplier at similar temperatures. As expected, the amount of reformed austenite has probably increased since the hardness reduced from 28.3 HRC to 21.8 HRC (WP #1).

The purpose of heat treatments for samples #3 to #8 was to re-austenitize the steel, therefore completely removing the initial Carlson metallurgical condition (which was unknown to us) and impose our own double-tempering heat treatment directly from the as-quenched condition. The selected heat treatment (last line of the table) was a re-austenitizing at a slightly lower temperature (because the capacity of the available furnace to hold the whole plate could not exceed 1000°C), with a 24 h sustained second tempering heat treatment at 630°C. An average hardness of 20.1 HRC +/- 1.2 was obtained out of 10 measurements on the plate.

Table 3.2 Summary of heat treatment temperature, time and hardness for different tests

Samples #	First heat treatment			Second heat treatment			Third heat treatment		
	Temperature (˚C)	Time (Hour)	Hardness (HRC)	Temperature (˚C)	Time (Hour)	Hardness (HRC)	Temperature (˚C)	Time (Hour)	Hardness (HRC)
1	670	2	26	610	2	23.9	630	17	21.8
2	670	2	26	610	2	23.9	650	8	23.8
3	1050	1	31.9	670	2	25.1	630	2	22.2
4	1050	1	31.9	670	2	25.1	630	8	21.6
5	1050	1	31.9	690	2	27.9	630	2	23.1
6	1050	1	31.9	690	2	27.9	630	8	22.8
7	1050	1	31.9	630	4	23.8			
8	1050	1	31.9	660	2	26	625	23	22.6
9	950	1.02	-	670	2.38	-	630	24.38	20.3

The plate was made of martensitic stainless steel 13%Cr-4%Ni with length, width and thickness of 472 ×254×38.1 mm^3 respectively.

As discussed in the last section, the plate was heat treated in a three-step sequence, as described below

In the first step, the plate was held in the oven at 950 ℃ for 1.03h in order to austenitize the plate in depth. The set point of the furnace was adjusted to obtain 950°C as the average response of five K-type thermocouples tack welded on the plate, as indicated in Figure 3.2.

Figure 3.2 Installation of five k-type thermocouples to control the temperature inside oven during heat treatments
(This picture was taken after a first heat treatment, where the plate was rapidly cooled. The plate was reheated and slowly cooled in the furnace)

This temperature was maintained for 1.03 h. The plate was then slowly cooled down in the furnace. Phase transformation within the steps was predicted from equilibrium diagram of stainless steel 13%Cr-4%Ni.

Austenitization occurred in the plate at 950℃ according to phase diagram (Figure 1.11). The austenite to martensite ($\gamma \rightarrow M$) phase transformation took place as the plate was being cooled down. Consequently, the microstructure of base material was transformed entirely into fresh martensite as it was described in chapter 1 [18, 66].

In the second step, the plate was held at 670°C for 2.38 h, subsequently being cooled down to room temperature. The microstructure then consists of a mixture of austenite and martensite at room temperature after tempering at 670℃. According to the phase diagram, austenite appears in the microstructure at a rough temperature range of 620 ℃ to 720°C.

Consequently, fresh martensite was converted to a tempered martensite and reformed austenite at this stage. It is consistent with the micro hardness measurements as the measured value for hardness decreased to 25.1 HRC.

The third step included holding the plate at 630°C for 24 h, then cooling it down to room temperature. The ultimate microstructure of the base material was tempered martensite and more reformed austenite compared to the second step. The plate hardness was measured to be 20.3 HRC.

No grain growth was confirmed by microstructural investigations using optical microscopy. Figure 3.3 revealed no grain growth occurred during the heat treatment of sample 9. Figure 3.3-a and Figure 3.3-b indicated the microstructure of martensitic stainless steel prior to the heat treatment and after 3-step of heat treatment, respectively. The micrograph exhibited that the grain size was the same for both samples.

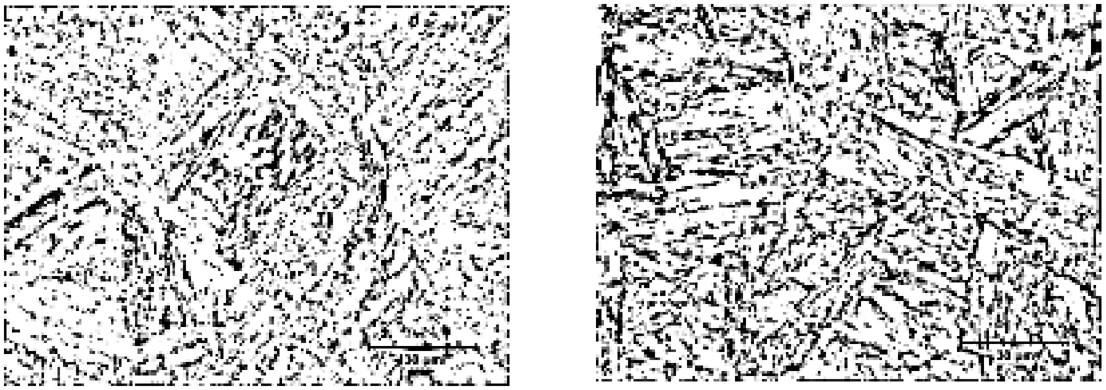

(a) (b)

Figure 3.3 The microstructure of martensitic stainless steel a) before heat treatment b) after heat treatment

3.5 Preparation of plate and V-groove

In this process, the heat-treated plate was ground to its final shape and size. The V groove preparation has been suggested for welding of thick plates similar to the one employed in this study [2].

Schematic picture of the plate and v-groove is presented in Figure 3.4. The z-axis designated to the longitudinal direction of the plate. The x and y-axes were assigned to the transverse and normal directions, respectively. V–groove was prepared along the z direction for multi-pass welding.

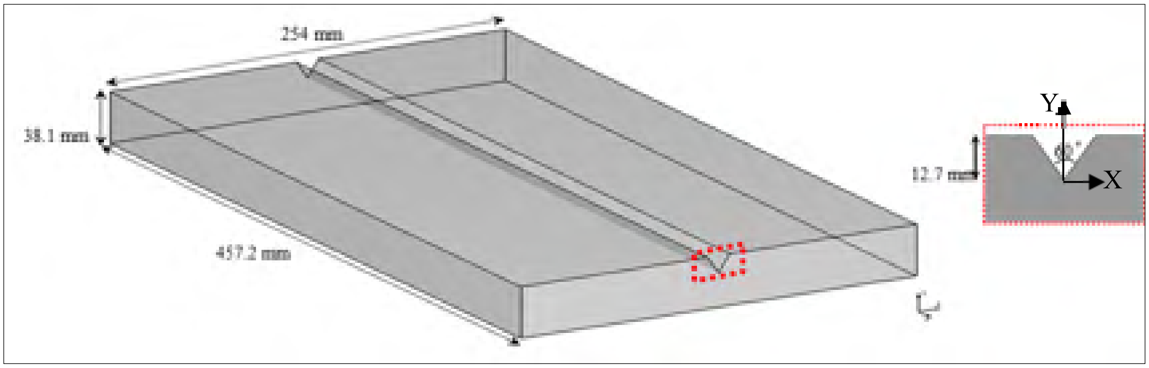

Figure 3.4 Schematic picture of machined plate and V-groove

Moreover, eighteen 3.26 mm diameter holes were drilled in the inferior surface of the plate to embed thermocouples. As shown in Figure 3.5, these holes were located in the x-z plane at different depth.

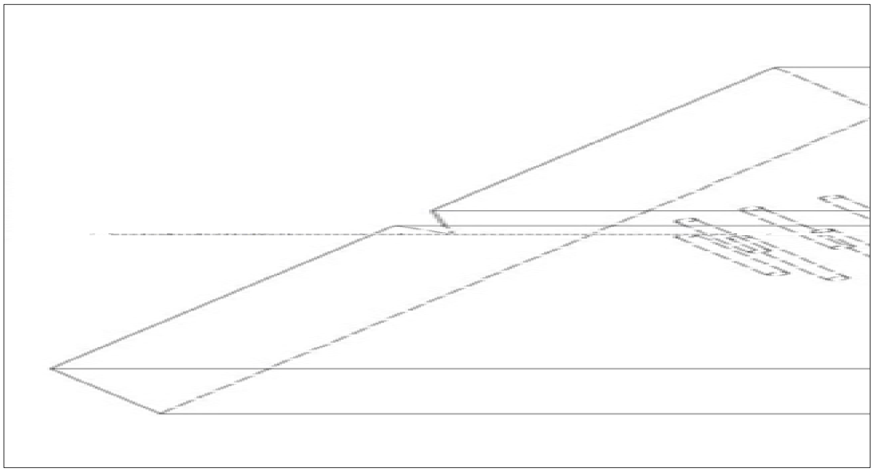

Figure 3.5 Schematic picture of v-preparation and drilled holes

The locations of thermocouples were determined through simulations. Critical temperatures for base material specimens were set within a temperature range between 620℃ and 720℃ corresponding to the phase transformation (M→ γ) occuring in the base metal. Consequently, it is expected that the microstructure and hardness of base material will change in HAZ. The 18 thermocouples were installed in the processed holes, in the lower face of the plate. Furthermore, two more thermocouples were installed on the upper surface of the plate to monitor temperature far from the welding zone.

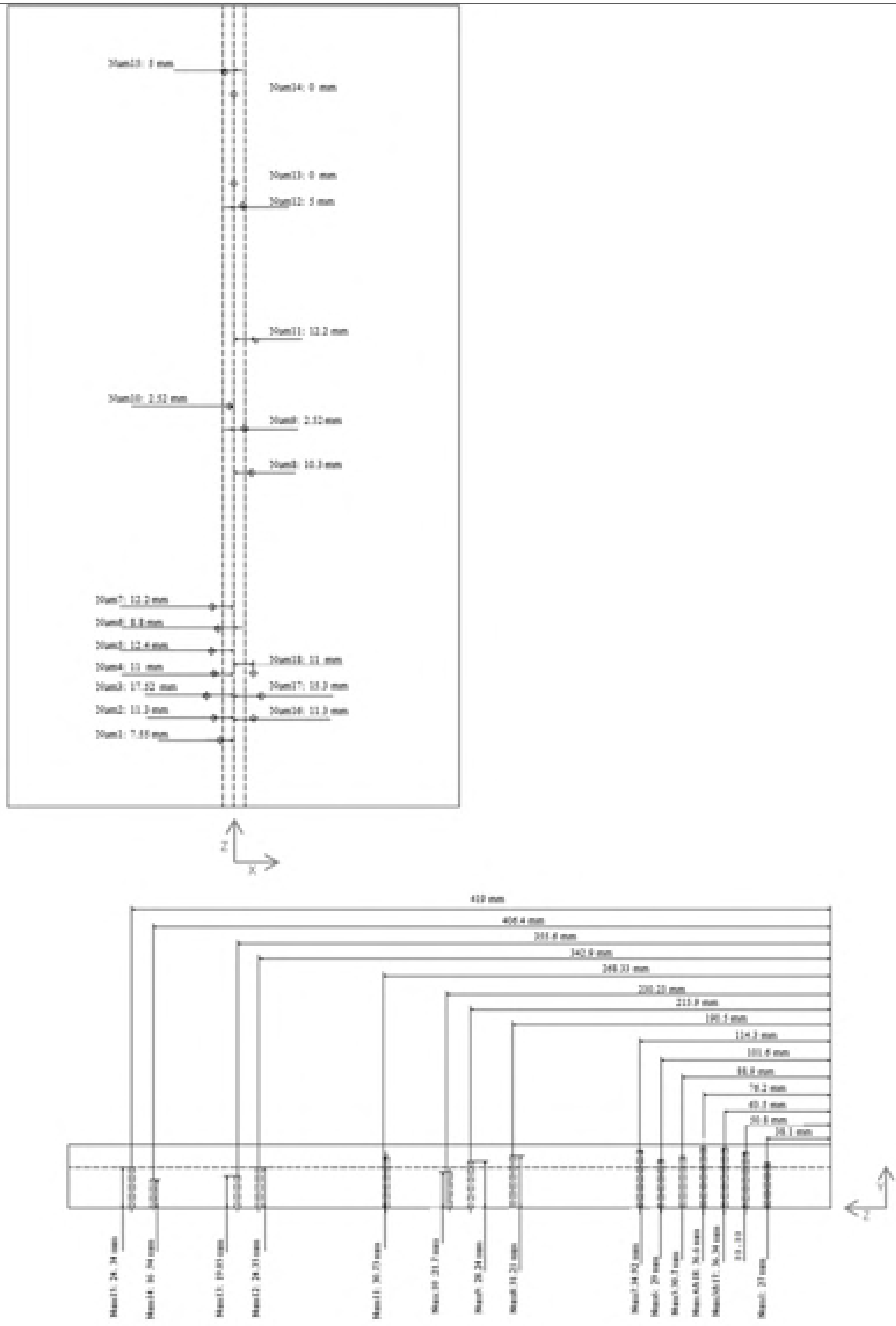

Figure 3.6 Drawing for machining, indicating the position of thermocouples on the plate

3.6 Thermocouples installation

The thermal history induced by welding was recorded experimentally. K-type thermocouples were employed in this research. Schematic set up of K-type thermocouples is presented in Figure 3.7. This type of thermocouples consists of two different wires protected against a contact with the plate by a ceramic tube with two holes. Each wire is passed through a hole in ceramic tube [27]. It is worth noticing that the k-type thermocouples are limited to applications with the temperature lower than 1200℃. The positions and depth of thermocouples are shown in Figure 3.5.

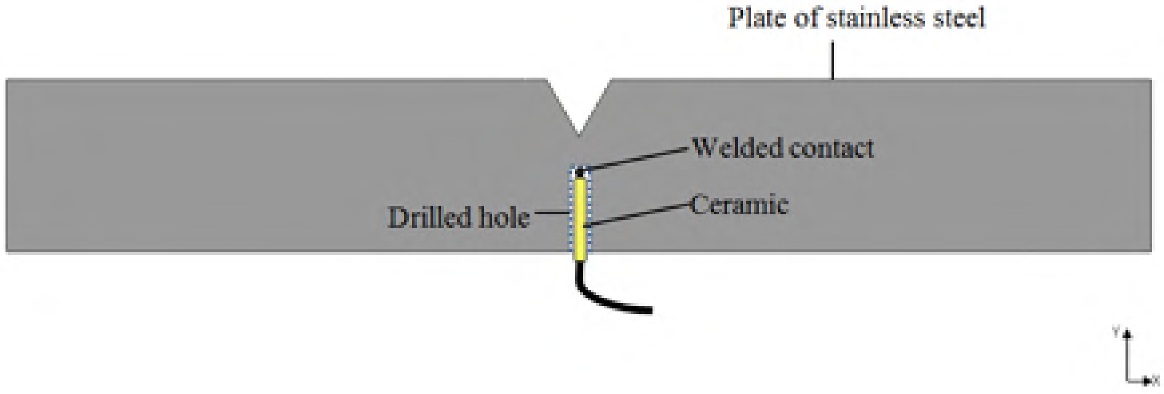

Figure 3.7 Schematic picture of K-thermocouples & installation

3.7 Characteristic of the welding set up

Flux-cored arc welding (FCAW) was employed as the welding process in this study. The base material and the filler metal were martensitic stainless steel 415 and 410 Ni-Mo TQS 1/16, respectively. The filler metal and the base metal have similar chemical compositions illustrated in Table 3.1. The plate was simply supported at three points to minimize heat transfer by conduction through direct contact with the structure. The installation of plate and welding torch are presented in Figure 3.8.

Figure 3.8 Installation of the plate on three points

Multi-pass welding was required to fill the V-groove in this study. Multi-pass welding is suggested to weld thick plates to avoid high current and to maintain adequate properties in the HAZ.

Prior to the first pass, the plate was preheated to 100℃ to ensure crack free welding [60]. The first pass was positioned at x=127 mm, $y = 25.4$ mm, and z varying from 0 to 457.2 mm. The arc characteristics were voltage of 28V, current of 292.9A, and feed rate of 6.5mm/s. A backhand technique was conducted for the three passes accompanied by a travel angle of

6°.[1] A work angle of 90° was applied for the first pass. In addition, the molten weld pool and hot surrounding metal were protected from ambient air for the three passes by mixed gas Argon- 25% CO_2.

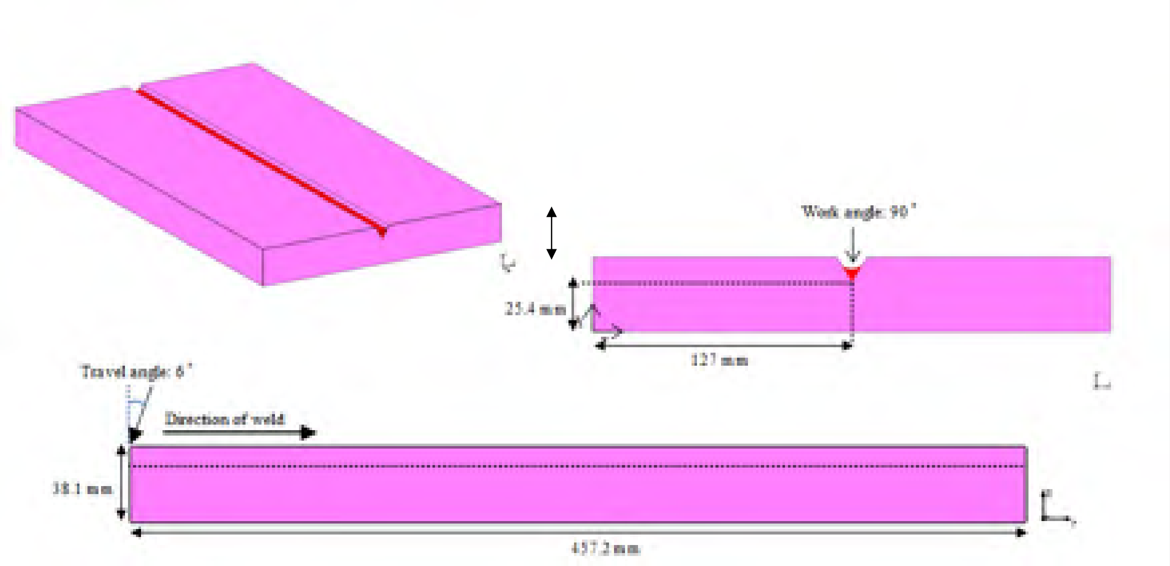

Figure 3.9 Schematic picture of coordinates and work angle of first pass

The second pass of welding was positioned at x=123.698 mm, y=32.512 mm and z varying from 0 to 304.8 mm. Inter pass temperature was approximately 150 ℃ for the second pass. A work angle of 65° was applied for second pass as shown in Figure 3.10. The arc characteristics were voltage of 28 V, current of 292.9 A, and feed rate of 6.5 mm/s.

---

[1] In the backhand welding technique, the torch is held perpendicular to the plate, tilting in the direction of welding for 6 degrees.

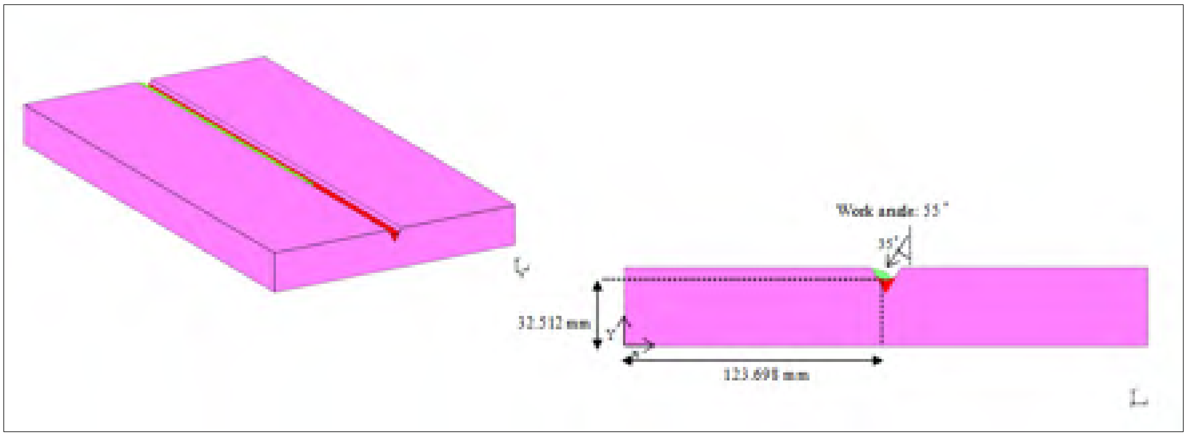

Figure 3.10 Schematic picture of coordinates and work angle of second pass

The angle between torch and the plate (work angle) for the second welding is presented in.Figure 3.11.

Figure 3.11 Installation of the plate and angle of torch for second pass of welding

The third pass of welding was positioned at x= 129.54 mm, y=32.512 mm and z varying from 0 to 152.4 mm. The inter pass temperature was measured to be 150℃. Arc characteristics were voltage of 28 V, current of 294.3 A, and feed rate of 6.5 mm/s. A work angle of 90˚ was applied for third pass too.

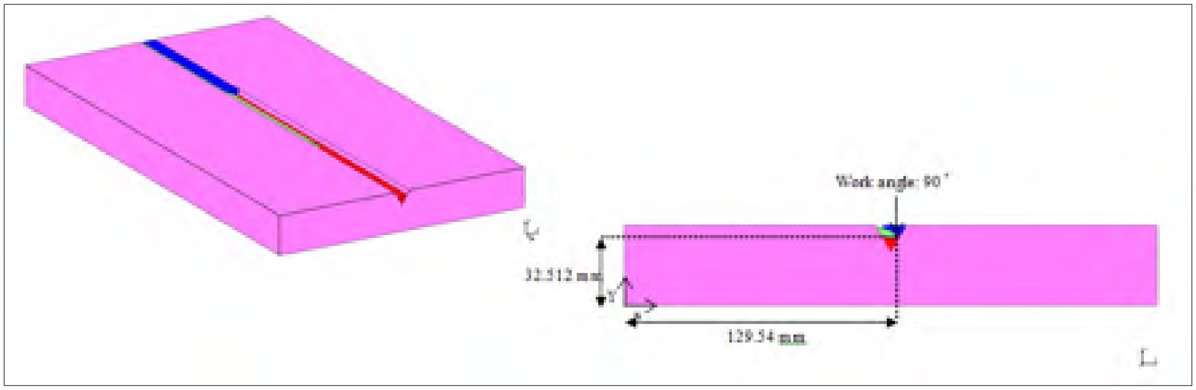

Figure 3.12 Schematic picture of coordinates and work angle of third pass

3.8 Microstructure analysis

The fully reversible nature of the phase transformation (γ →M) is known as an exceptional feature of martensitic steel 13%Cr- 4%Ni. The fraction of austenite transformed in the HAZ depends on the thermal cycle at each point. The measured hardness in HAZ reflects the fraction of martensite transformed to austenite.

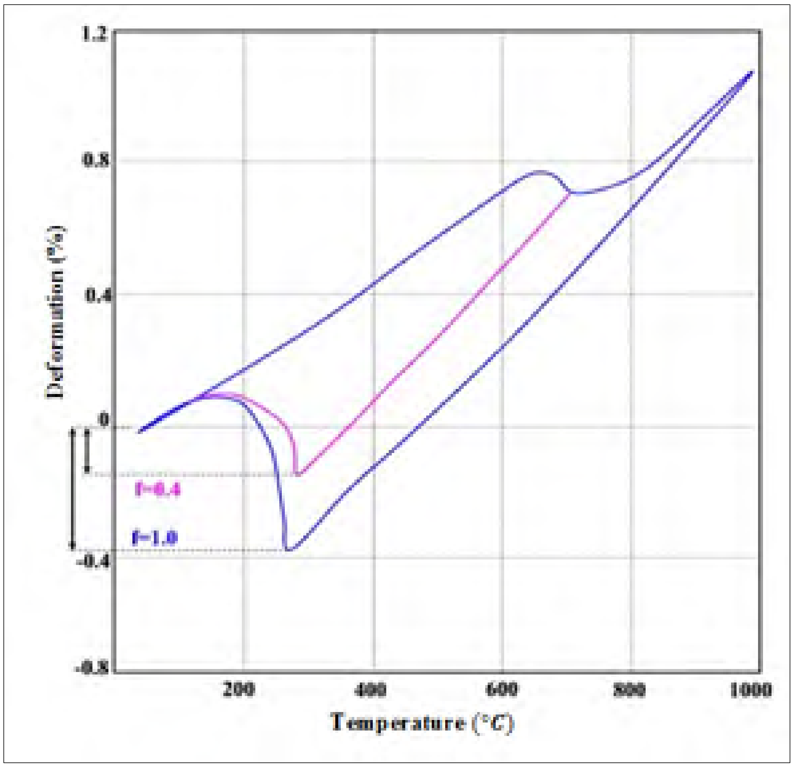

Figure 3.13 Two examples of phase transformation fraction

Figure 3.13 presents an example of complete and partial phase transformation (M→γ). The blue temperature cycle (f=1) is an example of complete phase transformation and 100% non-tempered martensite while the purple thermal cycle is an example of 40% progressed phase transformation producing 40% of non-tempered martensite. Various points in HAZ are composed of different fractions of tempered and non-tempered martensite and austenite depending on the temperature cycle they were exposed. Samples with smaller cross sections of welded plate were prepared, polished, and etched by Kallings (2.5 gr $CuCl_2$-$2H_2o$, 50ml HCl and 50 ml Ethanol) to investigate the phase transformation in HAZ. The samples were plunged in the etching solution for around 60 s.

The microstructure of the first weld is presented in Figure 3.14 including filler metal, base metal and phase transformation in HAZ. Microstructure and micro hardness of sub-size specimens will be investigated and compared by calculated results as presented in chapter 5.

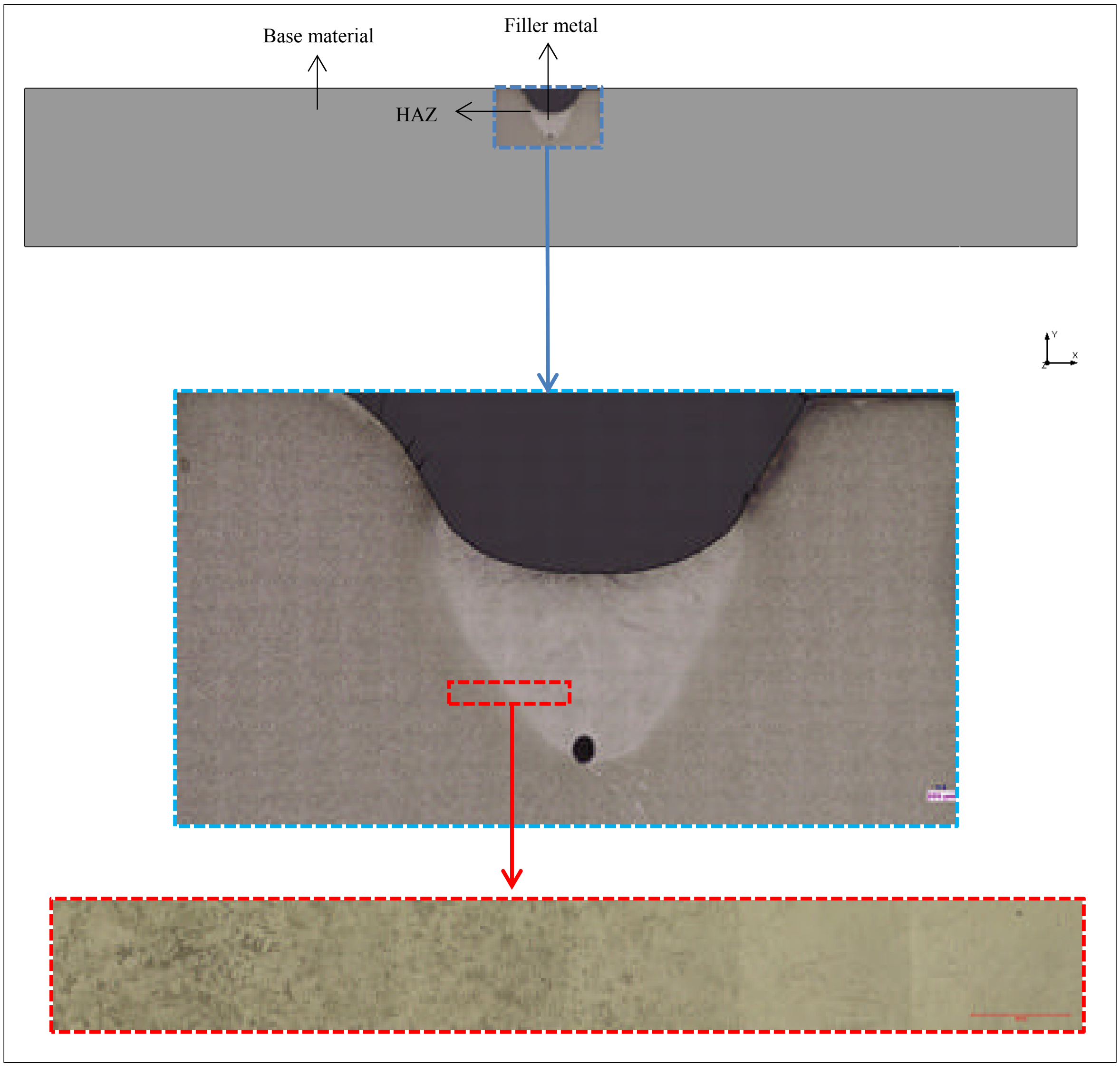

Figure 3.14 Microstructure of cross section for first pass of welding

3.9 Micro hardness Measurement

Micro hardness imprints at a load of 100 g and a distance of 150 µm between points were used to determine hardness at different locations and produce hardness map.

It should be considered that the phase transformation causes a variation of hardness in HAZ. Developing 3D hardness map is helpful for characterizing the dimensions of heat affected zone. 3D hardness map can also help to determine the maximum temperature reached at specific points of weld. Transverse and longitudinal sections of the plate for each pass are required to achieve a 3D hardness map.

3.10 Reproduction of calculated thermal history of welds

A reproduction of calculated thermal history at some nodes from small size specimens and a comparison of measured hardness in both small size specimens and the actual position of the corresponding node in the welded plate is the last step of experiment to validate simulations.

The simulation of first welding pass was carried out before this part of experiment and the simulation will be described in chapter 4. Then, thermal profile of some nodes (placed in or in the vicinity of HAZ) was considered for the reproduction since phase transformation had a serious effect on hardness in or near HAZ. Moreover, comparison between measured micro hardnesses was the criteria to validate the calculated temperature in HAZ. Ten nodes with maximum temperature in a range of 800℃ - 1200℃ were selected to reproduce their thermal profile in small samples of base material. Thermal profile of a node is presented in Figure 3.15 as an example.

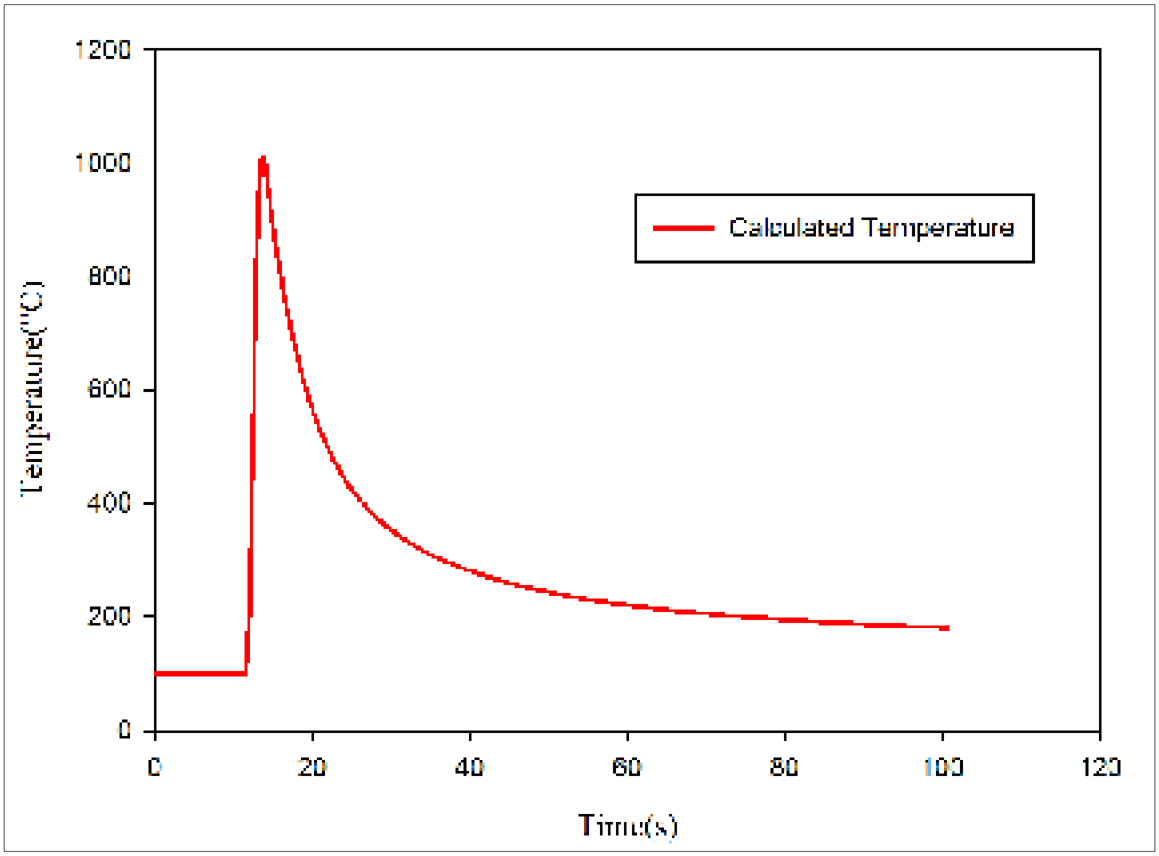

Figure 3.15 Calculated thermal profile for a specific node in simulation

Rapid rate induction heating and controlled rate cooling by Helium assistance were used to reproduce the thermal history of selected nodes in the FEM model located in the HAZ. In this experiment, temperature was controlled by installing k-type thermocouples as it is presented in Figure 3.16.

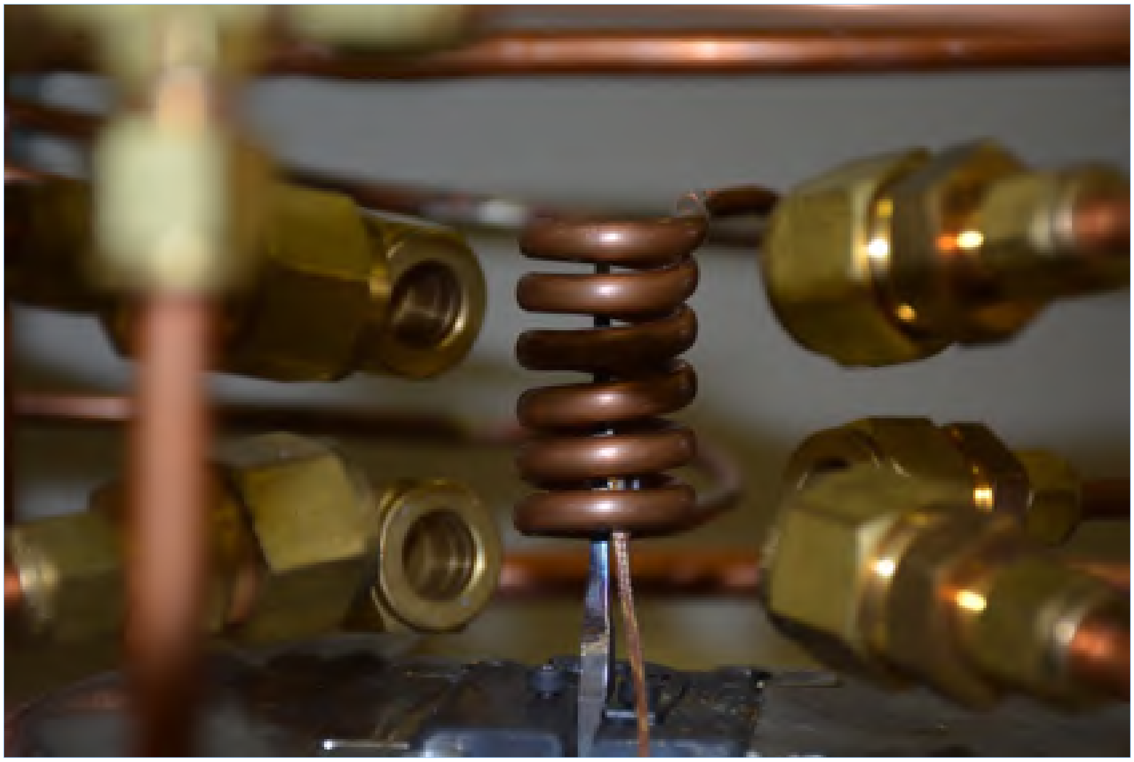

Figure 3.16 Installation of equipment for reproduction of thermal history

Finally, the hardness of small samples was compared to measured hardness at the position of instrumented node on the plate.

CHAPTER 4

THERMAL SIMULATION OF MULTI-PASS WELDING

4.1 Introduction

The procedure of multi-pass welding simulation is discussed in this chapter. A summary of finite element method is reviewed in the first section since finite element method is employed. Furthermore, convergence analysis of finite element method is required to minimize the simulation time without decreasing its accuracy. In addition, it is noteworthy to achieve a mesh independent and a time step independent solution. Thermal properties are also pointed out, as they are very important in a thermal simulation.

4.2 Finite element method

Finite element method is proposed for the numerical analyses of heat transfer in this study. Welding process has certainly a non-linear nature because of a time dependent temperature history in the welded plate due to the welding source movement, temperature dependency of thermal properties and involvement of radiation in heat transfer. The heat equation (4.1) has been suggested as a solution for this type of problems by Cook [71].

$$[C]\{\dot{T}\} + [K_T]\{T\} = \{R_T\} \tag{4.1}$$

Where $[K_T]$ is the sum of the thermal conductivity matrix and the combined convection and radiation matrix, $[C]$ is the specific heat matrix, $\{T\}$ is nodal temperature vector, $\{\dot{T}\}$ is the vector of temporal temperature variation, and $\{R_T\}$ is the sum of the power source vector and the combined convection and radiation heat flux vector.

Equation (4.1) can be solved numerically with standard FE models by the modal method or direct time integration solution. Time integration solution is used to solve nonlinear problems such as sharp transient in this research [29, 71, 72].

If two temperature states such as T_n and T_{n+1} are considered by Δt separating time, temporal integration is calculated through equation (4.2).

$$\{T\}_{n+1} = \{T\}_n + \Delta t\big\{(1-\beta)\dot{T}_n + \beta\dot{T}_{n+1}\big\} \tag{4.2}$$

The combined equation of (4.1) and (4.2) is

$$(1-\beta)([C]\{\dot{T}\}_n + [K_T]\{T\}_n) = (1-\beta)\{R_T\}_n \tag{4.3}$$

$$\beta\left([C]\{\dot{T}\}_{n+1} + [K_T]\{T\}_{n+1}\right) = \beta\{R_T\}_n \tag{4.4}$$

If $[K_T]$ and $[C]$ are time independent, we can add equation (4.3) and (4.4) , then use equation (4.2) to eliminate time derivatives of temperature. The result is as follow

$$\left(\frac{1}{\Delta t}[C] + \beta[K_T]\right)\{T\}_{n+1} = \left(\frac{1}{\Delta t}[C] - (1-\beta)[K_T]\right)\{T\}_n + (1-\beta)\{R_T\}_n + \beta\{R_T\}_{n+1} \tag{4.5}$$

It is noteworthy that neglecting the variation of $[K_T]$ and $[C]$ between two temperatures generates a numerical error. However, decreasing the separating time Δt reduces the error [36].

Several methods can be applied to solve equation (4.5) as it is shown in Table 4.1. Different values of parameter β are applied in different methods. Crank-Nicolson method is employed in this research, which is a popular second order accurate method.

Table 4.1 Different methods of direct time integration solution

Parameter β	Method	Stability
0	Forward difference or Euler	Conditionally stable
$1/2$	Crank-Nicolson	Unconditionally stable
$2/3$	Galerkin	Unconditionally stable
1	Backward difference	Unconditionally stable

4.3 Arc modeling

In this study, Goldak moving heat source model is employed to model heat input from the arc welding (FCAW). As mentioned in the literature review (section 1.4.2.3), Gaussian distribution of power density in double ellipsoidal geometry reflects energy input and arc penetration accurately. The equation (4.6) corresponds to the calculation of heat input through Goldak's model.

$$q(x,y,z,t) = Sf\,\frac{3f\sqrt{3}f_{(r,f)}Q}{abc\pi\sqrt{\pi}}\,e^{{-3x^2}/{a^2}}e^{{-3Y^2}/{b^2}}e^{{-3(z+v(\tau-t))}/{c^2}} \tag{4.6}$$

This equation is described by five unknown parameters; a (width of the heat source), b (depth of the heat source), c_r (length of rear ellipsoidal), c_f (length of front ellipsoidal), f_r (rear heat fraction) and f_f (front heat fraction) considering a relation between rear fraction and front fraction ($f_r + f_f = 2$).

Front heat fraction and rear heat fraction are assumed 1.4 and 0.6 based on the literature [46]. Other parameters are adjusted to achieve the agreement between calculated temperature and experimental data.

Energy input is applied through an ellipsoid in Goldak model when welding is conducted on straight-line surface (coefficient $Sf = 2$ is applied in equation (4.6) since energy is entered in half ellipsoid. In the present work, shape factor is employed since welding is deposited in V-groove. Therefore, the coefficient S*f* is not the same value as Goldak model. Theoretical input energy (Q_{th}) is estimated through equation (1.3). Then, the theoretical input energy is determined through the multiplication of the experimentally applied voltage and current, as well as, the efficiency of heat source. The efficiency is adjusted to optimize the predictions of thermal profile far from the weld bead.

Calculated energy input (Q_{cal}), from numerical integration of the simulation results, is different from the theoretical one. Theoretical input energy and calculated input energy are related through equation (4.7)

$$Sf = {}^{Q_{th}}/_{Q_{cal}} \tag{4.7}$$

Coefficient *Sf* (shape factor) is changed in each heat source depending on the surface shape since depositing filler metal changes the surface shape. Goldak's heat source model is intended in order to compute heat generation on a flat face. The shape factors are calculated in the simulation through equation (4.7) for each step. Shape factor should be less than 2 in each step as the energy is entered in a larger volume in V-preparation compared to non-preparation surface, as it is presented in Figure 4.1

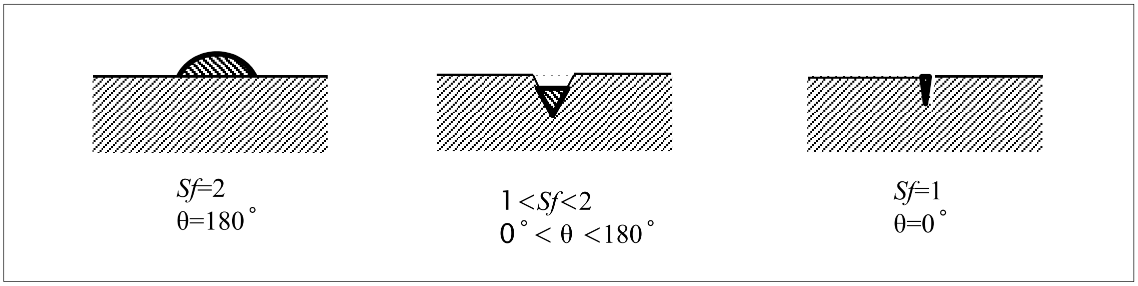

Figure 4.1 Shape factors corresponded to different surfaces

4.4 Mesh and element size

The simulation results are affected by the size of elements wherein the size of elements is not fine enough. The sensitivity analysis is performed by comparing the convergence of simulations with different element sizes. In this research, maximum and minimum temperatures are chosen to verify the convergence. A simulation is conducted by large elements, and then the same simulation is conducted using a finer mesh. This procedure is repeated until the results for a specific temperature show a similar distribution. Finer mesh requires more calculation time and memory. The optimisation of calculation time and mesh size is conducted in this research.

A fine mesh is used in or near HAZ because of the high temperature gradient in this area while larger elements are used in the areas far from the HAZ. It helps to avoid the fine mesh for entire geometry, which results in high computational cost. In this type of research, the element size of 1 mm is fairly adequate nearby the welding line [32].

The 3D FE model of plate contains 73691 nodes with associated 66780 elements. HEX 8 elements (i.e. eight-node linear hexahedrons) are used for meshing the model. The model after meshing is presented in Figure 4.2**Erreur ! Source du renvoi introuvable.**

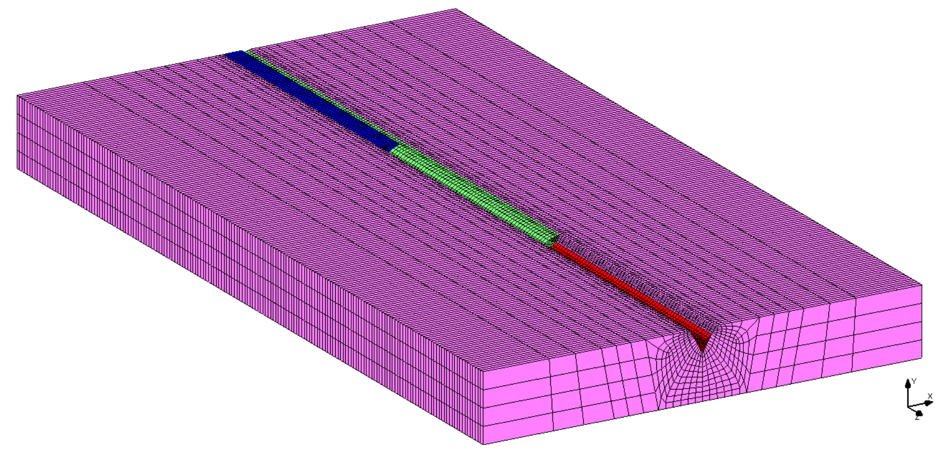

Figure 4.2 Hexahedral mesh structure of the plate

Twenty nodes are selected at the thermocouples locations to plot temperature changes during welding simulation. The places of nodes are adjusted in modeling to reflect the exact position of the thermocouples. An initial temperature of 100 ° C is imposed on all nodes in the model in regard to the preheat temperature in the experiment.

Elements corresponding to the filler metal are added through element birth method in this research. Designated time to activate the elements is controlled by geometric predominantly criteria. Elements will be activated through changing their properties when the heat source arrives to the filler metal elements for each welding line.

4.5 Material properties

Thermal properties of stainless steel 415 are temperature dependant as it was described earlier section 1.3.4. The values of specific heat, thermal conductivity and emissivity are important in this study and will be explained in the following sections.

4.5.1 Specific heat

Specific heat is measured in this study since it was not reported in the literature for stainless steel 415. The measurements are performed for the temperatures below 1000℃ since this temperature range is of interest due to phase transformation. Data is obtained from the literature for the temperatures above 1000℃ [35]. Variations of specific heat did not exhibit an identical trend during cooling and heating. In other words, specific heat shows different temperature dependency in the cooling and the heating process. The specific heat graphs are shown in Figure 4.3, the black and red curves correspond to the specific heat during heating and cooling respectively.

Two sharp augmentations in the black curve correspond to the phase transformation and melting phenomenon. The measurement of the specific heat also include latent heat. The first augmentation occurs in the temperature range between 600℃-800℃, which is related to transformation of martensite to austenite during heating. The second augmentation happens at the temperature of 1200°C, which corresponds to the melting of the material. Considering the red graph, the augmentation in the temperature range between 300°C-200°C is noticable which correlates to the transformation from austenite to martensite phase during cooling.

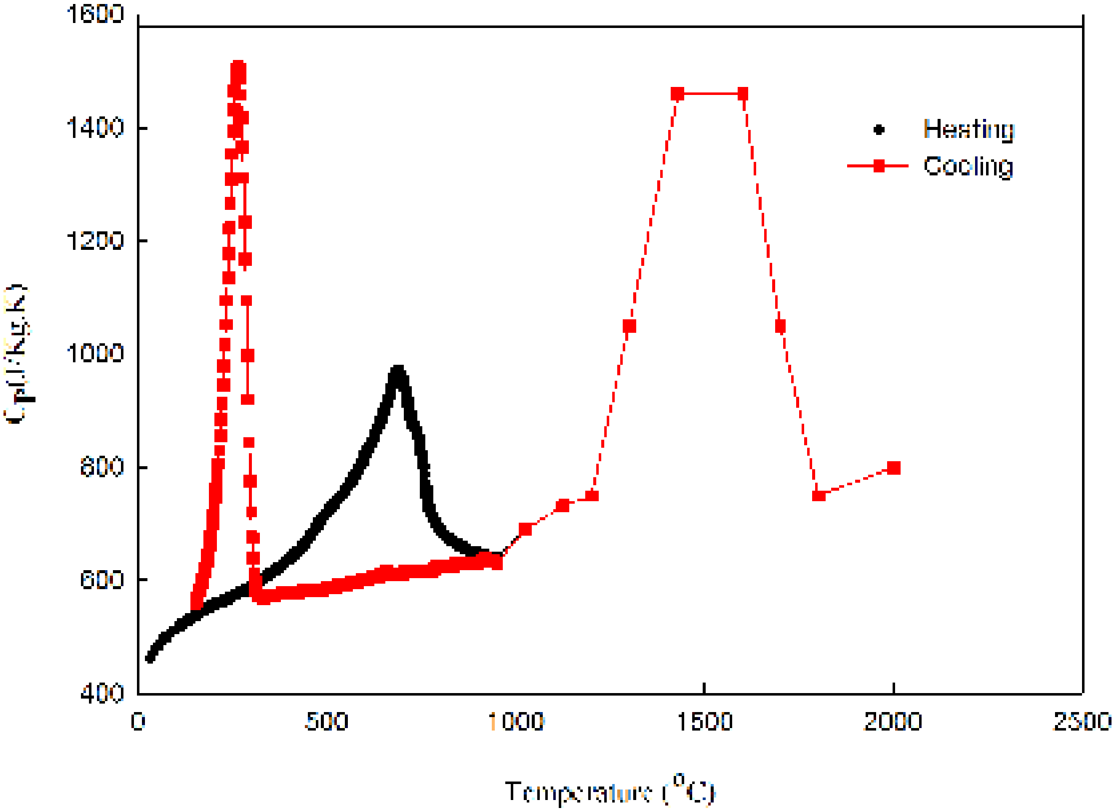

Figure 4.3 Applied specific heat of stainless steel 415 in simulation

4.5.2 Conductivity

The value of conductivity is also measured for the temperatures below 1000 ℃ in this research in addition to specific heat. Conductivity versus temperature is presented in Figure 4.4 for this material. Thermal conductivity follows different trends during the heating and cooling because of the phase transformation. During heating, thermal conductivity increases with increasing the temperature. Furthermore, a sharp augmentation in the range between 600 °C-800°C corresponds to the phase transformation from martensite to austenite. Second sharp augmentation appears at melting temperature (1200°C). Moreover, thermal conductivity decreases with temperature reduction. Moreover, the appearances of two peaks are originate from the phase transformation and melting, as the one observed in the specific heat.

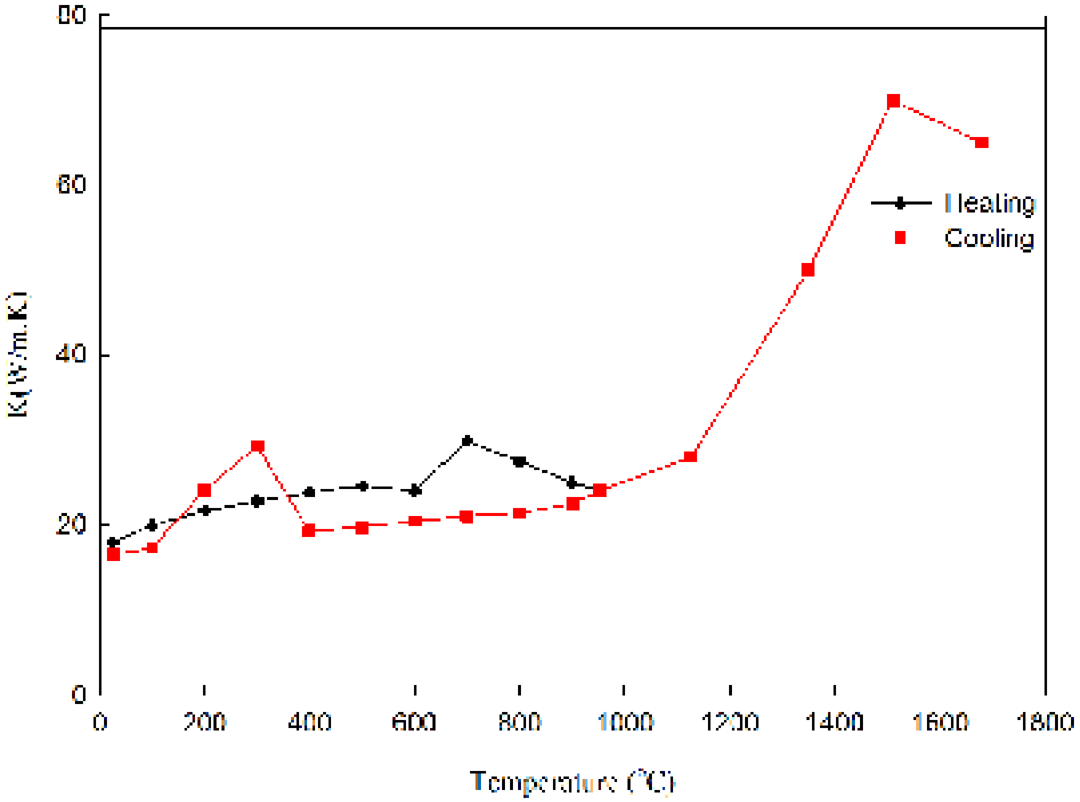

Figure 4.4 Applied conductivity of stainless steel 415 in simulation

Therefore, phase transformation effects on the material properties significantly. It is noteworthy that the effective temperature for the phase transformation is not the same during cooling and heating. Phase transformation occurs in the range from 600 °C to 800°C during heating and in the range from 200 °C to 400°C during cooling as it is presented in Figure 4.4.

Thermal properties of filler metal were assumed as base material properties, owing to similar chemical composition in this research.

4.6 Summary

Finite element method is used to simulate welding in this study. Goldak model is chosen to simulate heat source. Its parameters are investigated in purpose of achieving the best results. Furthermore, shape factor is suggested in this chapter to prevail the limitation of Goldak model for V-preparation surface. Finally, the thermal properties of stainless steel are presented based on the measured data at IREQ.

CHAPTER 5

RESULTS AND DISCUSSION

In this chapter, the simulated data were compared to the experimental results to validate the simulation. First, applying the Goldak's parameters caused the predicted results to meet experimental data, corresponding to the first welding pass, closely. Subsequently, the predicted temperature profiles were compared to the measured ones at 20 given points, where the thermocouples were embedded. The microstructure and micro hardness maps of the weld pool were schematically illustrated for three passes of welding, accompanied by the predicted results. At last, the measured micro hardness was correlated to the predicted one to find out the efficiency and the reproducibility of the simulation.

5.1 Goldak's parameters adjustment

The simulation result is controlled by Goldak's input parameters, heat source efficiency, material properties, boundary condition and the position of the heat source. In this section, the Goldak's parameters and heat source efficiency were adjusted for the first welding pass. The same Goldak's parameters were kept for all the welding passes. Therefore, these parameters determine the size and shape of fusion zone, as well as, the thermal profile of thermocouples. The predicted shape of fusion zone and the maximum temperature of thermocouples were compared to the experimental data to adjust the aforementioned parameters. The results are summarized in Appendix I and Appendix II.

Figure 5.2 presents the variation of average error corresponding to the different simulations of first pass. The average error was calculated from equation (5.1). The initial parameters for simulation #1 were extracted from reference [32]. However, the coordinates of heat source was frequently changed in simulations according to the torch place within the experimental procedure.

$$Error_{ave} = \frac{\sum_{i=1}^{n} \sqrt{(T_{\max(\exp)_i} - T_{\max(cal)_i})^2}}{n} \tag{5.1}$$

Where $T_{\max(\exp)}$,$T_{\max(cal)}$ and n stand for the maximum measured temperature, the maximum calculated temperature and thermocouple number. In the first step, the coordinates of the first heat source was determined. X and Y stand for the horizontal location and vertical location of the heat source as it was presented in Figure 5.1. X was considered zero since the heat source was placed in the middle of the plate. Furthermore, axis origin is at mid length of the plate. Y was changed in the simulations #1 to #9, minimizing the average error to predict heat affected zone more accurately. The minimum average error was observed in simulation #2.

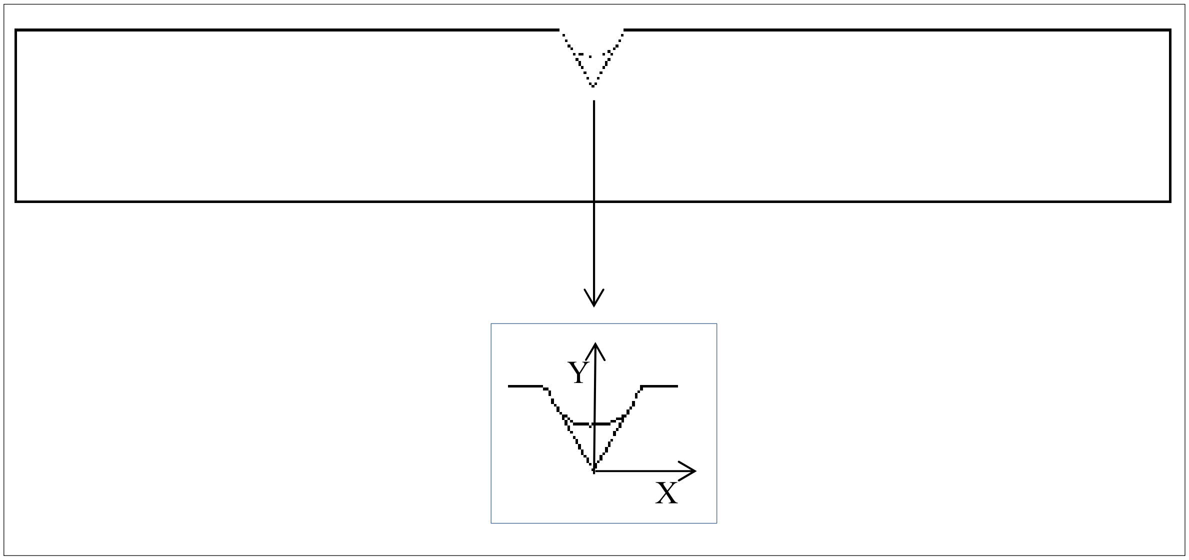

Figure 5.1 Origin coordinates in the plate

An attempt was carried out to find an interpretation of the simulation outcome upon changing the width of heat source, a, and the depth of penetration b, in simulation #10 to #13. The increase of the heat source depth led to a better prediction of the melted zone in vertical direction, compared to the experimentally observed shape. No noticeable effect on the average error was detected since the calculated maximum temperature was improved for some thermocouples, worsening in other ones compared to the measured data. Therefore, the undesirable predicted melted zone of simulation #2 arose from the inadequate depth of the heat source. Nevertheless, the volume of Goldak's ellipsoid increased by the increase of the depth, decreasing the width of melted zone for a given energy. The rest of parameters have been kept constant. This is consistent with the simulated data corresponding to the melted zone in simulations of #2, #12, #5, and #15. It was found that, the width of melted zone decreased upon the increase of heat source depth.

The predicted shape of the melted zone became closer to the experimentally observed one with the increase of depth and the decrease of width of the heat source concurrently, presented in Appendix II. Therefore, the closest shape was predicted in simulation #12.

The variation of the heat source location led to different optimized values of width, a, and depth, b, in the simulation. Therefore, those three values were modified in the simulation #13 to #18, to reach the experimentally detected shape of the melted zone. This was roughly achieved in the simulation #12 and #15. It is worth noticing that, a and b were changed in simulation #19 and #20 concurrently as the rest of parameters were the same as the simulation 12. However, b was changed in the simulation#15, the result reflected in the simulation#21.

The prediction of maximum temperature at different thermocouples clearly demonstrated the inadequate efficiency of the heat source as revealed in simulation #21 and maximum calculated temperature and measured maximum temperature are presented in Appendix II. This is deduced from the lower predicted maximum temperature compared to the measured one at distinct thermocouples. It is offered to enhance the applied efficiency of the heat source to increase the predicted maximum temperature. Subsequently, the efficiency in the simulation #12, #15, #19 and #21 was increased from 80 to 81%. The outcome was revealed in the simulation #22, #23, #24 and #25, respectively. One can observed that the predicted maximum temperature becomes closer to the experimentally collected data through the thermocouples. Furthermore, this change caused the predicted shape of the melted zone to approach the experimentally measured one in simulations #22 and #24 compared to simulation #12 and #19.

Table 5.1 The average error corresponding to simulations #1 to #25

#Simulation	Error_{ave}	a (mm)	b (mm)	c_f (mm)	c_r (mm)	η (%)	y (mm)
1	38.50	6	6	6	12	80	0
2	6.05	6	6	6	12	80	5.080
3	12.78	6	6	6	12	80	2.540
4	7.75	6	6	6	12	80	3.810
5	6.25	6	6	6	12	80	4.572
6	6.57	6	6	6	12	80	4.318
7	6.11	6	6	6	12	80	4.826
8	6.05	6	6	6	12	80	5.334
9	6.17	6	6	6	12	80	5.558
10	6.14	6	7	6	12	80	5.080
11	7.31	7	6	6	12	80	3.810
12	6.48	5	7	6	12	80	5.080
13	6.99	7	5	6	12	80	3.810
14	6.15	6	5	6	12	80	4.572
15	6.74	6	7	6	12	80	4.572
16	7.22	5	7	6	12	80	4.572
17	6.14	7	5	6	12	80	4.572
18	6.26	7	6	6	12	80	4.572
19	7.21	5	8	6	12	80	5.080
20	6.14	5.5	6.5	6	12	80	5.080
21	7.51	6	8	6	12	80	4.572
22	6.31	5	7	6	12	81	5.080
23	6.66	6	7	6	12	81	4.572
24	7.11	5	8	6	12	81	5.080
25	7.47	6	8	6	12	81	4.572

The efficiency of the simulation #22 was also enhanced in the simulation #26 and #27 while the rest of adjustable parameters were constant. The same procedure induced in the simulation #24, reflected through the simulation #28 and #29. A larger efficiency was applied in the simulation #29 than that of the simulation #28.

The average errors and the shape of melted zones were investigated for the simulations #26 to #29. The predicted shape of the melted zone was much similar to the experimentally detected morphology in the simulations #26 and #27 among the executed simulations, whereas a hole appeared at the end of V-preparation within the microstructure of 2D cross-section of the sample. It is also striking that, less average error occurred in the simulations #26 and #27 than the simulations #28 and #29, as it is shown in Table 5.2.

An effort was made to diminish the average error in the simulation #30 and #31 by changing the efficiency. The parameters of simulation #30 were applied to the simulation #32 to #49 while the effect of length of rear ellipsoid, c_r, and length of front ellipsoid, c_f were evaluated. The contribution of the length of the ellipsoid is less pronounced than those of the heat source depth and heat source width to the shape of melted zone as presented in Appendix I.

The length of front and rear ellipsoid are represented along the welding pass direction, *Z*. However, in this study, no data was collected along the *Z* direction in the experiments, whereas no effect along Z is expected as long as the welding rate is constant. In the other words, temperature is independent of Z direction far from either end of the plate. Nevertheless, the average error was influenced by these parameters. It was found that, the average error decreases upon the increase of c_r and c_f .The minimum error was observed in the simulation #47.

Table 5.2 The average error corresponding to simulations #26 to #46

#Simulation	Error$_{ave}$	a (mm)	b (mm)	c_f (mm)	c_r (mm)	η (%)	y (mm)
26	6.28	5	7	6	12	82	5.080
27	6.38	5	7	6	12	83	5.080
28	7.13	5	8	6	12	82	5.080
29	7.26	5	8	6	12	83	5.080
30	6.28	5	7	6	12	81.5	5.080
31	6.32	5	7	6	12	82.5	5.080
32	6.24	5	7	7	12	81.5	5.080
33	6.31	5	7	5	12	81.5	5.080
34	6.21	5	7	6	11	81.5	5.080
35	6.36	5	7	6	13	81.5	5.080
36	6.39	5	7	5	11	81.5	5.080
37	6.34	5	7	4	12	81.5	5.080
38	6.43	5	7	6	10	81.5	5.080
39	6.32	5	7	7	11	81.5	5.080
40	6.21	5	7	8	12	81.5	5.080
41	6.18	5	7	9	12	81.5	5.080
42	6.16	5	7	8	13	81.5	5.080
43	6.10	5	7	8	14	81.5	5.080
44	6.13	5	7	9	13	81.5	5.080
45	6.10	5	7	10	13	81.5	5.080
46	6.08	5	7	9	14	81.5	5.080

Subsequently, a and b were optimized in the simulations #50 to #54, as c_r and c_f corresponding to the minimum error in the simulation #47, was applied. It was concluded that, the increase of the heat source width from 5 mm, in simulation #47, to 7 mm, in simulation #52, caused a slight decrease of the average error. This is the least obtained average error among 54 simulations. The efficiency of heat source was enhanced in the simulation #52 to reach a more realistic prediction of the maximum temperature of thermocouples in the simulation #55 to #57, as the effect of variation of efficiency was disclosed on the maximum temperature earlier. One can observe that, the increase of efficiency from 81.5 to 82.5% led to a decrease in the average error from 5.54°C to 5.43°C. This average error is the least in the welding simulation compared to that of simulation #52. Therefore, the width, depth, front length, rear length, vertical coordinate of the heat source, and the efficiency were assumed, respectively, 7 mm, 7 mm, 10 mm, 14 mm, 5.08 mm, and 82.5%. These values were extracted from simulation #55 in Table 5.3. Nevertheless, these parameters were individually changed within the next step to demonstrate that the simulation #55 reveals the minimum average error.

Table 5.3 The average error corresponding to simulations #47 to #57

#Simulation	Error_{ave}	a (mm)	b (mm)	c_f (mm)	c_r (mm)	η (%)	y (mm)
47	6.06	5	7	10	14	81.5	5.080
48	6.08	5	7	11	15	81.5	5.080
49	6.08	5	7	10	15	81.5	5.080
50	6.51	4	7	10	14	81.5	5.080
51	5.71	6	7	10	14	81.5	5.080
52	5.54	7	7	10	14	81.5	5.080
53	5.65	8	7	10	14	81.5	5.080
54	6.28	6	8	10	14	81.5	5.080
55	5.43	7	7	10	14	82.5	5.080
56	5.48	7	7	8	14	82.5	5.080
57	5.63	7	7	8	12	82.5	5.080

The width of Goldak’s ellipsoid was evaluated at first. The simulations were performed to investigate the effect of varying the ellipsoid width in the range of 5 to 9 mm on the average error, whereas the other parameters were kept constant as simulation #55. The five resultant average errors were represented in Figure 5.2 within the range of ellipsoid width. The accuracy of this parameter is 1 mm in this study. The minimum average error occurred for the ellipsoid width of 7 mm, identical with the simulation #55.

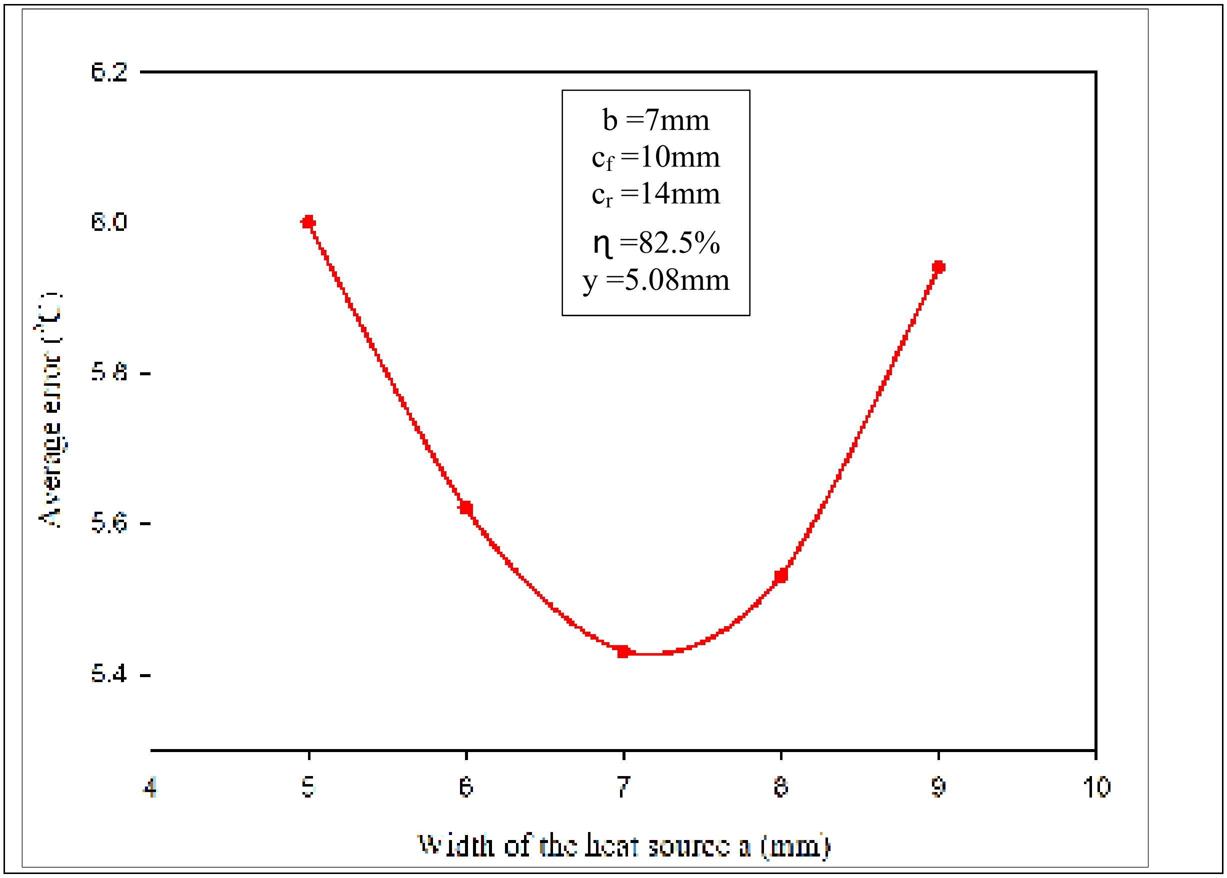

Figure 5.2 The variation of average error based on the width of Goldak’s ellipsoid (parameter a)

Subsequently, the same procedure was conducted on the depth of heat source, in the range of 5 to 9 mm. The average errors were compared in Figure 5.3 to that of the simulation #55 to determine the optimized value. The minimum average observed at the heat source depth of 7 mm, as addressed in the simulation #55 in Table 5.3.

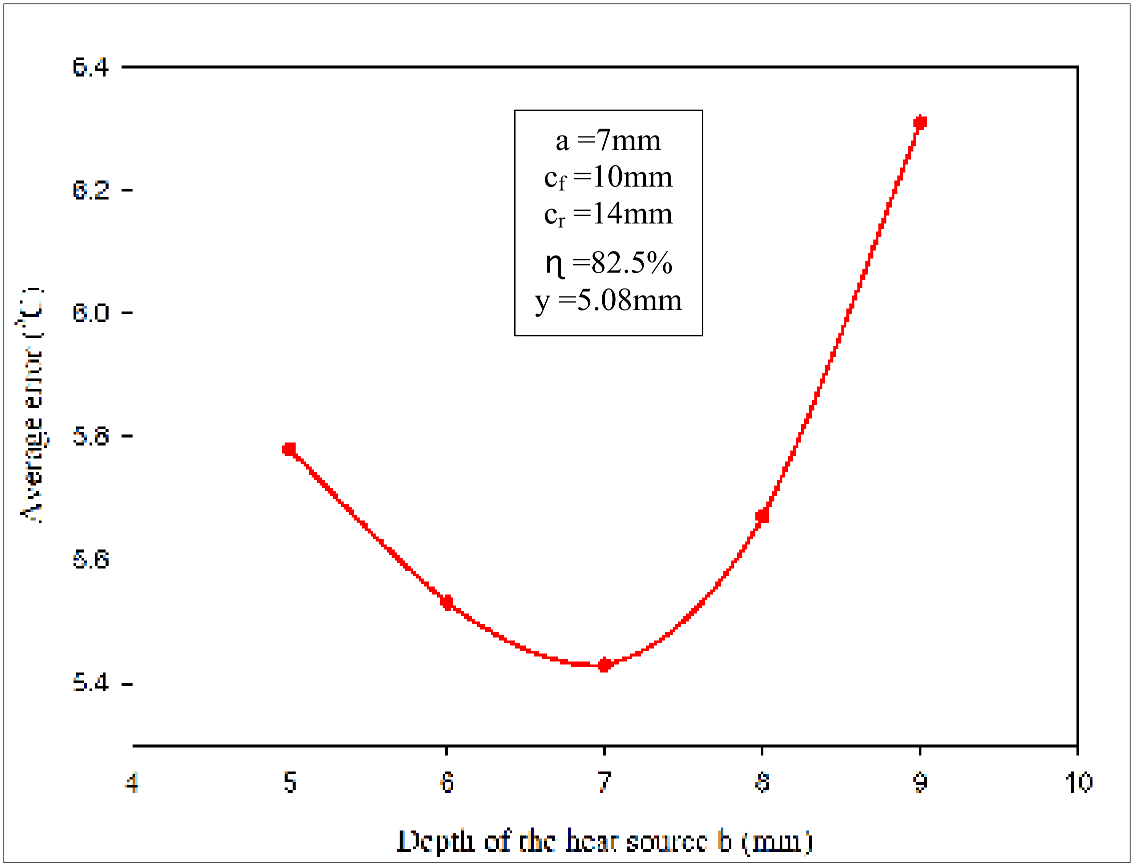

Figure 5.3 The variation of average error based on the depth of Goldak's ellipsoid (parameter b)

The simulation was repeated as the front length of ellipsoid, c_f was changed in the range of 8 to 12 mm. c_f in simulation #55 is larger than what applied in literature [6]. Goldak et al. was considered c_f to be 6 mm. It is noteworthy that the welding process (FCAW) in this study was not the same as literature (TIG). Furthermore, the V-preparation of the plate may affect the value of c_f, however, this fact is missing in the assumed configuration of Goldak. In this study, the optimized value was promoted to 10 mm to minimize the average error. The average errors of simulations were estimated by different values of c_f, shown Figure 5.4. Nevertheless, the minimum average was observed in the simulation #55, corresponding to the ellipsoid front length of 10 mm within the range of applied c_f. The applied c_f is adjusted with an increment of 1 mm in this study.

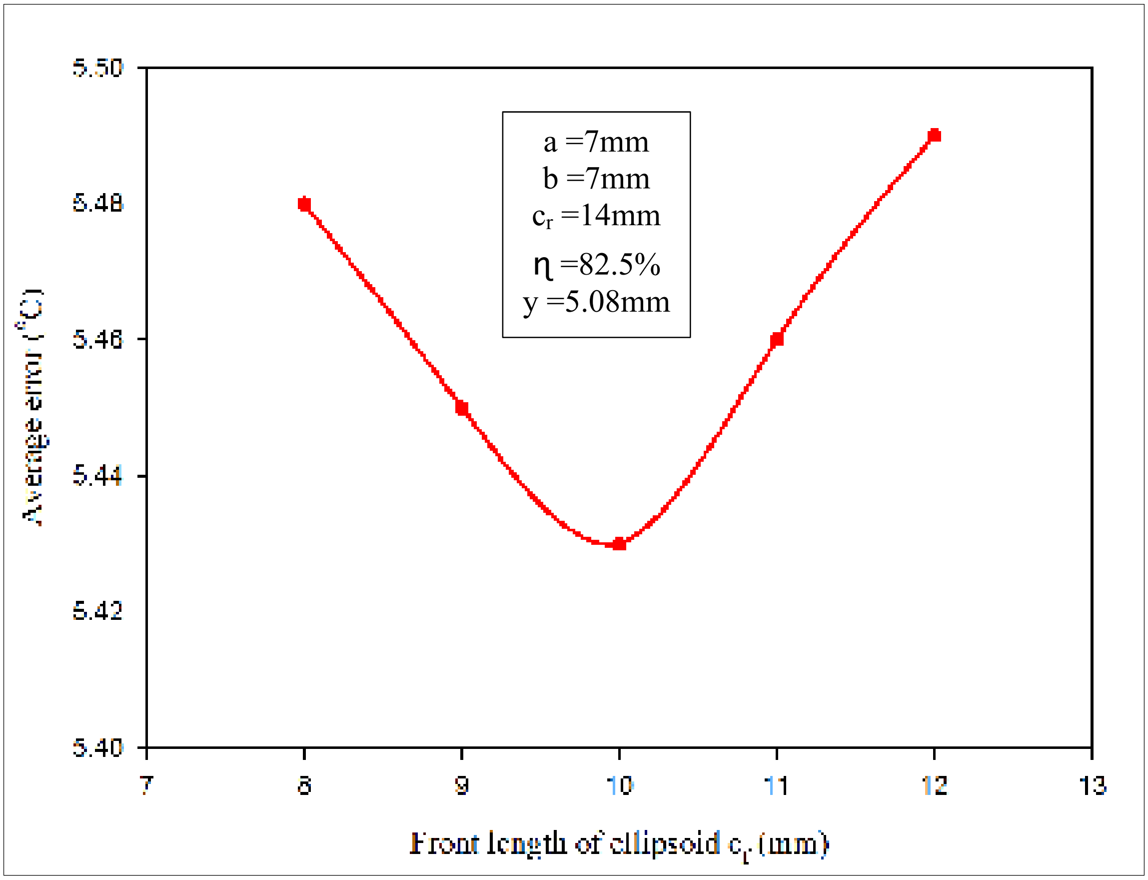

Figure 5.4 The variation of average error based on front length of ellipsoid (parameter c_f)

The rear length of ellipsoid, c_r, was also altered in the range of 12 to 16 mm to calculate the variation of the average error in this range through the simulation. In the simulation #55, c_r was 12 mm. In other words, this was 2 mm larger than that of the Goldak's. The average error was diminished from 5.55°C to 5.43°C upon the enlargement of ellipsoid rear length from 12 to 14 mm, as illustrated in Figure 5.5. Therefore, the average error was minimized at the optimized c_r equal to 14 mm among these five simulations. In this study, the applied c_r is adjusted with an increment of 1 mm in this study.

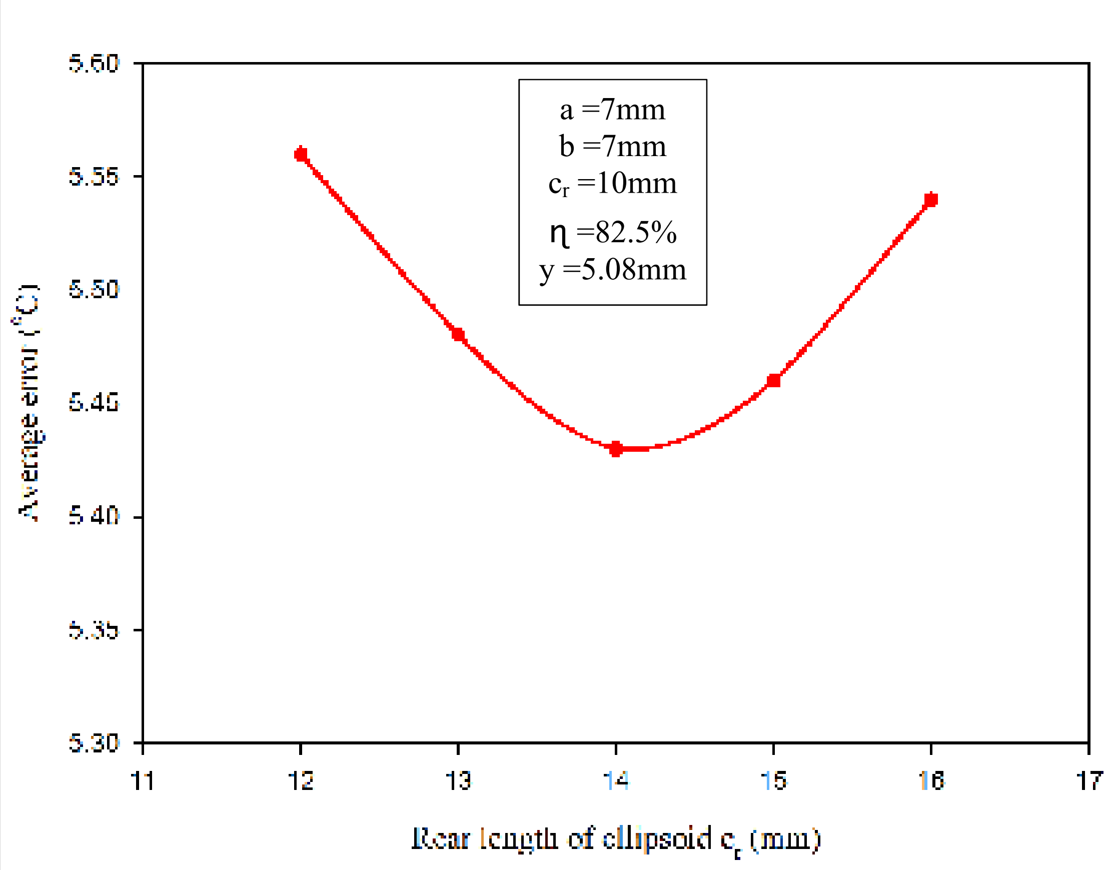

Figure 5.5 The variation of average error based on rear length of ellipsoid (parameter c_r)

Then, efficiency is a crucial parameter in the simulation. An enhancement of the efficiency led to the increase of maximum temperature of plate, widening the size of melted zone. Therefore, several simulations were carried out through different values of efficiency in the range of 81 to 84% to unfold the efficiency dependence of the average error in Figure 5.6. The minimum average error occurred in the efficiency of 82.5%. The applied efficiency is adjusted with an increment of 0.5% in this study.

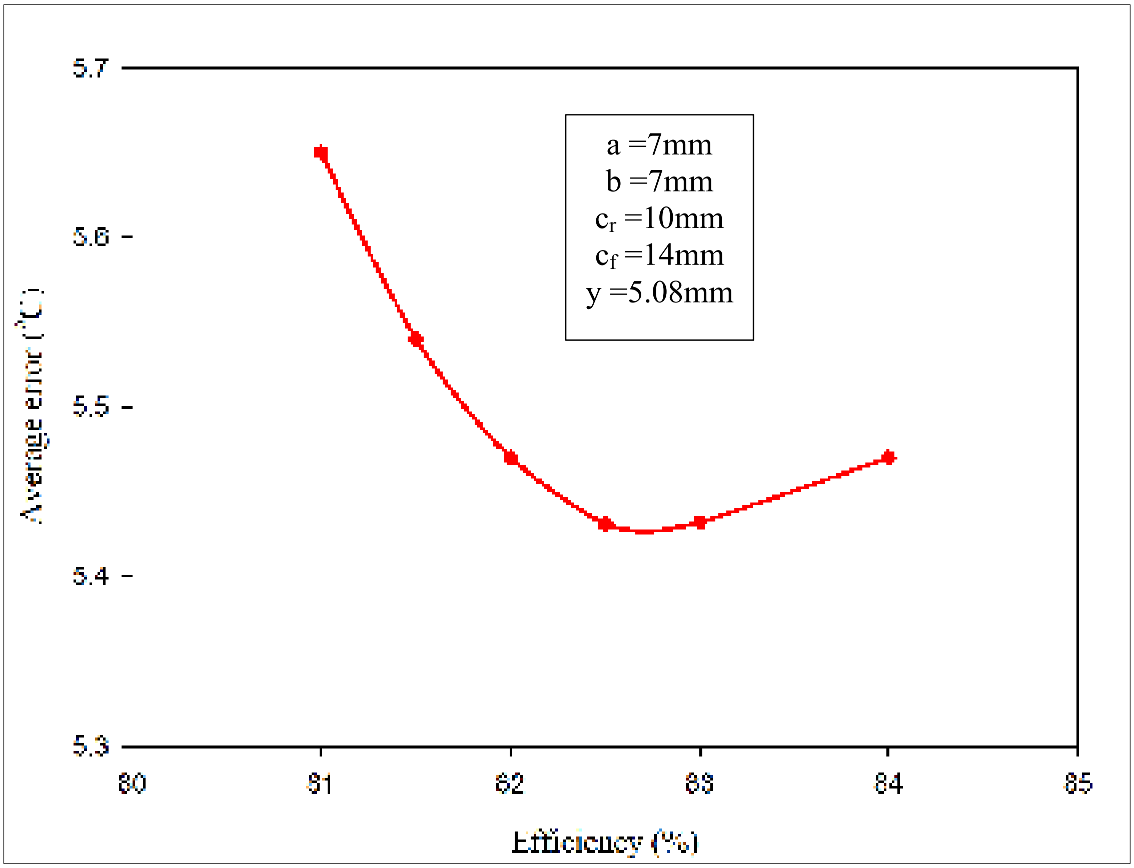

Figure 5.6 The variation of average error based efficiency (parameter η)

The first welding pass was well-predicted through the optimized parameters of the simulation. The optimization of parameters led to the prediction of the maximum temperature, with an average error less than 6°C, according to Table 5.3. Furthermore, the thermal profile was perfectly pursued by the simulation during the cooling process, demonstrated through a comparison between experimentally measured thermal profile and the predicted one in Figure 5.10.

Table 5.4 presents the calculated maximum temperature and the experimentally measured maximum temperature of thermocouples within the first welding pass. The predicted maximum temperatures were lower than the experimentally measured ones at 12 thermocouples of #1, #3, #4, #5, #6, #7, #8, #13, #14, #15, #16, and #20, and larger in the other 8 thermocouples. The maximum error was observed for thermocouple #8, where predicted value is 52°C less than the experimentally detected one. This fluctuation was attributed to the installation of thermocouple, as well as the errors related to the position of thermocouple in the simulations compared to the experimentally installed location, since the location of the thermocouple was measured experimentally. It can be related to the wrong input data (location of thermocouple) in simulation. Furthermore, it was supposed to weld the thermocouples in the bottom of the holes for installing of thermocouples. Nevertheless, it cannot be verified after installation. The minimum error happened at thermocouple #19 with the 3.5°C difference between predicted and measured maximum temperature.

Table 5.4 Comparing calculated maximum temperature and measured maximum temperature of thermocouples for the first weld bead

#	Measured T_{max}	Calculated T_{max}	abs($T_{max(m)}$ -$T_{max(cal)}$)	#	Measured T_{max}	Calculated T_{max}	abs($T_{max(m)}$ -$T_{max(cal)}$)
1	533.75	505.79	27.96	11	321.03	336.84	15.81
2	349.55	365.7	16.15	12	555.1	594.17	39.07
3	248.56	245.29	3.27	13	352.89	345.05	7.84
4	377.47	372.35	5.12	14	291.48	279.76	11.72
5	344.3	332.59	11.71	15	576.33	520.5	55.83
6	561.19	517.24	43.95	16	354.8	354.53	0.27
7	352.24	346.74	5.5	17	259.12	279.85	20.73
8	479.42	426.98	52.44	18	363.74	370.4	6.66
9	756.01	783.04	27.03	19	125.44	128.96	3.52
10	450.14	456.27	6.13	20	106.78	100	6.78

5.2 Adjusting the second pass parameters

This is of great importance to determine the position of the second heat source in the simulations. This was carried out using Goldak's parameters and the efficiency from the first pass. The heat source was not situated in the middle of the plate. X and Y expressed the distance from the middle of the plate and the distance from the tip of the notch (V-preparation), respectively. The coordination of heat source (X,Y) were adjusted in this section to minimize the average error for the second pass of welding process. The predicted shape of melted zone was not changed along the second pass compared to the first pass, as the same parameters applied for the entire simulation. However, the position of molten zone was altered due to the relocation of the heat source within the second welding pass. Table 5.5 presents the average error corresponding to the coordination of the heat source. The coordinates of heat source were determined in the simulation #1, based on the coordinates of a point in the second welding pass.

In simulation #1, the predicted maximum temperature was larger than the measured one for the thermocouples situated at the positive horizontal. The thermocouples localized at the other side of the weld bead revealed the lower maximum temperature by the simulation compared to the measured one. This caused a significant average error in simulation #1. This indicates that the heat source was not placed at the right position. The heat source moved to the middle of the plate in simulation #2. The average error decreased from 39°C to 15°C through the simulation #2. X was assumed -2.54 mm in the simulation #3. Subsequently, the average error was reduced to 9.4°C.

The effect of variation of vertical value was evaluated in simulation #4 where the other parameters were the same as the simulation #2. It was found that, the average error increases upon the increase of the vertical value individually. Therefore, the influence of the increase of vertical value and the reduction of horizontal value were investigated simultaneously in simulation #5 and simulation #6 where X was assumed the same as simulation #3. The increase of vertical value in simulation #6 resulted in less average error. Several possible coordinates of the heat source were investigated within the simulation #7 to #13. Nevertheless, the average errors of those simulations were higher than that of the simulation #6.

Table 5.5 Comparing variation of average error due to the coordinates of second heat source

#Simulation	X(mm)	Y(mm)	Error_{ave}(℃)
1	1.778	8.890	39
2	0	8.890	15
3	-2.540	8.890	9.4
4	0	10.160	17.18
5	-3.048	8.890	9.98
6	-2.540	10.160	7.17
7	-2.540	11.430	10
8	-2.032	10.160	7.4
9	-2.540	9.525	7.8
10	-2.286	10.160	7.22
11	-2.794	10.160	7.2
12	-2.540	9.906	7.32
13	-2.540	10.414	7.19

The parameters in simulation #6 are presented in Table 5.6. The efficiency and Goldak's parameter were considered the same as the first heat source. The coordinates of the second heat source were extracted from simulation # 6, summarized in Table 5.5.

Table 5.6 Adjusted parameters for second heat source

a(mm)	b(mm)	c_f(mm)	c_r(mm)	ɳ(%)	X(mm)	Y(mm)
7	7	10	14	82.5	-2.54	11.43

The coordinates of second heat source were presented as a black point in Figure 5.6. The applied parameters (x, y) were adjusted with an increment of 2.54 mm (0.1 in) in this study. It is noteworthy that a work angle of 55° was imposed to the simulation of the second welding pass to provide the same coordinates as the experiments.

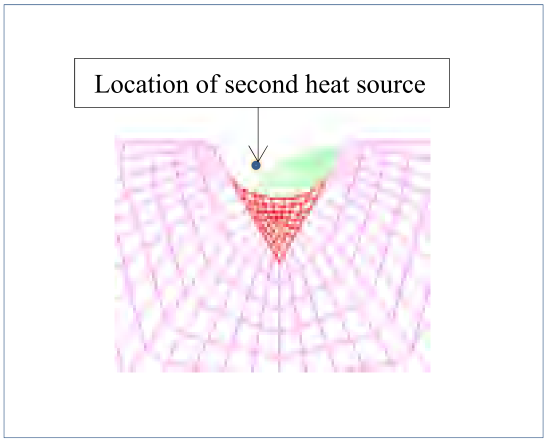

Figure 5.7 The coordinates of second heat source

Section 5.2 addressed the adjustment of the second heat source position. The simulated results showed some errors in predicting the maximum temperature with respect to the experimentally measured data. However, the thermal profile was well-predicted by the simulation during the cooling process.

Table 5.10 presents the predicted and the measured maximum temperature along the second pass of welding process. A considerable difference between the calculated and the measured values were observed in Table 5.10 at few thermocouples.

Table 5.10 Comparing calculated maximum temperature and measured maximum temperature of thermocouples for second heat source

#	Measured T_{max}	Calculated T_{max}	abs($T_{max(m)}$ -$T_{max(cal)}$)	#	Measured T_{max}	Calculated T_{max}	abs($T_{max(m)}$ -$T_{max(cal)}$)
1	326.18	307.80	18.38	11	559.49	556.10	3.39
2	256.48	266	9.52	12	131.52	136.51	4.99
3	215	212.04	2.96	13	132.45	136.97	4.52
4	268.28	270.48	2.2	14	131.15	136.70	5.55
5	253.78	251.47	2.31	15	129.31	136.1	6.79
6	326.42	313.28	13.14	16	750.1	653.19	96.91
7	255.5	259.33	3.83	17	453.32	536.45	83.13
8	723.4	764.51	41.11	18	1372	1003.6	368.4
9	669.95	702.35	32.4	19	148.15	144.81	3.34
10	307.09	316.54	9.45	20	112.98	119.8	6.82

The predicted maximum temperatures were larger than the measured ones at twelve thermocouples in the second welding pass. The minimum average error of 2°C was observed at the thermocouple #4. The maximum error of 368°C occurred at the thermocouple #18. The predicted maximum temperature through the simulation and the experimentally collected value were 1003.6°C and 1372°C at the thermocouple #18, respectively.

This error comes from the incorrect installation of thermocouple or errors related to the measurement of thermocouple position in the experiment. Furthermore, it is attributed to thermocouple detection range which is restricted to the temperature less than 1200℃.

5.3 Adjusting the third pass parameters

In this section, an effort was implemented to determine the position of the third heat source in the simulation. The predicted thermal profiles and the experimentally measured one were compared at different thermocouples to reach the minimum average error. Goldak's parameters and efficiency were the same for the first and the second pass. However, coordinates of the heat source (x,y) were adjusted to minimize the average error along the third pass of welding. Table 5.7 showed the average errors, corresponding to the coordinates of the heat source. X, Y stand for the distance from the middle of the plate and the distance from tip of the notch (V-preparation), respectively.

A positive X was assumed in the simulation #1, simulation #2, and simulation #4. A large average error was observed in these simulations. The average error increased as X was set to zero. However, the extent of melted zone improved compared to the experimental data. Negative X's were applied in the simulation. Subsequently, X and Y were varied to minimize the average error in next simulations. The minimum error of 9.93°C occurred in the simulation #22.

Table 5.7 Comparing variation of average error due to the coordinate of heat source

#Simulation	X(mm)	Y(mm)	$\mathrm{Error}_{\mathrm{ave}}$(℃)
1	2.286	10.16	20.17
2	2.286	8.89	22.09
3	0	10.16	32.38
4	2.54	10.16	45.03
5	-5.08	10.16	17.04
6	-5.08	7.62	19.95
7	-5.08	11.43	19.9
8	-6.35	10.16	35.19
9	-2.54	10.16	18.5
10	-3.81	10.16	11.75
11	-4.064	10.16	10.76
12	-3.556	10.16	12.77
13	-3.81	10.414	11.14
14	-3.81	9.906	12.18
15	-4.318	10.16	10.45
16	-4.064	9.906	11.36
17	-4.572	10.16	11.4
18	-4.826	10.16	14.19
19	-431.8	990.6	10.956
20	-4.318	10.414	10.14
21	-4.318	10.668	10
22	-4.318	10.922	9.93
23	-4.318	11.176	9.96

The applied parameters of simulation #22 were represented in Table 5.10. The efficiency and Goldak’s parameter were considered the same as the first heat source.

Table 5.8 Adjusted parameters for third heat source

a(mm)	b(mm)	c_f(mm)	c_r(mm)	η(%)	X(mm)	Y(mm)
7	7	10	14	82.5	10.922	9.93

The coordinates of third heat source were induced as the simulation #22 from Table 5.7. This was schematically illustrated as a blue point in Figure 5.14. The applied parameter (x,y) are adjusted with an increment of 2.54 mm (0.1 in) in this study.

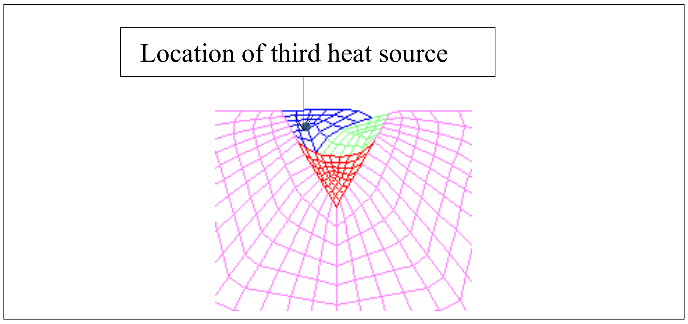

Figure 5.8 The location of third heat source

The average error of the third heat source, 9.93°C, is also reasonably fair. One can observe that, the calculated cooling rate of the third welding pass was tightly close to that of the measured one. The temperature profile of the cooling process was also in good agreement with the experimentally recorded one. The predicted maximum temperature and the experimentally measured one were shown in Table 5.9. Minimum and maximum errors occurred on thermocouples #15 and #7, i.e. 0.9% and 19% respectively.

Table 5.9 Comparing calculated maximum temperature and measured maximum temperature of thermocouples for third heat source

#	Measured T_{max}	Calculated T_{max}	abs($T_{max(m)}$ -$T_{max(cal)}$)	#	Measured T_{max}	Calculated T_{max}	abs($T_{max(m)}$ -$T_{max(cal)}$)
1	470.72	460.80	9.92	11	143.81	141.35	2.46
2	602.46	718.35	115.89	12	126.67	124.74	1.93
3	373.73	417.92	44.19	13	125.26	122.37	2.89
4	1083.2	1028.87	54.33	14	118.71	115.70	3.01
5	488.76	519.87	31.11	15	115.54	114.5	1.04
6	572.22	598.07	25.85	16	355.87	314.82	41.05
7	647.97	770.47	122.5	17	275.35	281.55	6.2
8	152.68	150.17	2.51	18	407.29	359	48.29
9	150.88	148.86	2.02	19	155.54	170.36	14.82
10	147.59	145.69	1.9	20	128.33	136.52	8.19

5.4 Results for measured and calculated temperature profile of thermocouples

Figure 5.10 gives the measured maximum temperature of the embedded thermocouples as compared to the simulation. The plate was initially heated to 100°C, prior to the welding process. An increase in temperature of the preheated plate was recorded through the thermocouples upon welding. The temperature at the thermocouple decreased as the torch passed by. The second welding pass started as the mean temperature level dropped below 125°C, the same as experimental procedure. The thermocouples, which were situated far away from the second heat source, exhibited no temperature rise during the second pass. This is attributed to the shorter length of the second pass compared to that of the first one. The third welding pass was performed at the interpass temperature of 125℃, the same as experimental procedure. The length of the third pass was also less than that of the second one. Therefore, larger number of thermocouples showed no temperature change during the third pass, compared to that of the second welding pass.

The initial temperature, as well as the time interval of the consecutive passes was provided to the model. The predicted maximum temperatures were fairly consistent with the measured values. However, several errors were detected, as summarized in Table 5.4, Table 5.7 and Table 5.9. Nevertheless, the model precisely predicted the temperature profile during the cooling process. The applied time interval was optimized to achieve the most accuracy of predicted data over a reasonable processing time. The accuracy improved as the time interval was decreased however, the simulation was more time-consuming.

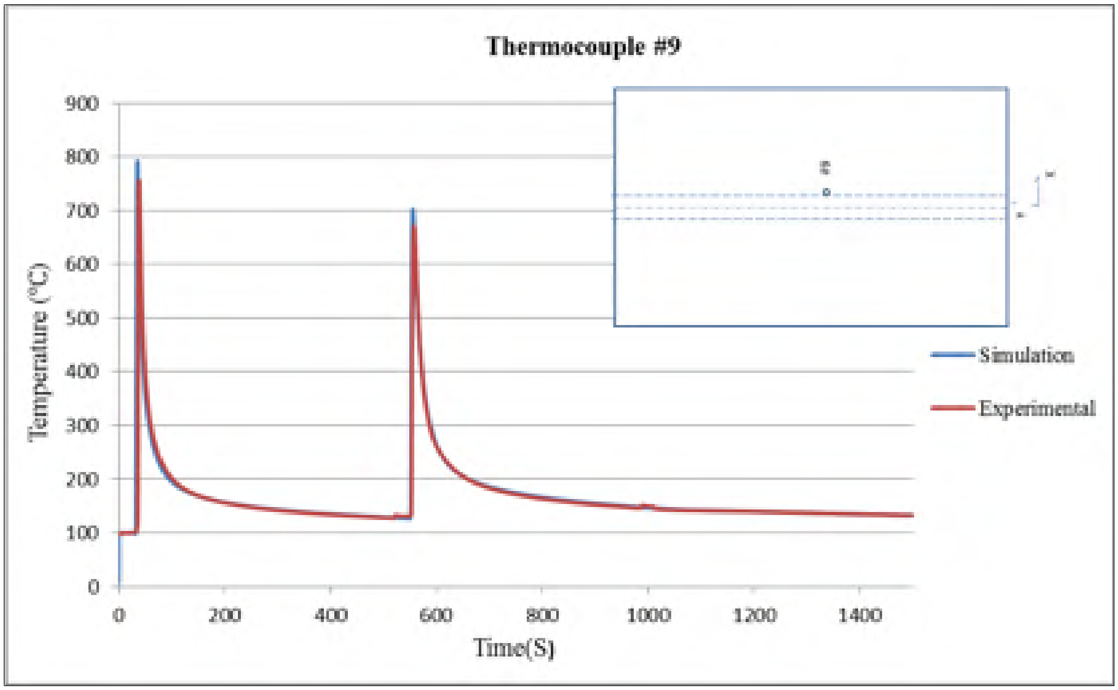

Figure 5.9 Thermal profile of thermocouple #9 during multi-pass welding

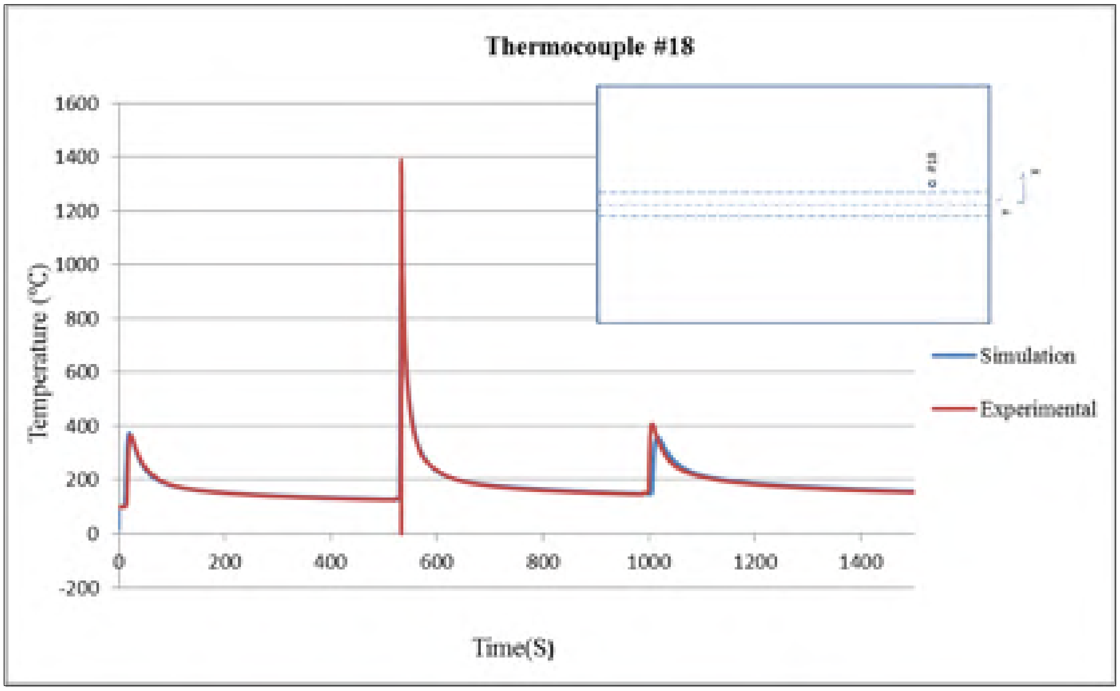

Figure 5.10 Thermal profile of thermocouple #18 during multi-pass welding

5.5 Heat affected zone

Figure 5.11 shows the microstructure of the fusion zone and the heat affected zone at the first welding pass. The extent of the melted zone also is shown on the right.

One can observe that, the model could not predict the configuration of the melted zone on the edges. This is attributed to the distribution of Gaussian power density in the edge of ellipsoid which at the limit is only 5%. Furthermore, the heat source did not comprise the edges of the cross-section, as the welding applied on the V-preparation. Move tip of torch along y, elaborate this modification led to a more accurate prediction of the melted zone configuration. However, the position of heat source, considered in the model, was far from where it was located during the experiment.

A hole was observed at the center of notch. The hole developed due to the lack of penetration of the heat source through the V-preparation.

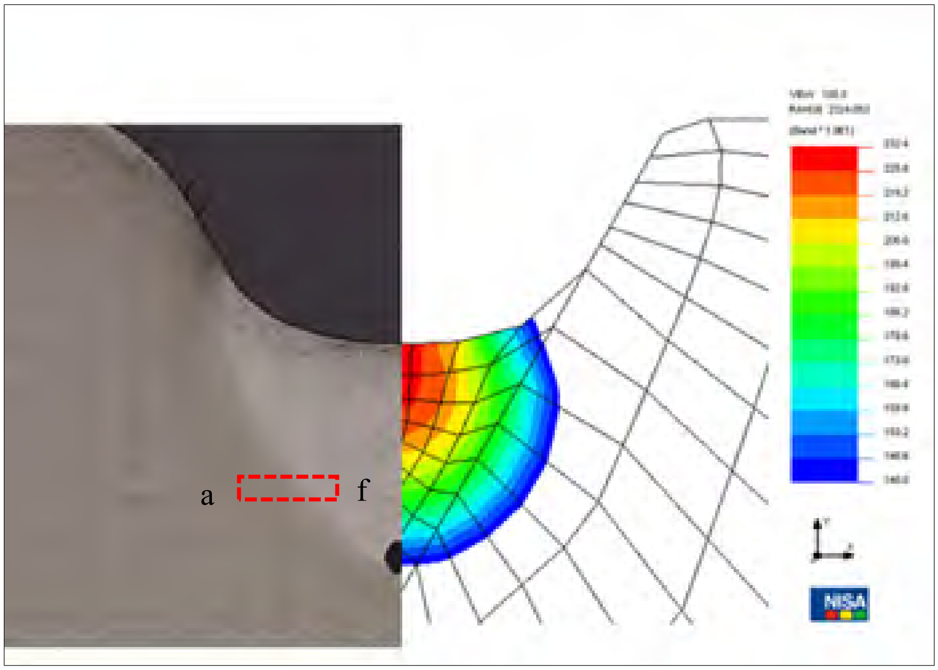

Figure 5.11 Experimental vs. calculated values of the size of the melted zone

Figure 5.12-a shows the micrograph of the base metal, predominantly composed of martensite. It has been demonstrated by Thibault *et al* [62] the martensite of base metal partially transformed into austenite at the border of heat affected zone, Figure 5.12-b. In the neighbouring region in Figure 5.12-c, martensite completely turned into austenite. The observed phase transformations are consistent with the predicted temperature distribution along the width of V-preparation. The measured micro-hardness map, in Figure 5.13, reflects the observed phase transformation in Figure 5.12.

.

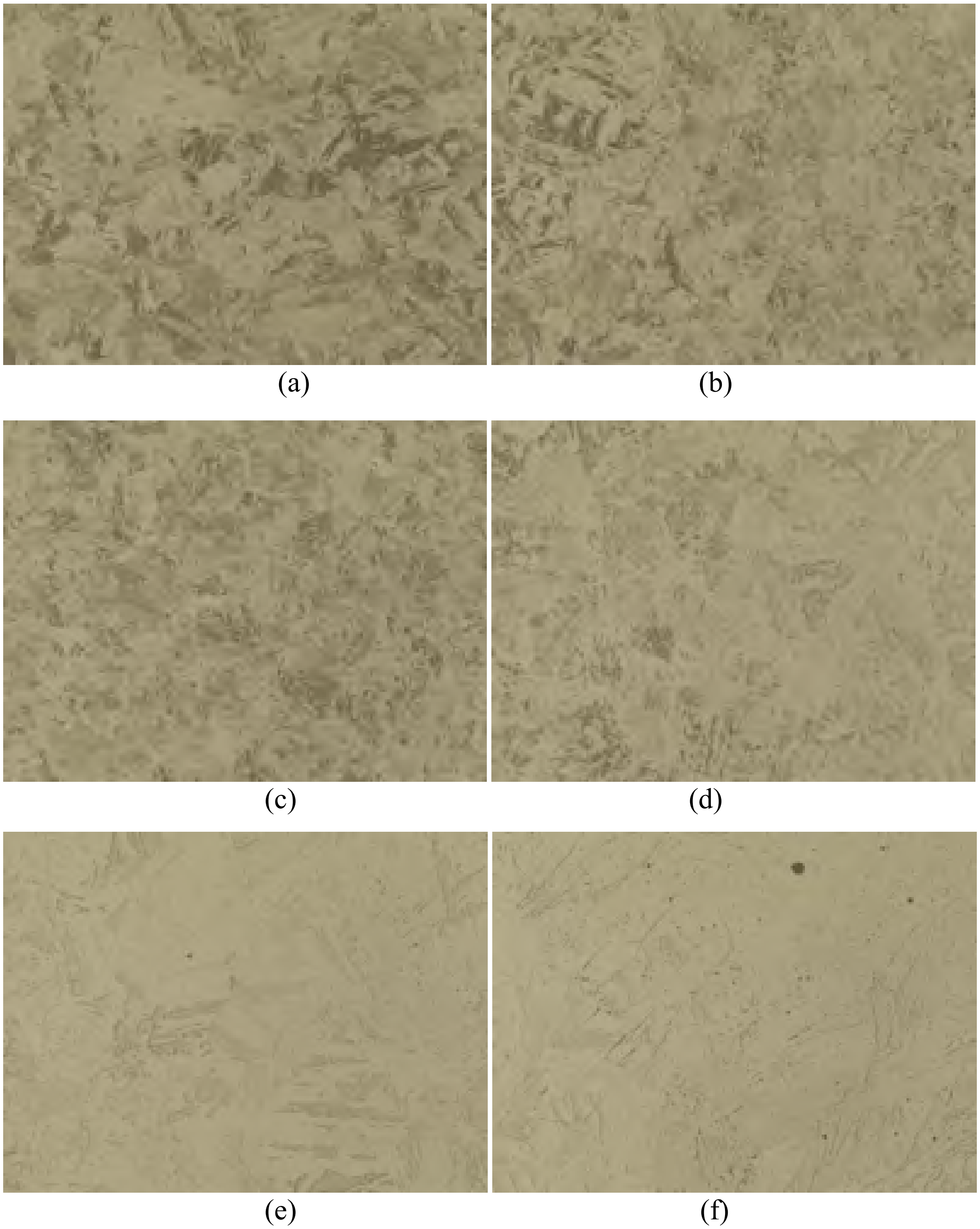
(a) (b)
(c) (d)
(e) (f)

Figure 5.12 Microstructure of heat affected zone

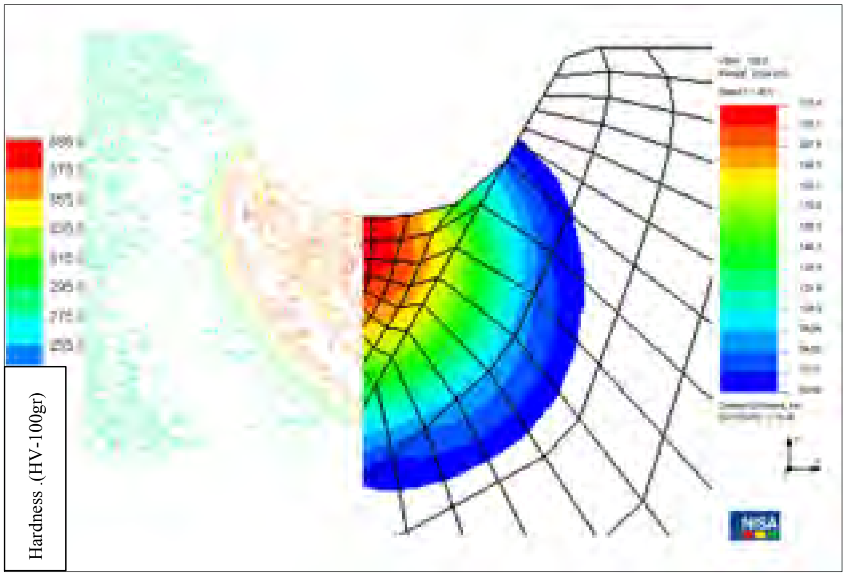

Figure 5.13 Micro hardness map of first welding

5.6 Results of reproduction & comparison of micro hardness

At last, the reproducibility of the predicted temperature profile was investigated. The predicted temperature profiles at some given nodes of the plate were experimentally induced on small specimens of the same composition. Subsequently, the micro-hardness of these components was measured and compared to the micro-hardness predicted by the map at the location of the given nodes. Therefore, the reliability of the simulation would be by the prediction of the hardness in reconstituting the thermal history of a node. Figure 5.14 shows the predicted temperature profile along with the experimentally measured ones. The predicted maximum temperature and the measured one were overlapped in Figure 5.14. However, the predicted cooling rate was different from the measured one through the welding experiments. One can observe in Figure 5.14 that, the predicted cooling by the simulation is faster than that of the experimentally recorded one.

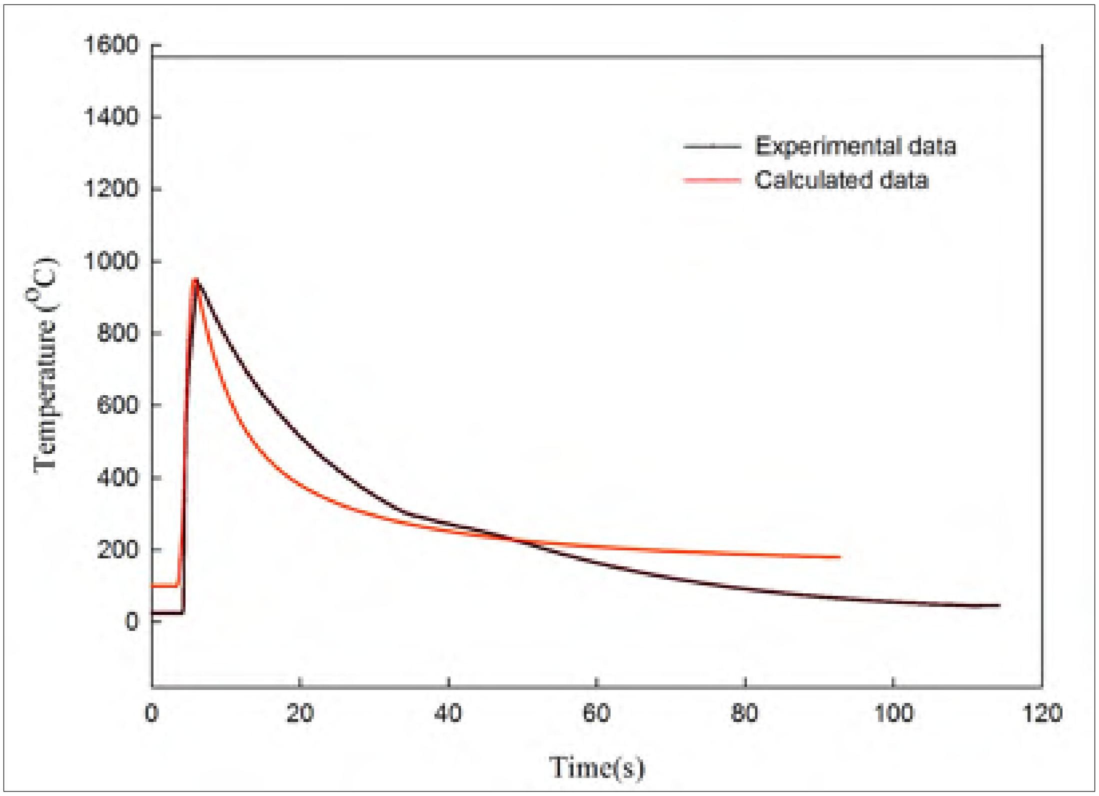

Figure 5.14 A sample of calculated thermal profile and experimental thermal profile

The cooling rate of the small specimens could not faithfully reproduce the profile of the simulation despite using Argon gas and, alternatively, Helium gas and compressed air. Therefore, it was suggested to compare the micro-hardness based on the integration of temperature with time, instead of maximum temperature. The integration was calculated using Equation (5.2), where I is integral (°C.s), *t* is time (s) and *T* is temperature (°C).

$$I = \int_{t_0}^{t} T dt \quad \text{for} \quad 600°\text{C} < T < T_{max} \tag{5.2}$$

The integration was executed from 600^{o}C to the maximum temperature as a contour, since the phase transformation occurs at the temperature above 600^{o}C. Figure 5.15 illustrated the integrated area within the aforementioned range in equation (5.2). The black shaded area, corresponding to the integration of the experimentally recorded data, is wider than the red shaded area, related to the predicted thermal profile, due to a slower cooling rate.

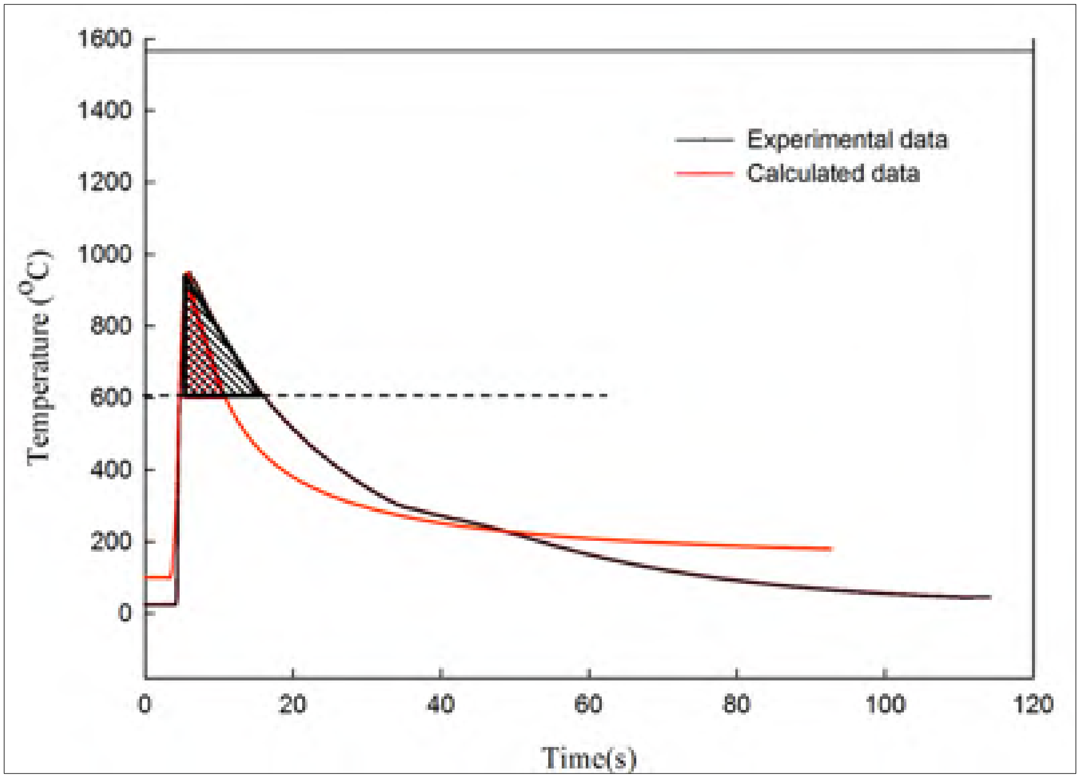

Figure 5.15 Schematic picture of calculated integral

Table 5.10 summarizes the integrated criterion of the 8 thermal profiles of the given nodes in the second column, as well as, their maximum temperatures in the first column. The third column in Table 5.10 shows the measured hardness, corresponding to the position of nodes along the plate. The fourth, fifth, and sixth column of Table 5.10 give the maximum temperature, the integrated criterion, and the hardness of the small specimens.

Table 5.10 Integral of 16 thermal profiles and their maximum maximum temperatures

FEM		Experiment	Samples		
Tmax(˚C)	Integral(℃.s)	Hardness(HV)	Tmax(˚C)	Integral(℃.s)	Hardness(HV)
603	602	279	593	0	273
662	2269	285	727	3419	280
796	3989	288	803	5104	286
821	4092	317.5	832	5249	307
1017	5345	332	853	5275	338
1134	6206	344	934	6401	356
1380	7552	353	948	8791	364
1438	7788	352	1008	7737	361

The predicted and experimentally measured results were represented concurrently in Figure 5.16. The hardness increased gradually with the integrated criterion. Then, a sudden increase was observed at a critical integrated value, known as the threshold hereinafter, proportional to a certain temperature. However, the increment levelled off at higher integrated values, regarding the experimentally measured data. The predicted data reached the threshold at a lower integrated criterion, around 4000 °C.s, compared to that of the experimentally measured data, around 5100 °C.s. Furthermore, the ultimate hardness for predicted data was slightly lower than that of the experimentally measured data. The difference between these two behaviors was derived from the thermal stresses developed in the plate during welding procedure. It was assumed that thermal stresses caused phase transformation at lower temperatures in the plate during welding. Therefore, the measured hardness levelled off at lower integrated criterion (lower maximum temperature) due to the thermal stresses. The small specimens were surrounded by the provided atmosphere, unlike the corresponding material in the plate that has been surrounded by the cold metal during the welding process of the plate. Consequently, no thermal stress was developed in the small components due to the absence of the considerable thermal expansion difference.

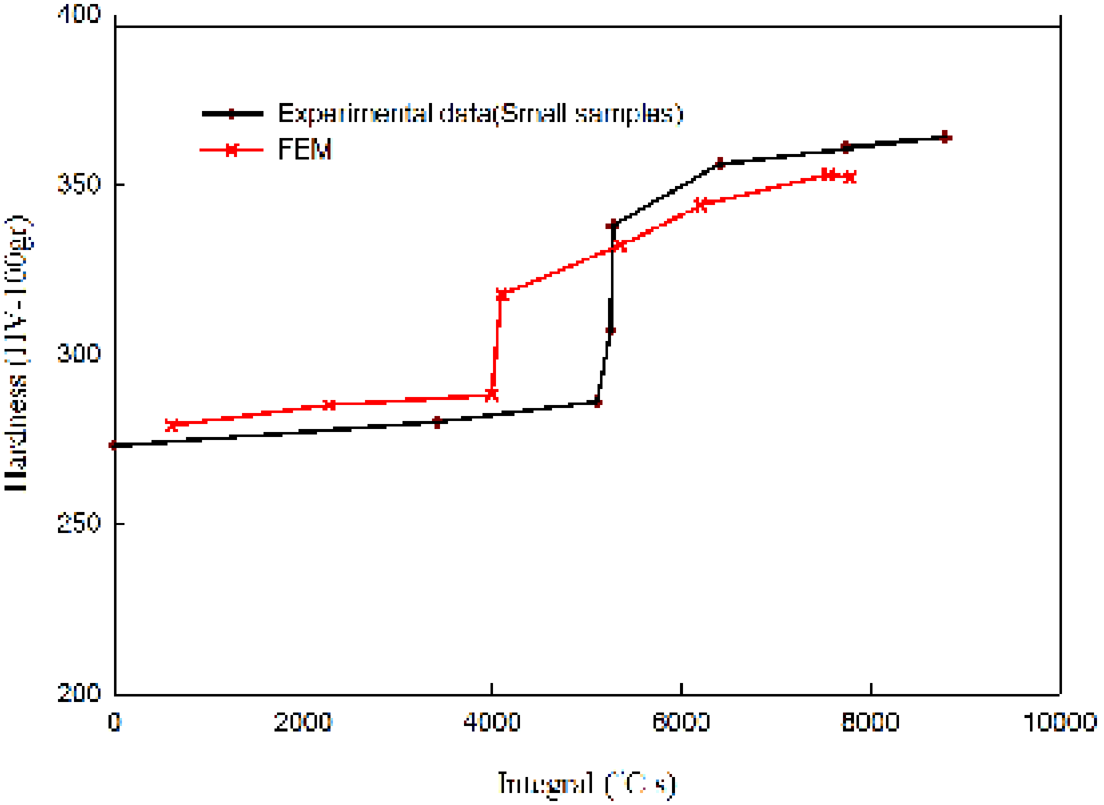

Figure 5.16 Measured hardness vs. calculated integral

CONCLUSION

In this thesis, a finite element model for predicting the temperature field induced by multi pass welding process was validated. To achieve the main goal, three specific objectives were defined. The first objective was to measure the specific heat and conductivity coefficients for stainless steel 415 to be applied in the simulation, as there is no certain values from literature review for this material. Different values have been assumed during cooling and heating process according to measured data. The second objective was to verify the predicted temperature distribution at 20 given nodes. The simulated thermal profiles were compared to the experimentally measured ones through the installed thermocouples during welding. Furthermore, the accuracy of the thermal simulation was evaluated through the comparison of a 2-dimensional cross-section of the heat affected zone microstructure in the plate with the simulated melted zone configuration.

The third objective was to spread the validity evaluation of the simulation to any given nodes throughout the welded plate, by inducing the predicted temperature profile to the small specimens, and subsequently comparing the resultant micro hardness of the small specimens to the measured corresponding node along the plate.

In the first part, measured conductivity and specific heat of stainless steel 415 were substituted into the simulation. Within the next step, it was demonstrated that the model is able to precisely predict the temperature profile during the cooling and heating process for multi-pass welding through comparison of the calculated thermal profile with the measured one by the thermocouples. This means that the heat transfer process is fairly predicted by this simulation procedure during the welding.

In the second part, Goldak's parameters, efficiency of heat source, and position of heat source were adjusted through comparing the predicted shape of fusion zone to the experimentally measured maximum temperature of the thermocouples. The main objective was met using this continuous simulation for a three pass welding in this study. The average errors of 5.43, 7.17 and 9.93°C were calculated for the first, the second, and the third welding pass, respectively. It was found that the provided time to reach the maximum temperature in the simulation is adequate. The maximum error occurred in calculating maximum temperature of thermocouple#18 in second welding pass of 360°C. This error was attributed to either the incorrect installation of thermocouple or the wrong data from experimental measurement, originated from the restricted measurement accuracy at temperatures above 1200°C in the k-type thermocouples.

The predicted configuration of melted zone was compared to the microstructure of cross-section of the welded plate to validate the simulation. The results indicated that the shape and size of the measured melted zone were tightly close to the one predicted by the simulation. However, the edges of the melted zone were not perfectly figured due to the V-groove preparation.

At last, the temperature profiles, corresponding to eight selected nodes in the heat affected zone, were reproduced in the small specimens of the base material. The micro-hardness was correlated using the integration of temperature with time in the small specimens. The criterion was applied to compare the measured micro-hardness with the selected nodes to validate the simulation at heat affected zone. The measured micro-hardness of small samples and corresponded nodes in the plate were disclosed in base material and filler metal. However, there is a gap in the measured hardness of heat affected zone, it is assumed that is corresponded to the thermal stress in the welded plate.

This study demonstrated that the finite element models are able to predict temperature distribution during multi pass welding process in V-groove preparation using Goldak's model. Therefore, the re-adjustment of input parameters, as well as, the assumption of the different physical properties during cooling and heating is applied.

RECOMMENDATIONS

- Modeling of the residual stress field is suggested to shed light on the dark spots of the welding process in future studies.
- It is crucial to investigate the mechanical properties on stainless steel 415 in order to predict the welding distortion.
- The heat source can be considered far from the V-preparation. Moreover, the three or four times larger ellipsoids can be assumed, since Goldak's ellipsoid model could not predict the configuration of the melted zone on the edges as the welding induced on the V-preparation.
- The constant distribution can be used instead of Gaussian distribution to better predict the edge of molten zone. The reason is that only 5 % of heat input is applied on the edge in Gaussian distribution.

APPENDIX I

MELTED ZONE IN FIRST WELDING

Appendix I provides the results obtained from the simulation for melted zone in first welding pass.

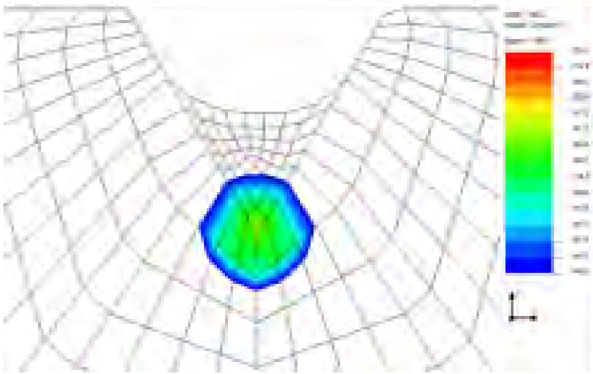

Simulation #1

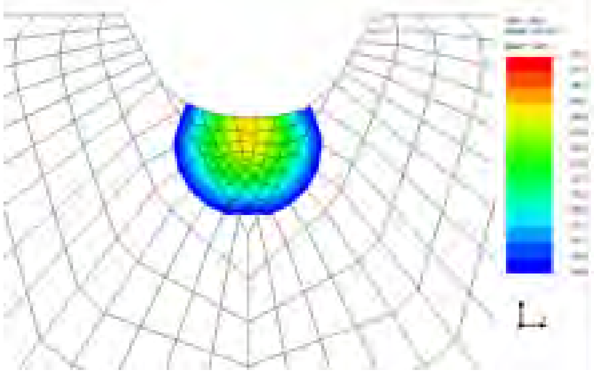

Simulation #2

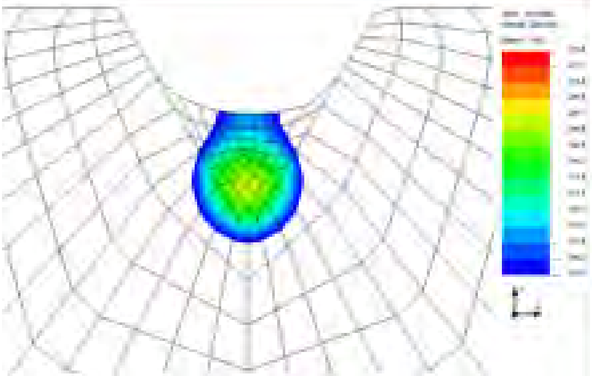

Simulation #3

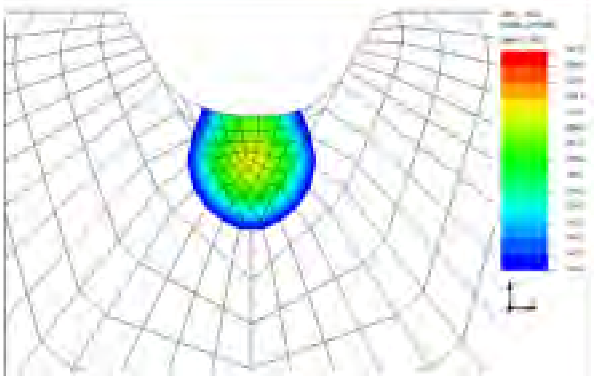

Simulation #4

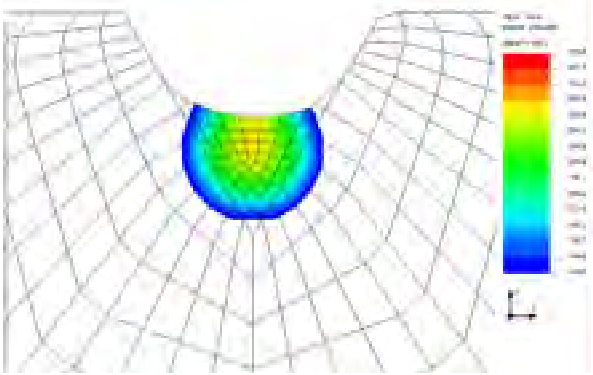

Simulation #5

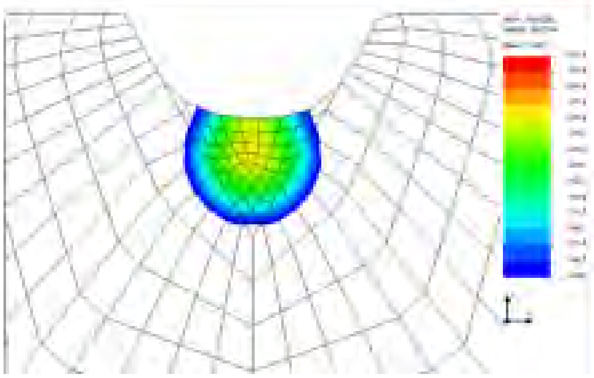

Simulation #6

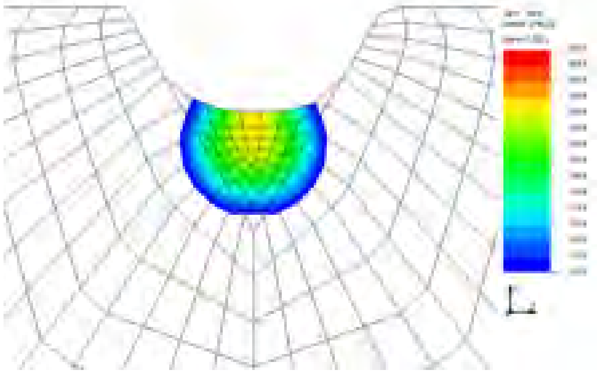

Simulation #7

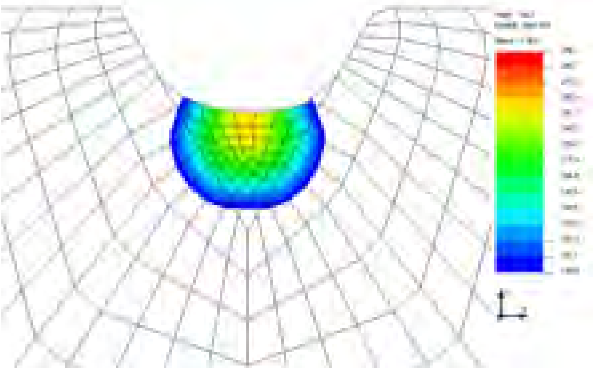

Simulation #8

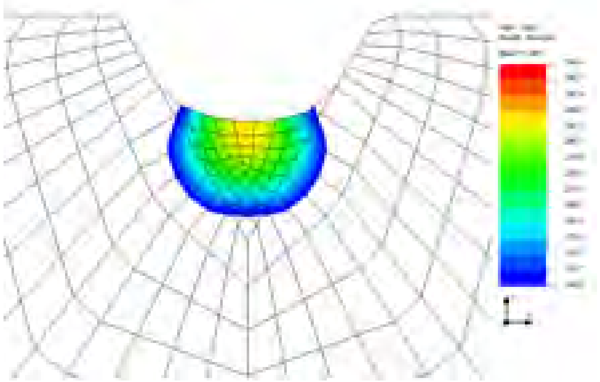

Simulation #9

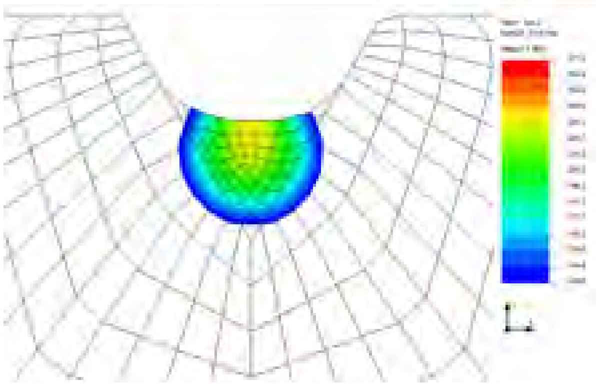

Simulation #10

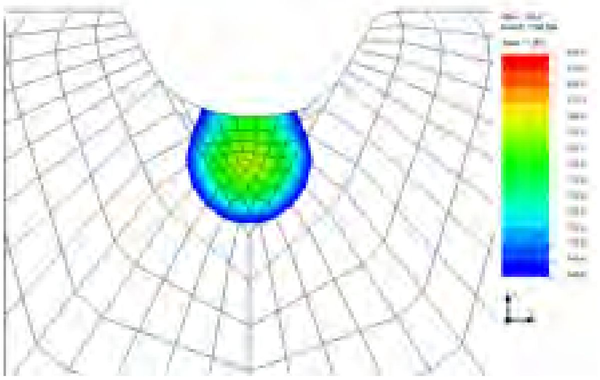

Simulation #11

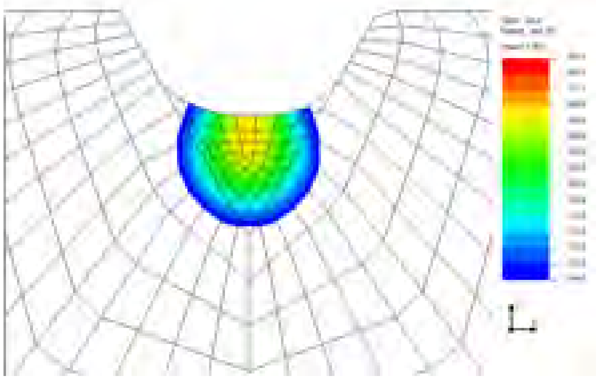

Simulation #12

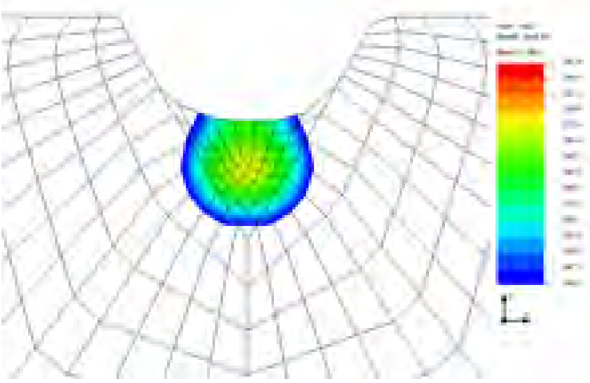

Simulation #13

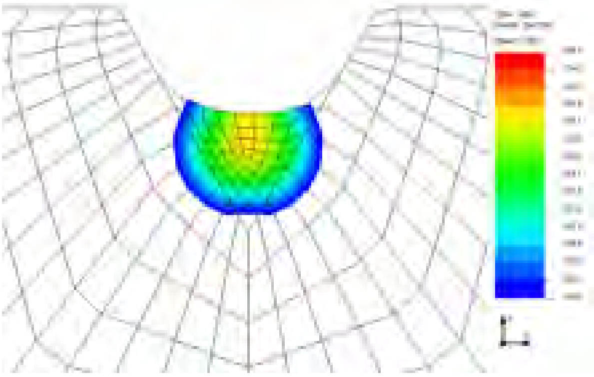

Simulation #14

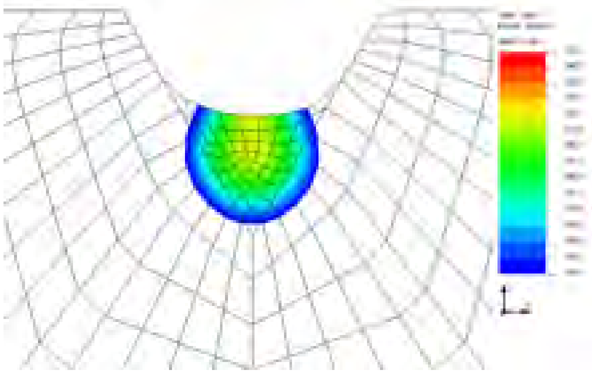

Simulation #15

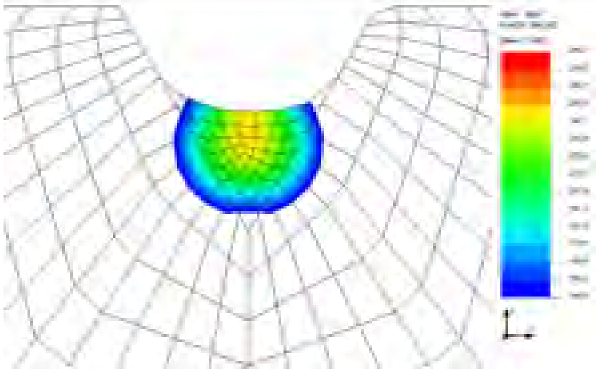

Simulation #16

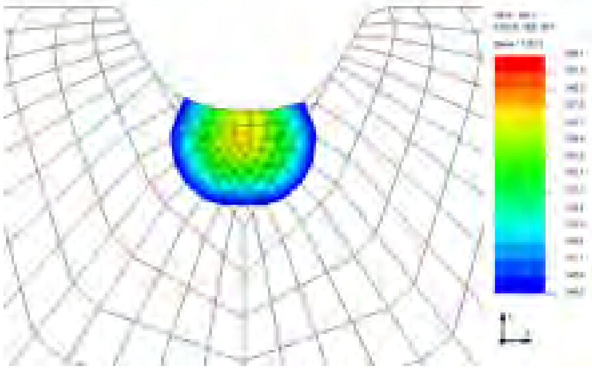

Simulation #17

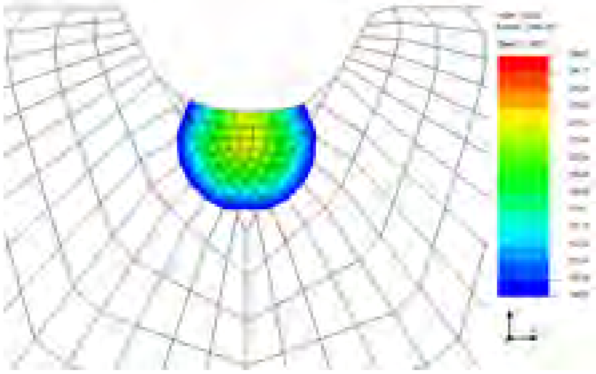

Simulation #18

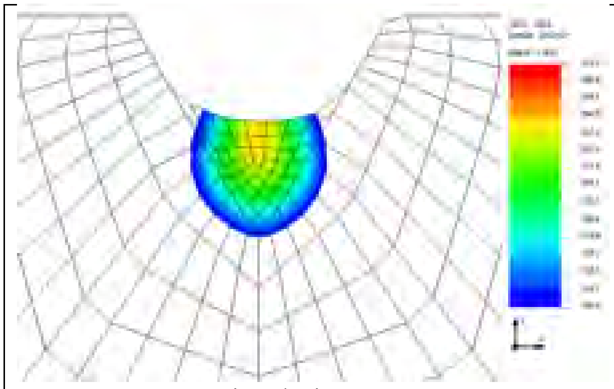

Simulation #19

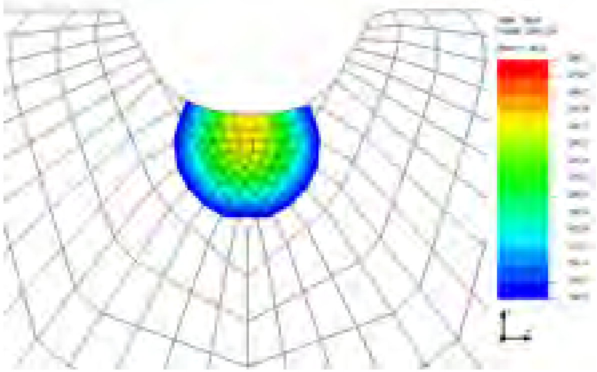

Simulation #20

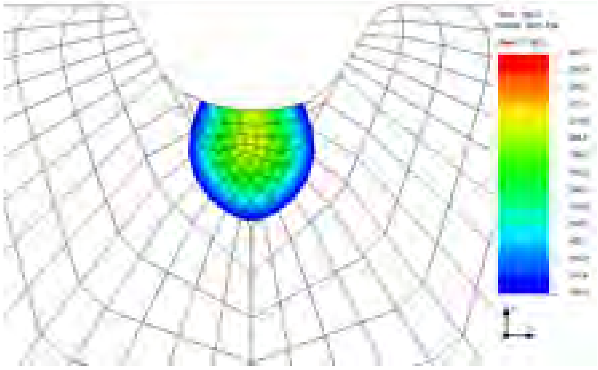

Simulation #21

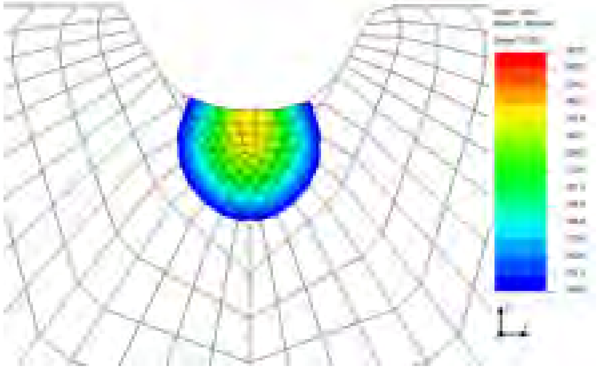

Simulation #22

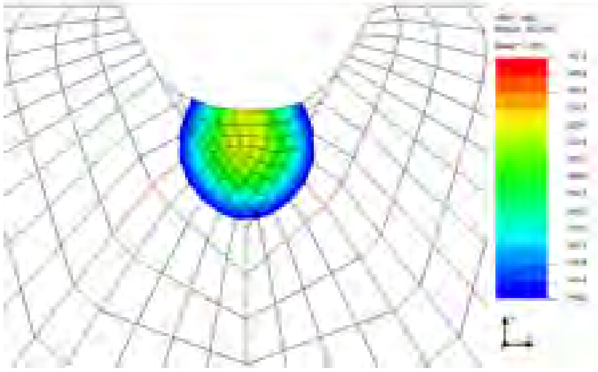

Simulation #23

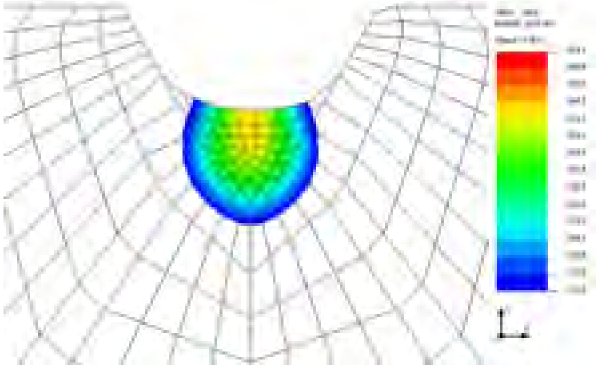

Simulation #24

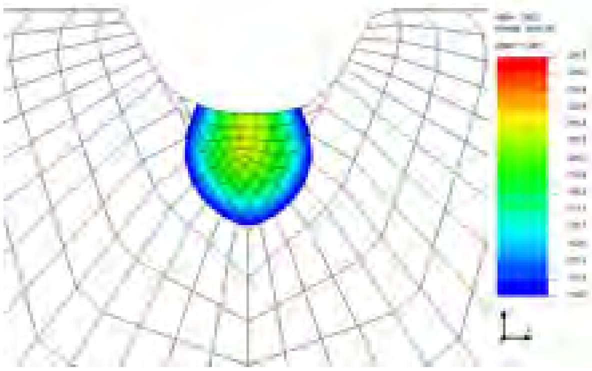
Simulation #25

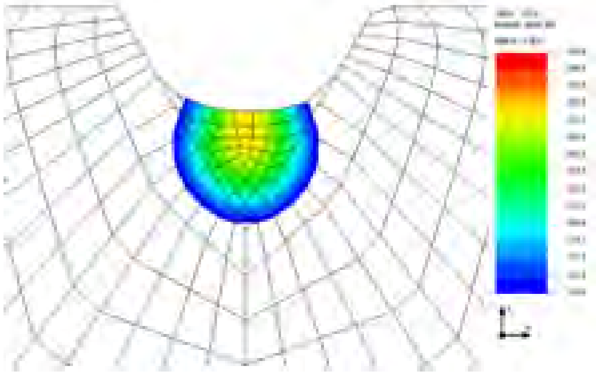
Simulation #26

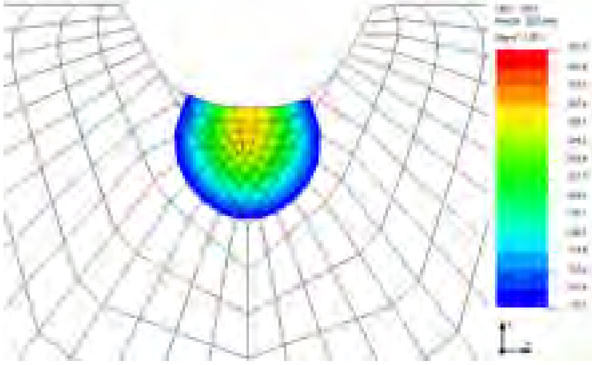
Simulation #27

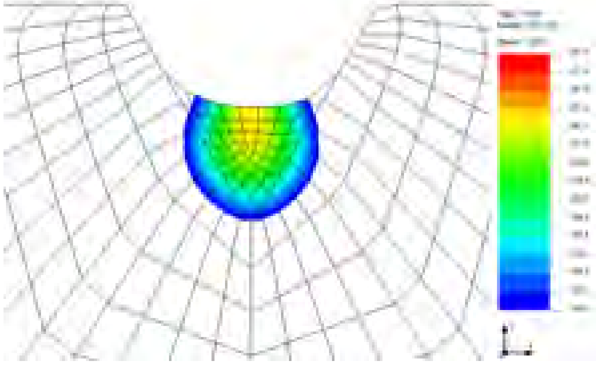
Simulation #28

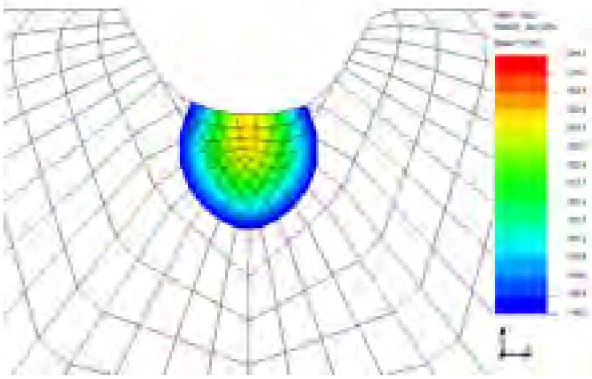
Simulation #29

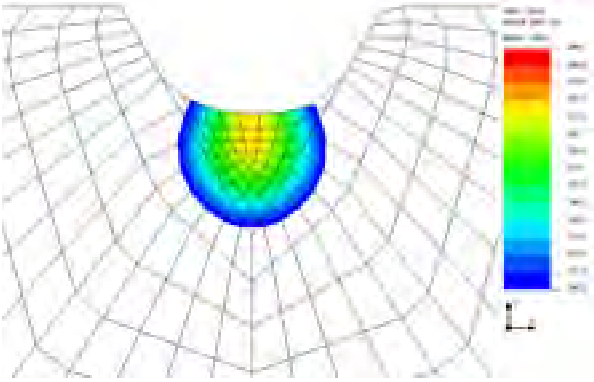
Simulation #30

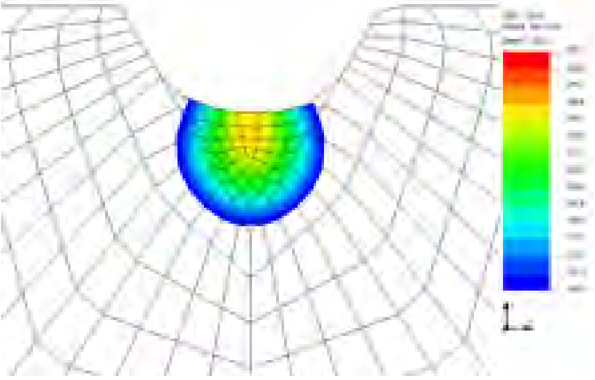
Simulation #31

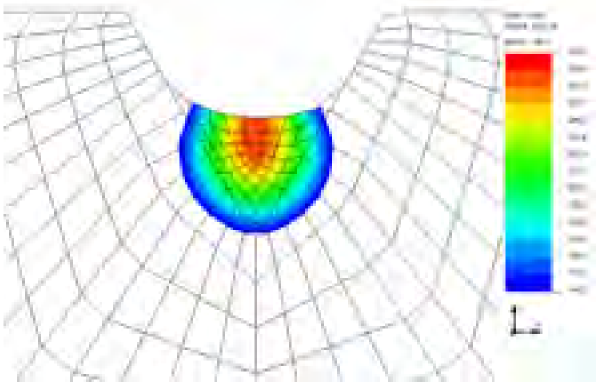
Simulation #32

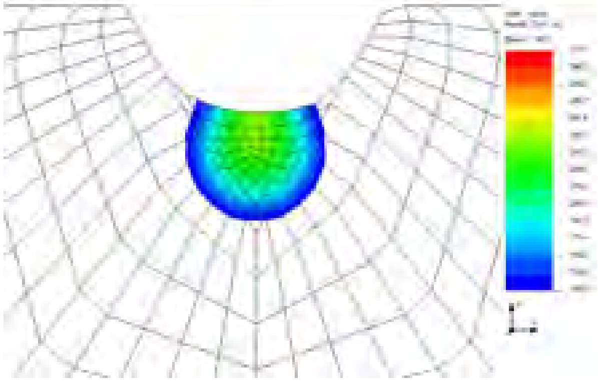
Simulation #33

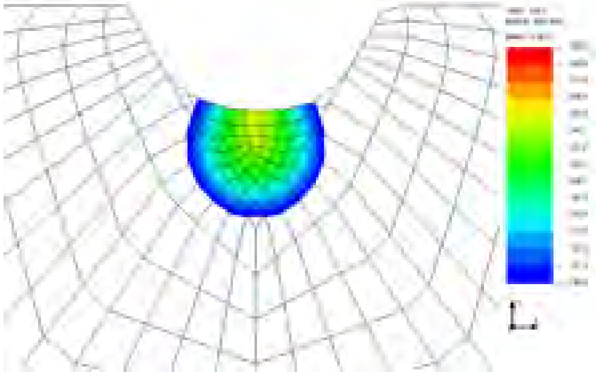
Simulation #34

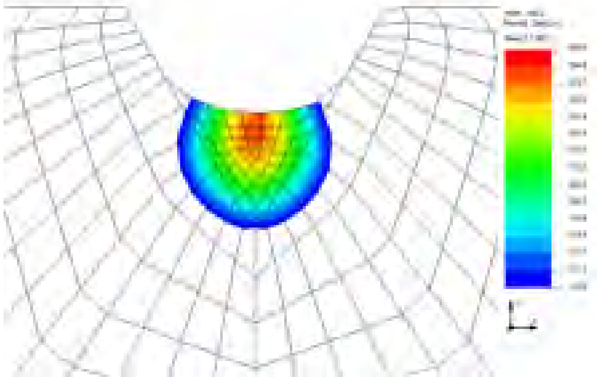
Simulation #35

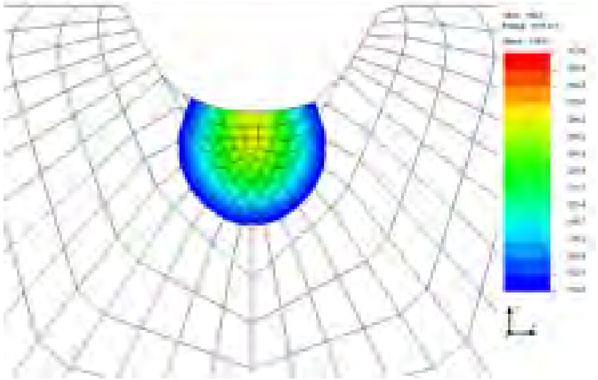
Simulation #36

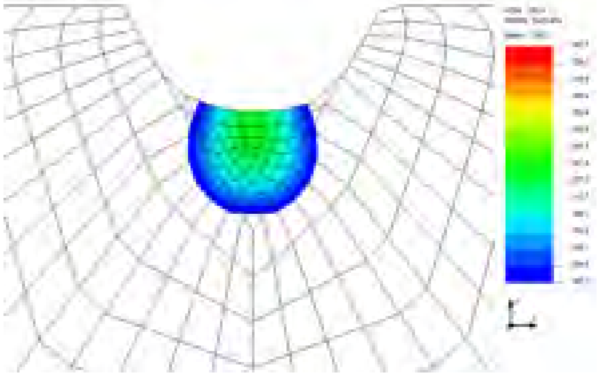
Simulation #37

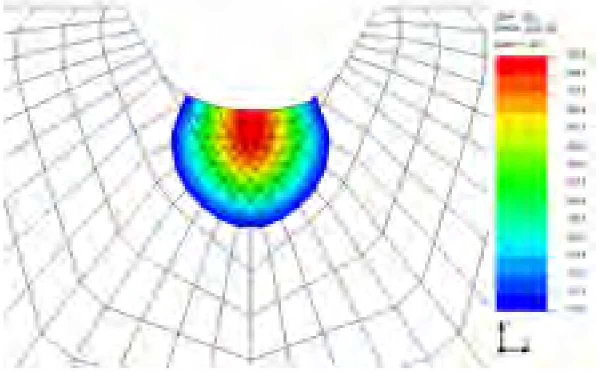
Simulation #38

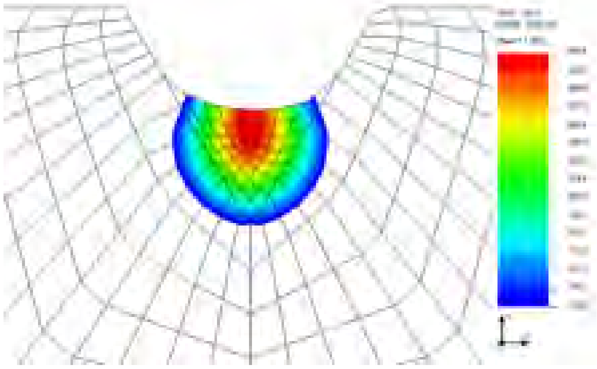
Simulation #39

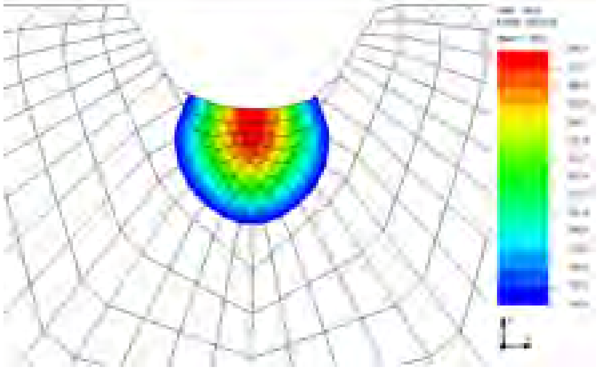
Simulation #40

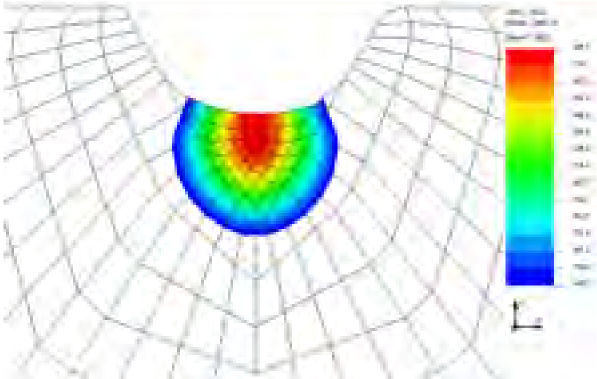
Simulation #41

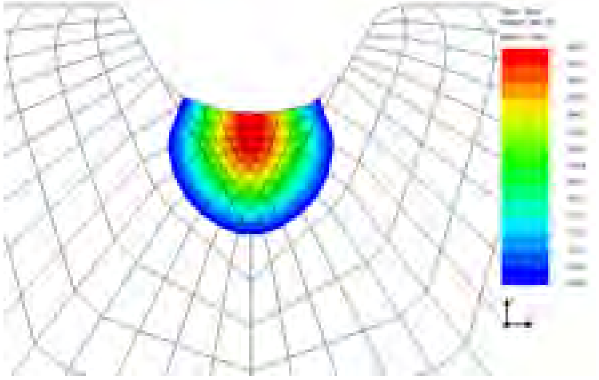
Simulation #42

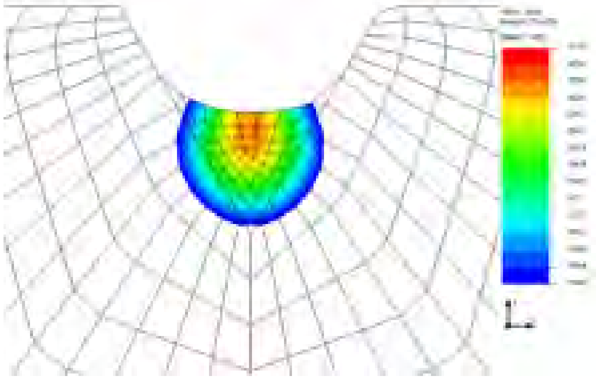

Simulation #43

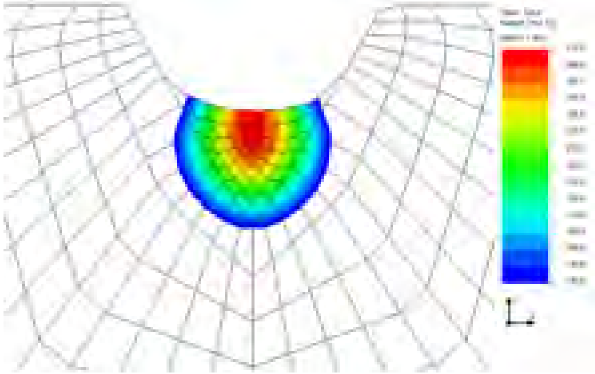

Simulation #44

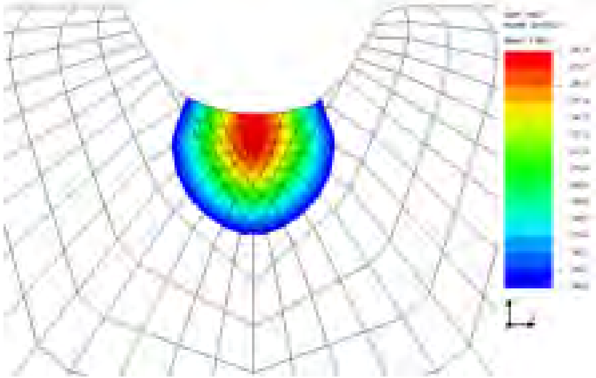

Simulation #45

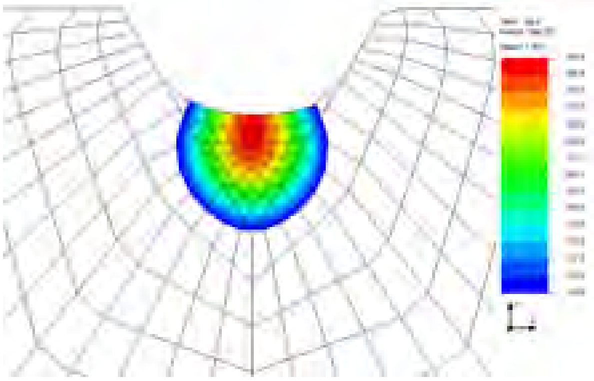

Simulation #46

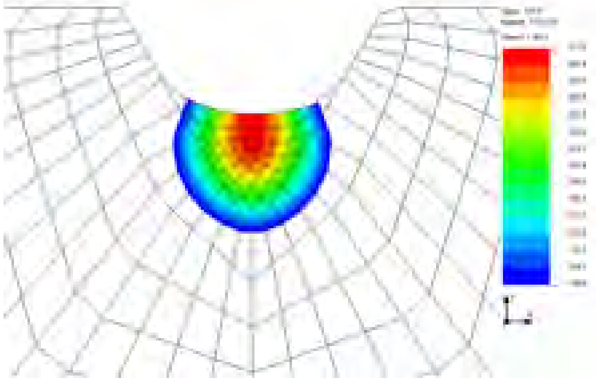

Simulation #47

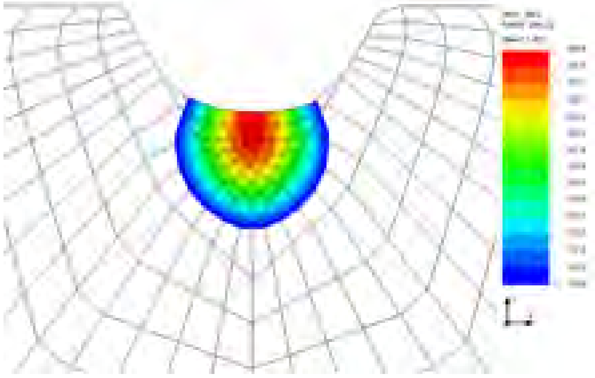

Simulation #48

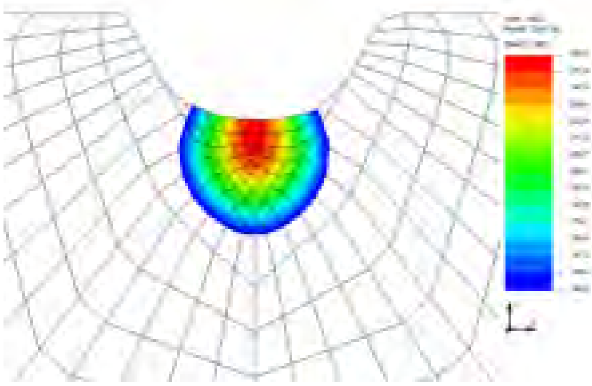
Simulation #49

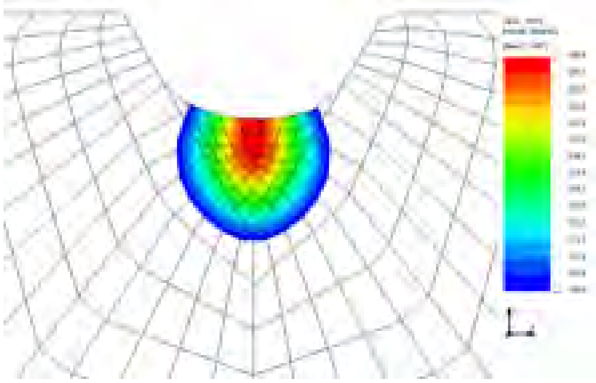
Simulation #50

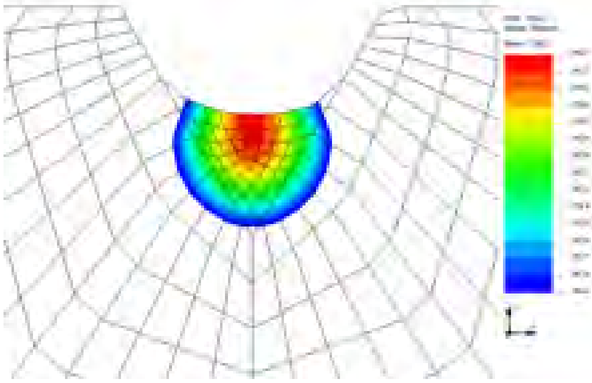
Simulation #51

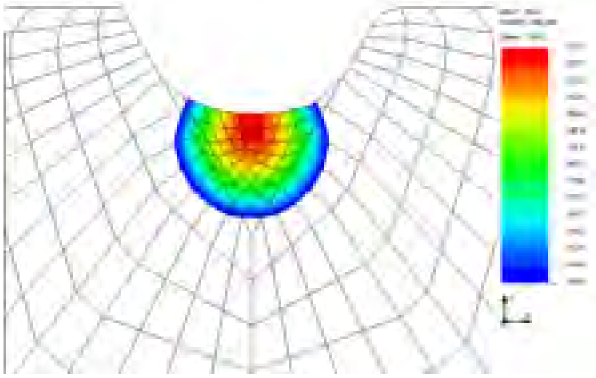
Simulation #52

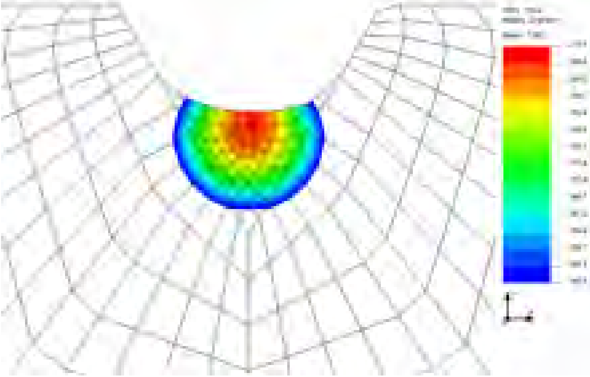
Simulation #53

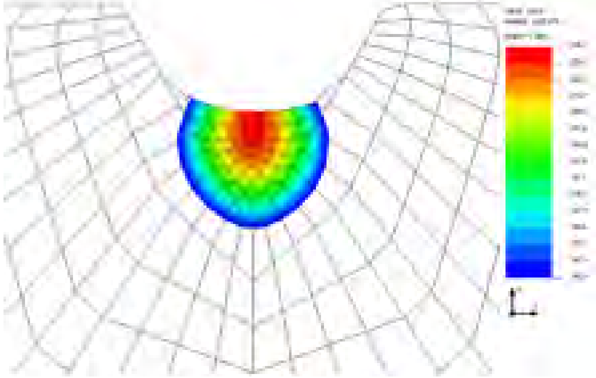
Simulation #54

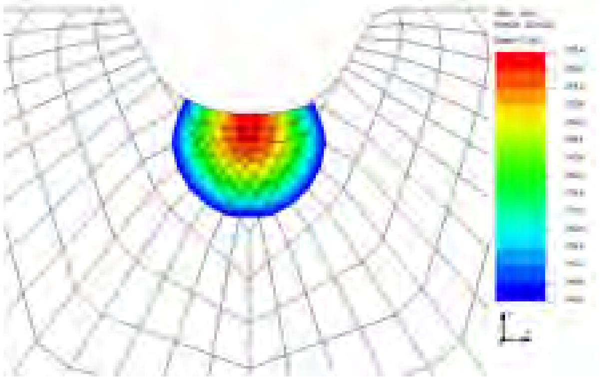

Simulation #55

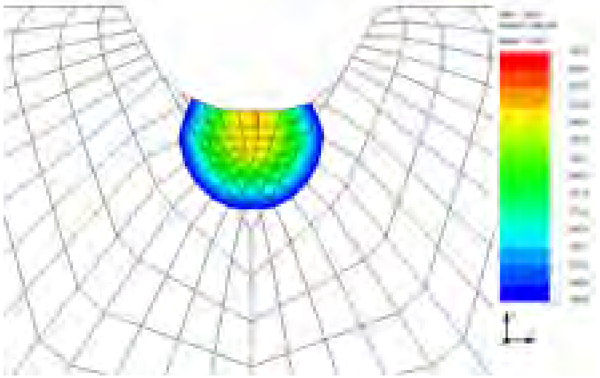

Simulation #56

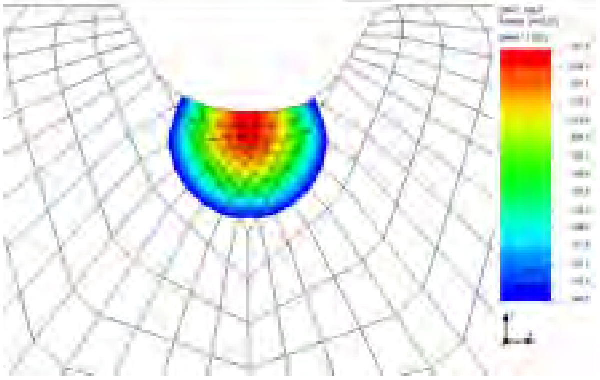

Simulation #57

APPENDIX II

MEASURED MAXIMUM TEMPERATURE AND CALCULATED MAXIMUM TEMPERATURE OF THERMOCOUPLES

Measured maximum temperature and calculated maximum temperature of thermocouples are presented in appendix II.

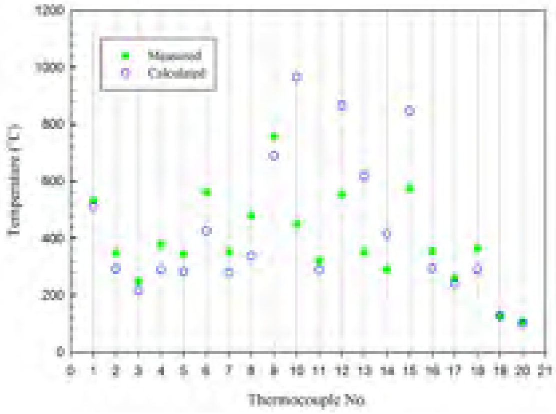

Simulation #1

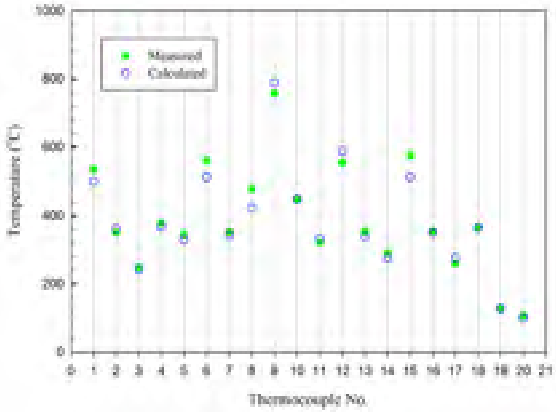

Simulation #2

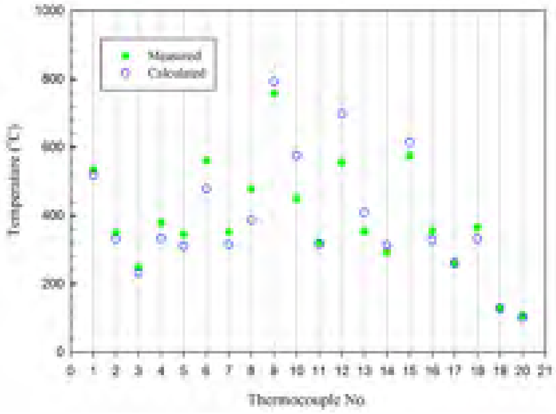

Simulation #3

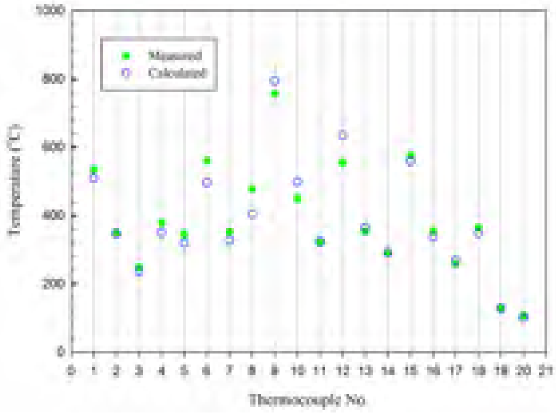

Simulation #4

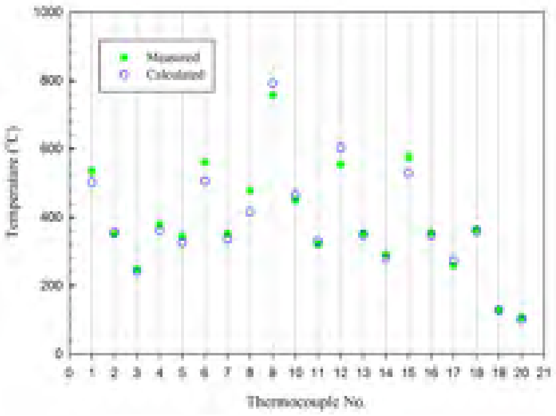

Simulation #5

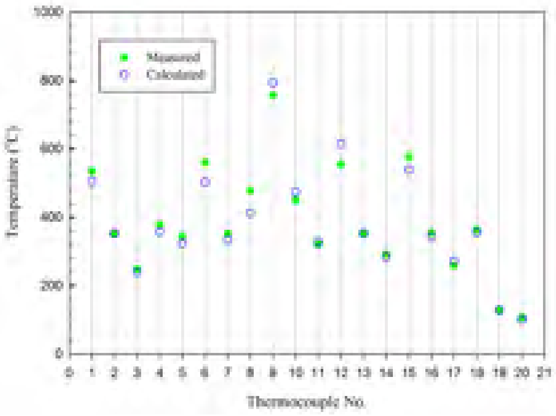

Simulation #6

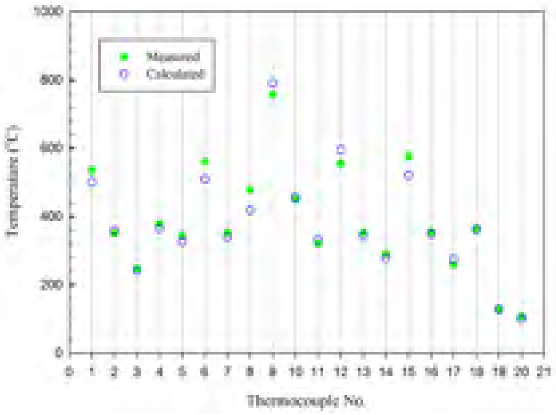

Simulation #7

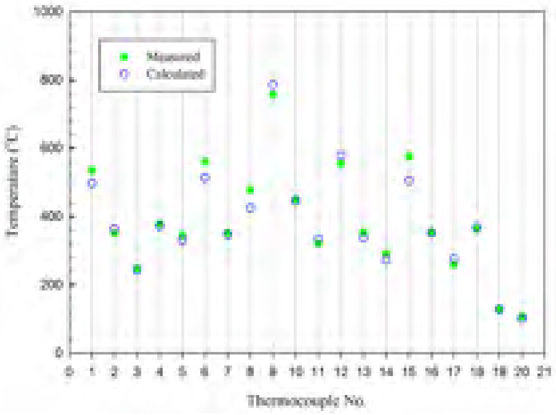

Simulation #8

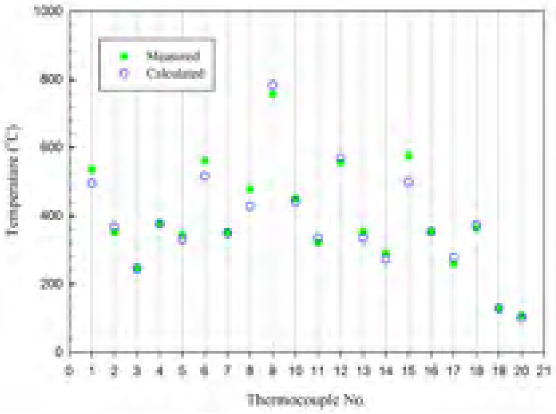

Simulation #9

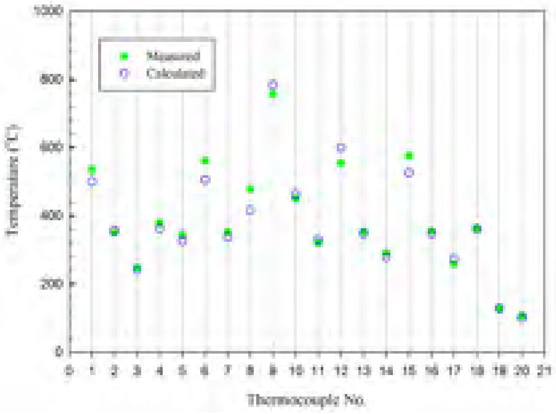

Simulation #10

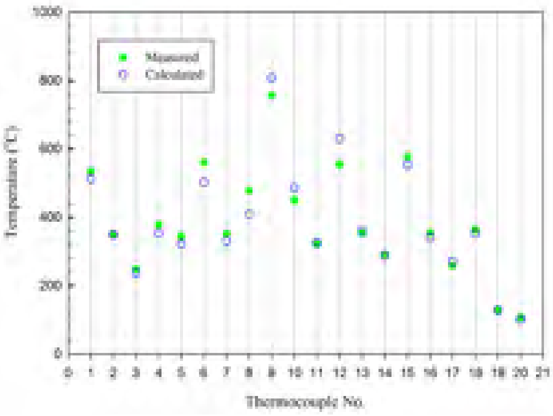

Simulation #11

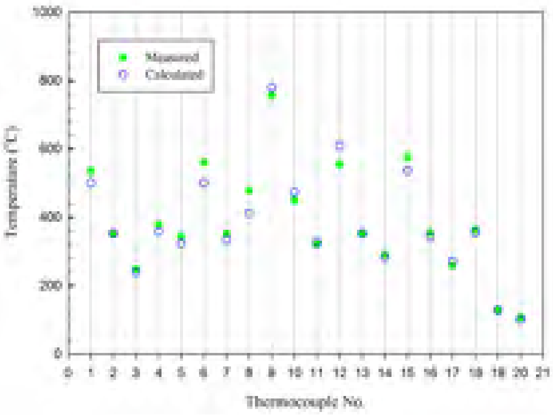

Simulation #12

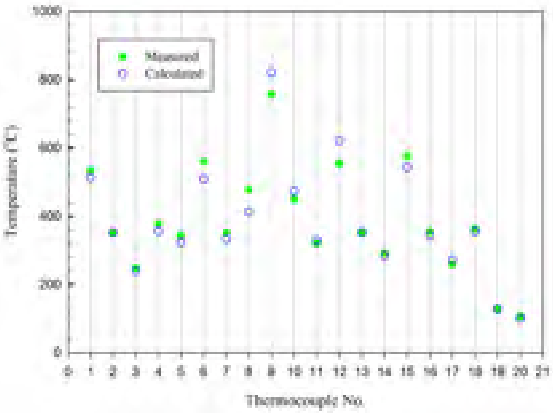

Simulation #13

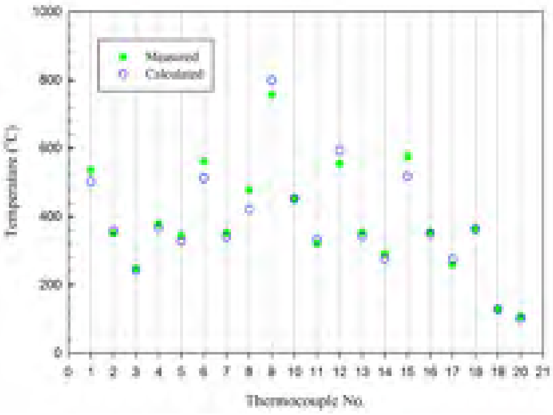

Simulation #14

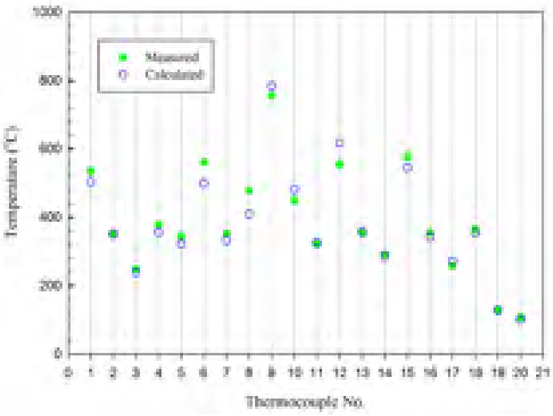

Simulation #15

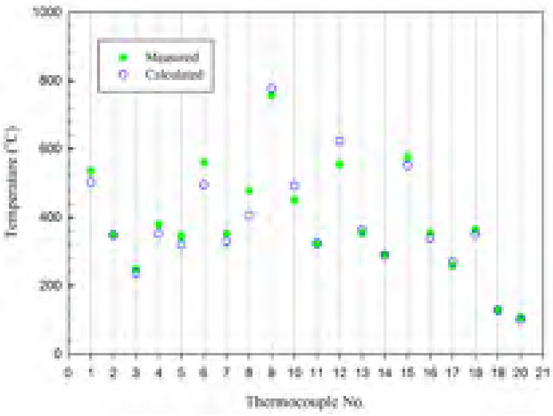

Simulation #16

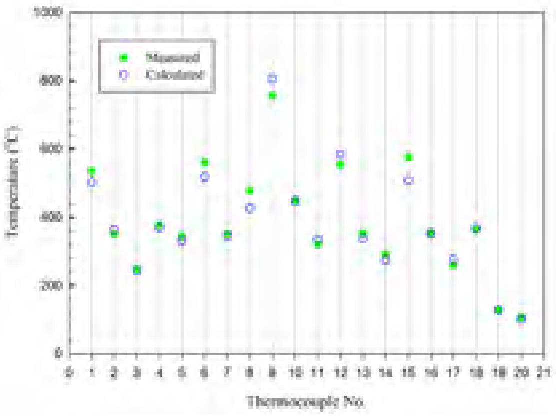

Simulation #17

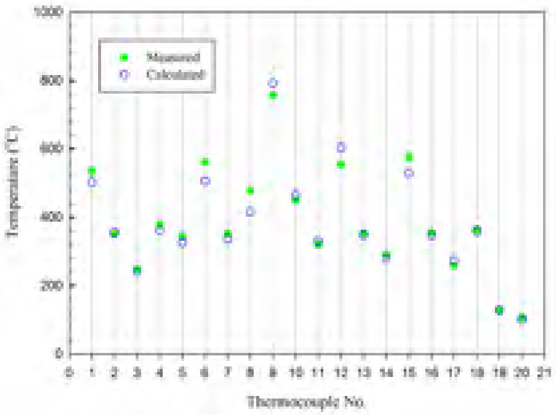

Simulation #18

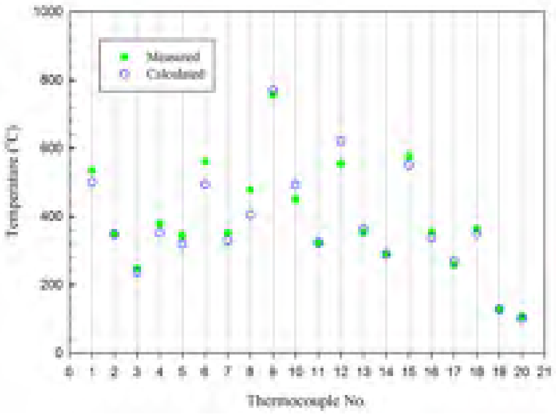

Simulation #19

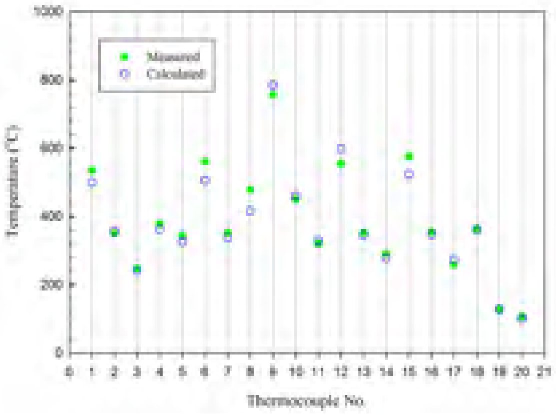

Simulation #20

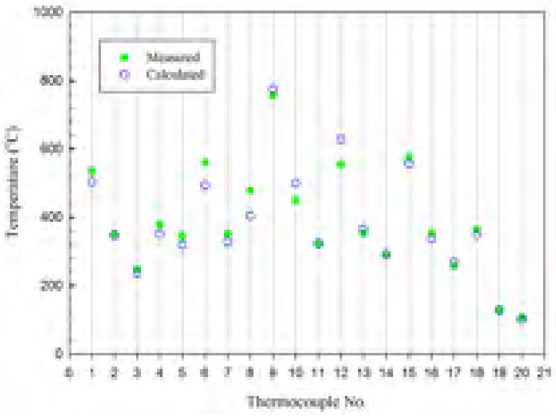

Simulation #21

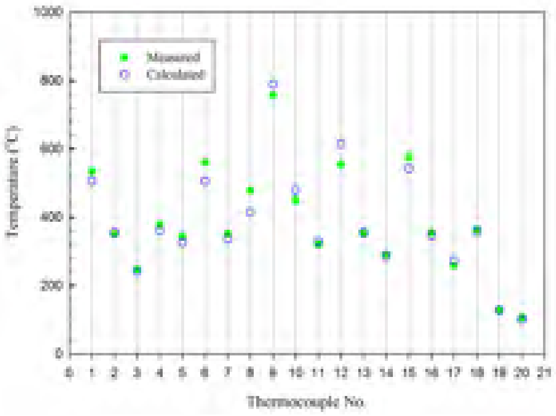

Simulation #22

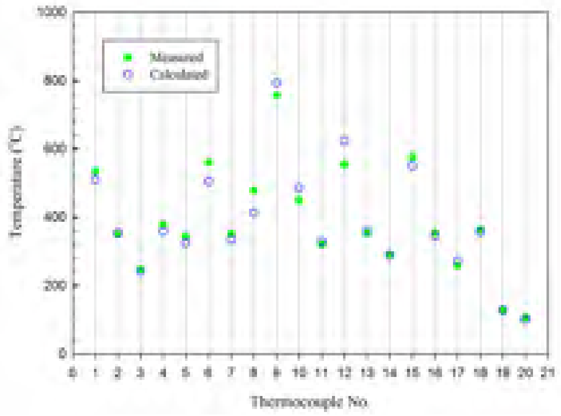

Simulation #23

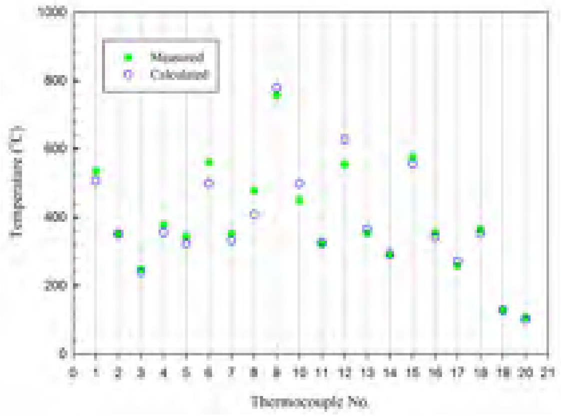

Simulation #24

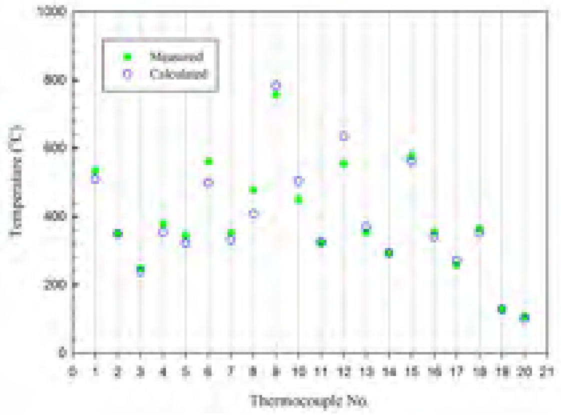

Simulation #25

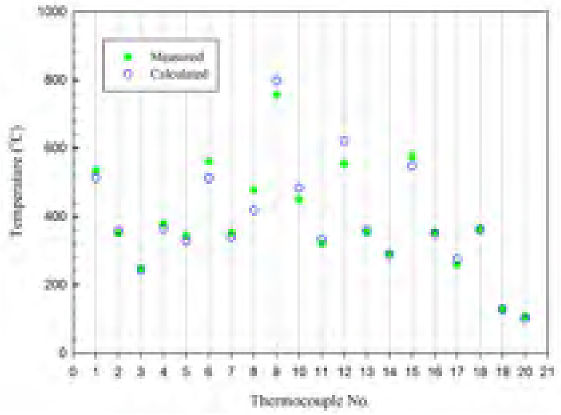

Simulation #26

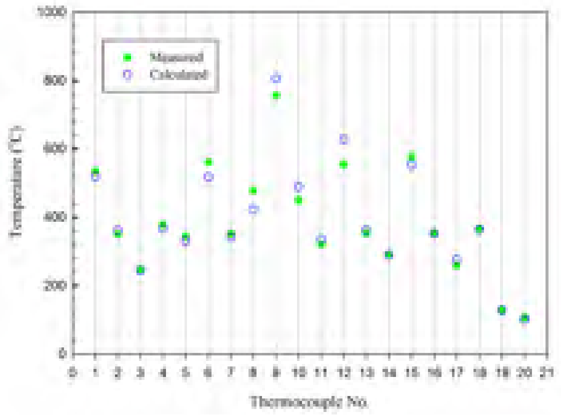

Simulation #27

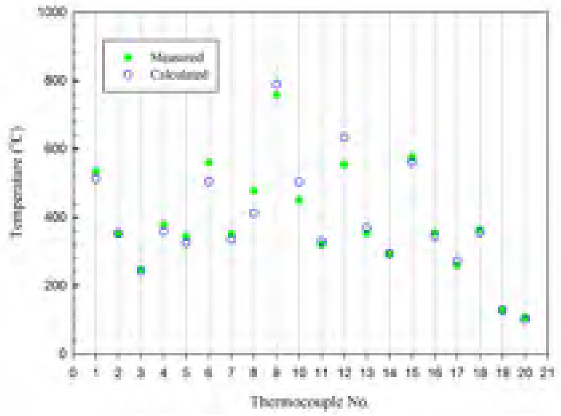

Simulation #28

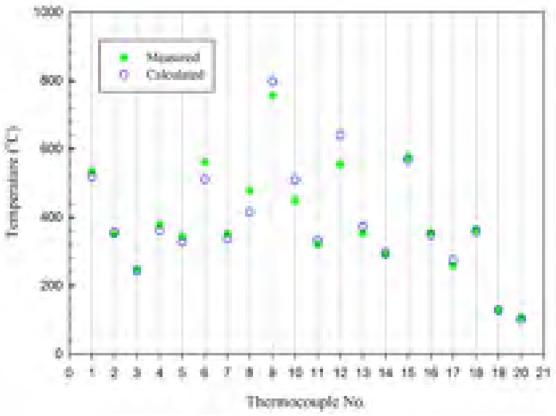

Simulation #29

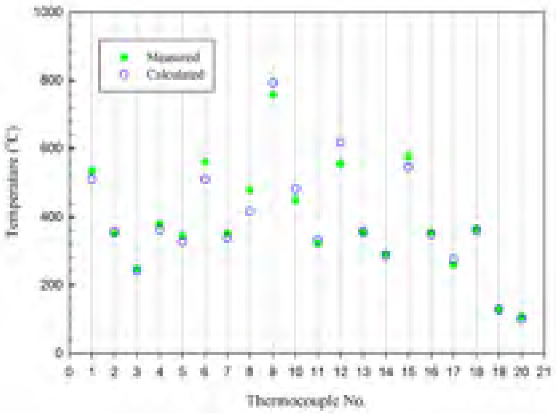

Simulation #30

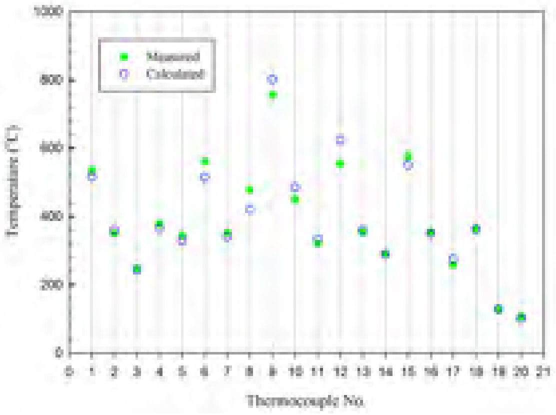

Simulation #31

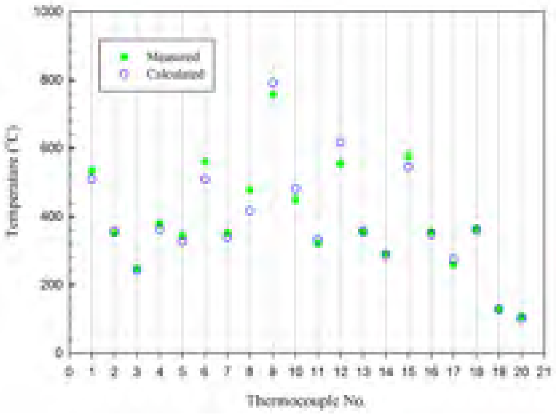

Simulation #32

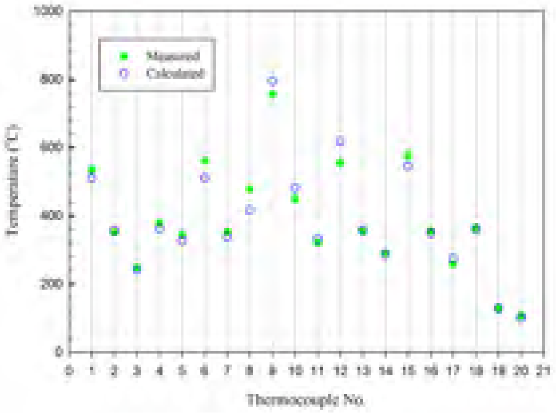

Simulation #33

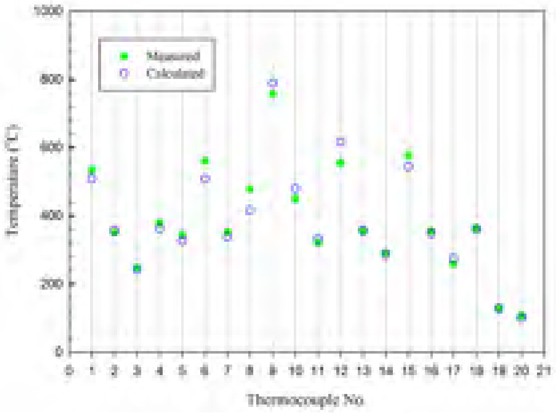

Simulation #34

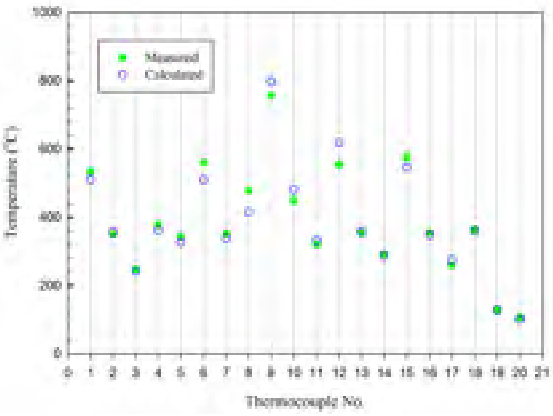

Simulation #35

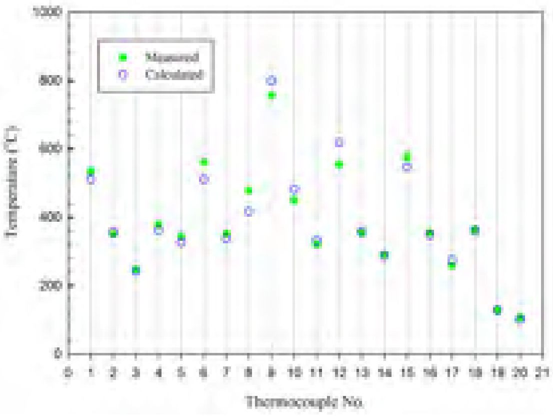

Simulation #36

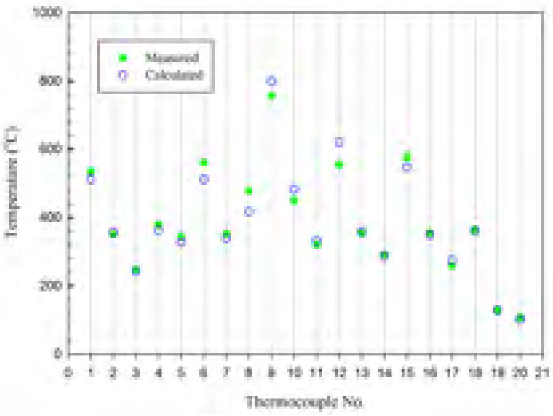

Simulation #37

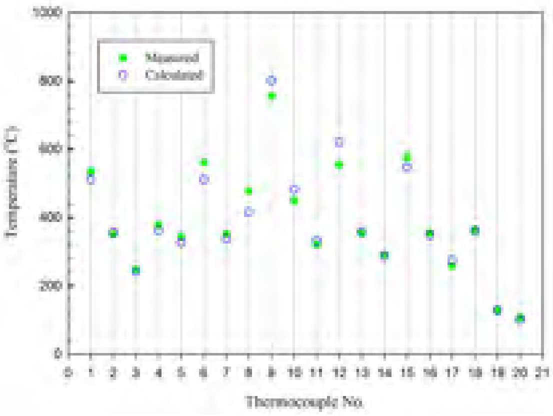

Simulation #38

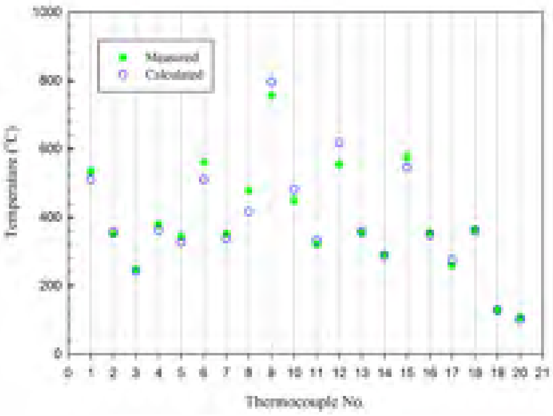

Simulation #39

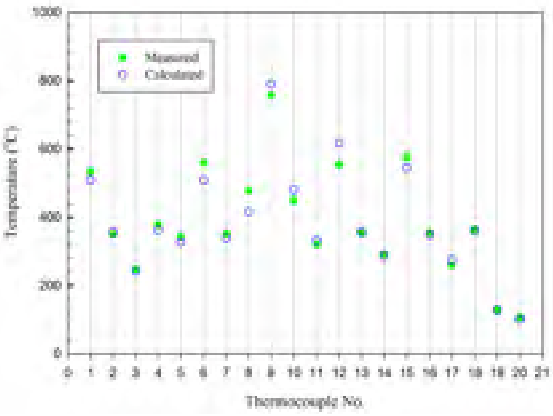

Simulation #40

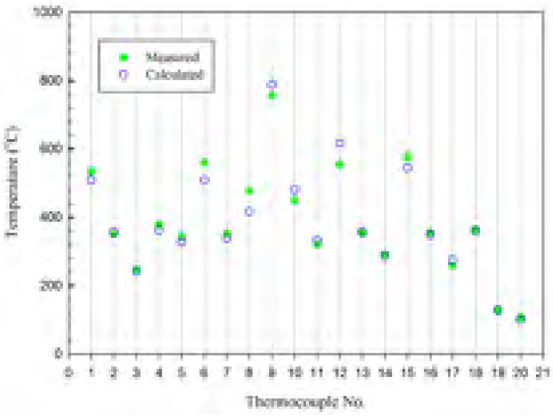

Simulation #41

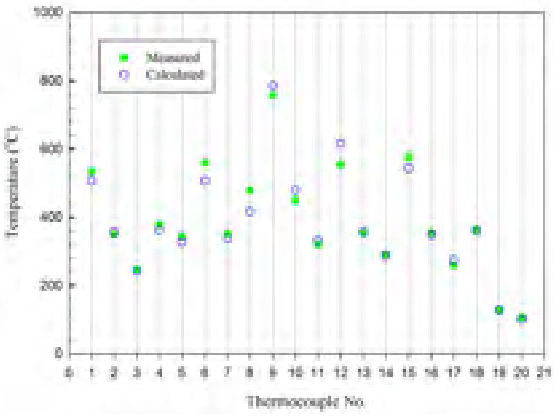

Simulation #42

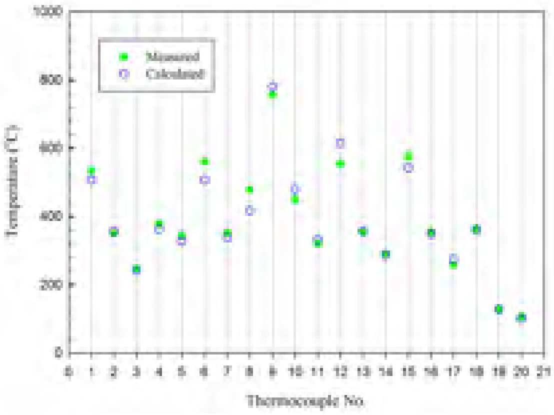

Simulation #43

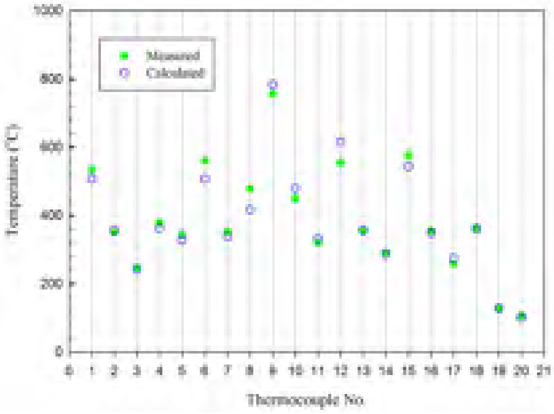

Simulation #44

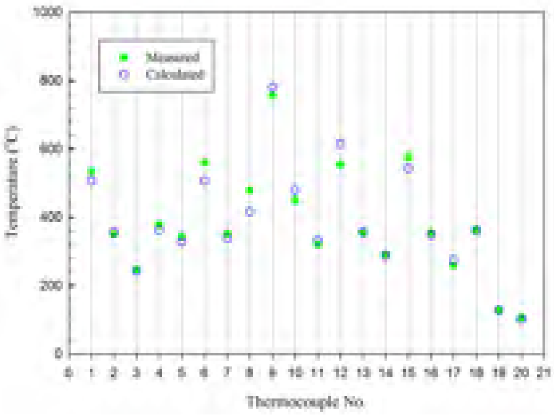

Simulation #45

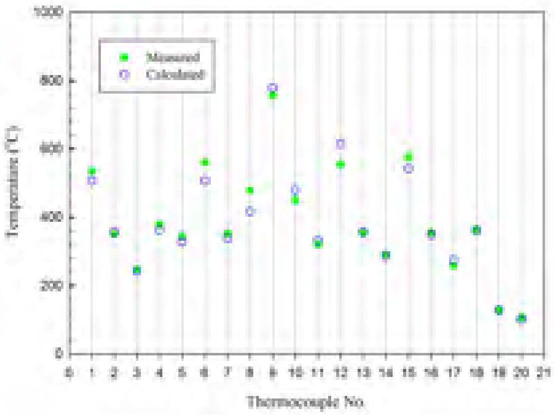

Simulation #46

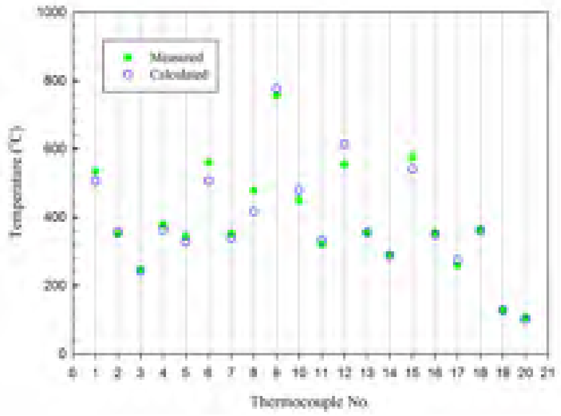

Simulation #47

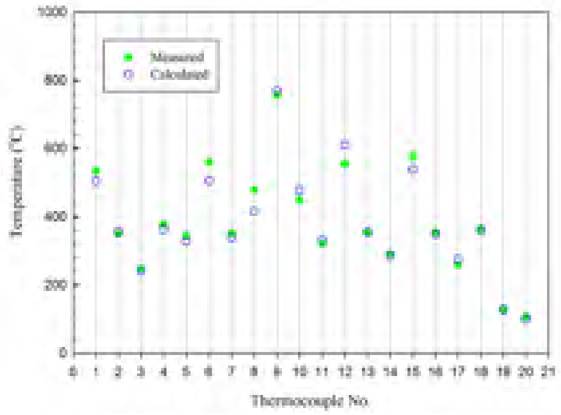

Simulation #48

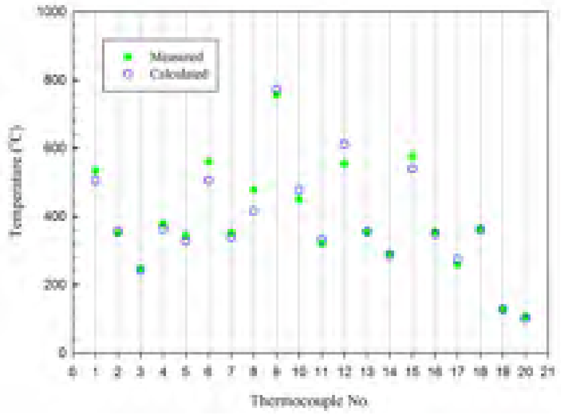

Simulation #49

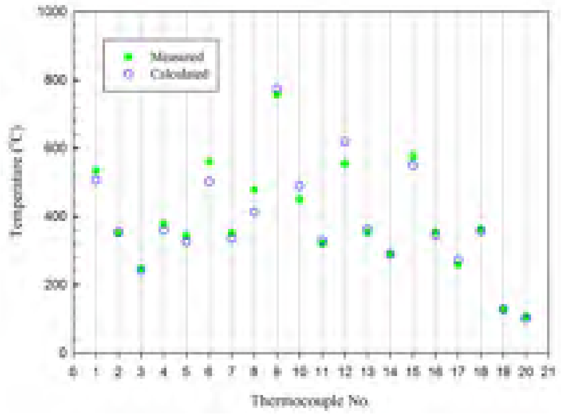

Simulation #50

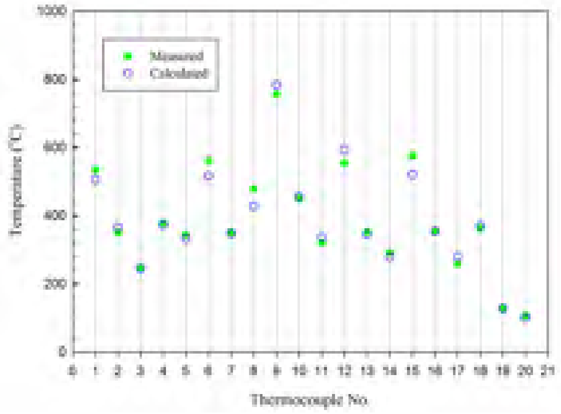

Simulation #51

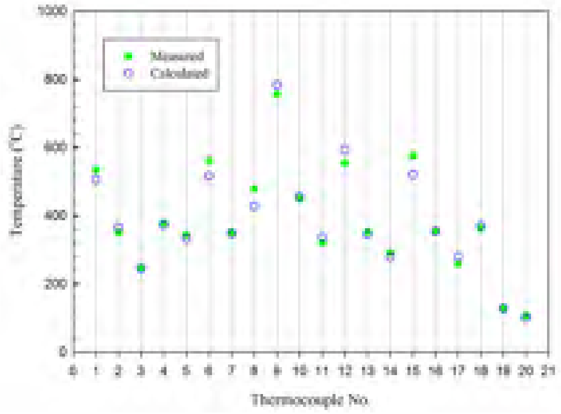

Simulation #52

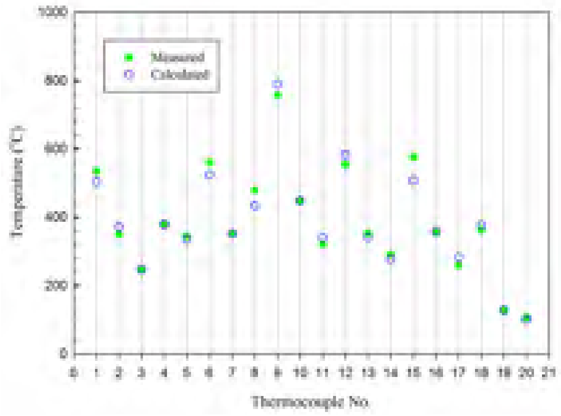

Simulation #53

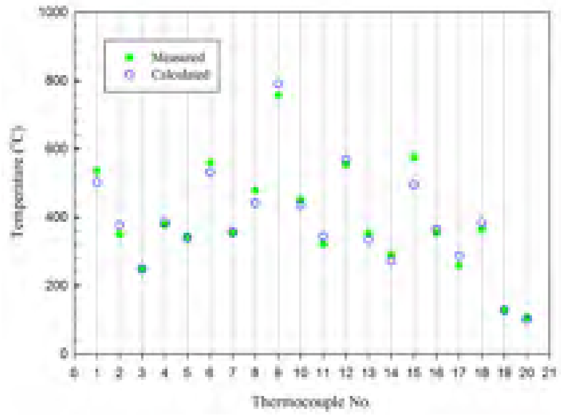

Simulation #54

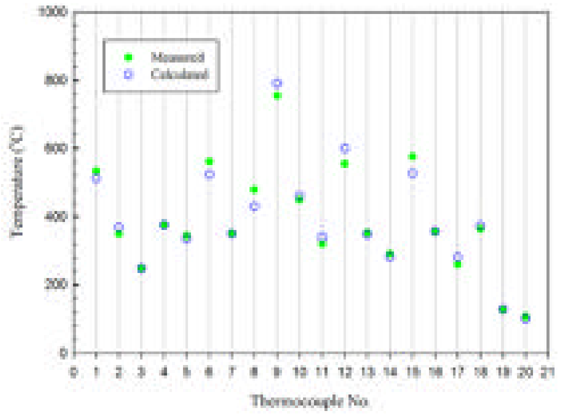

Simulation #55

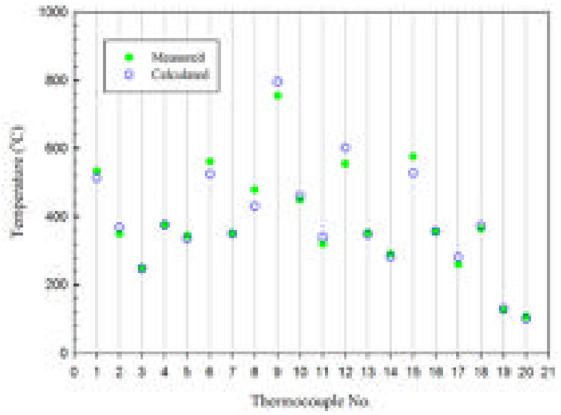

Simulation #56

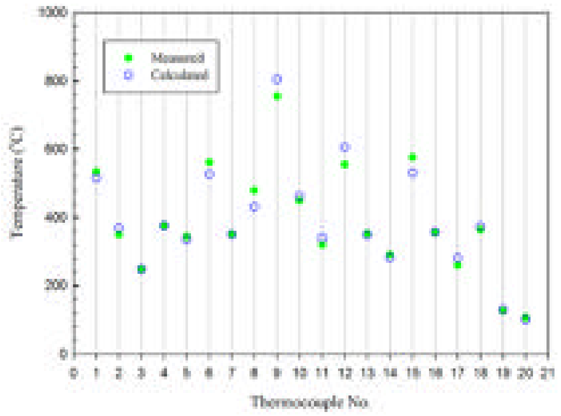

Simulation #56

APPENDIX III

MEASURED AND CALCULATED THERMAL PROFILES OF THERMOCOUPLES

Thermal profiles of thermocouples are presented in appendix III during multi-pass welding.

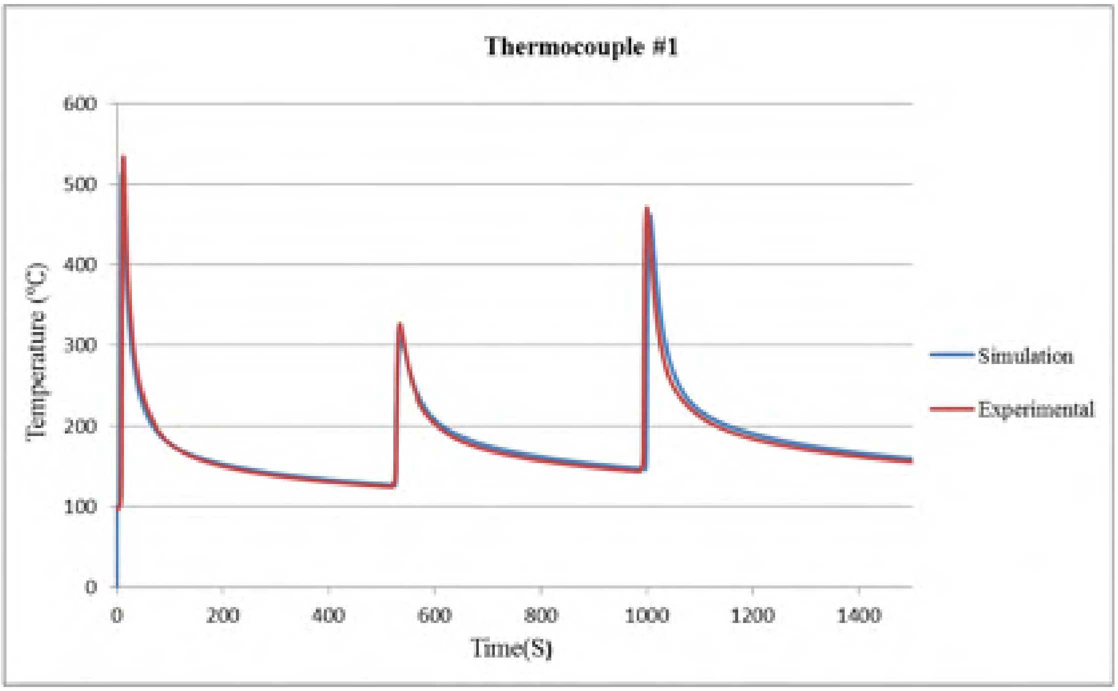

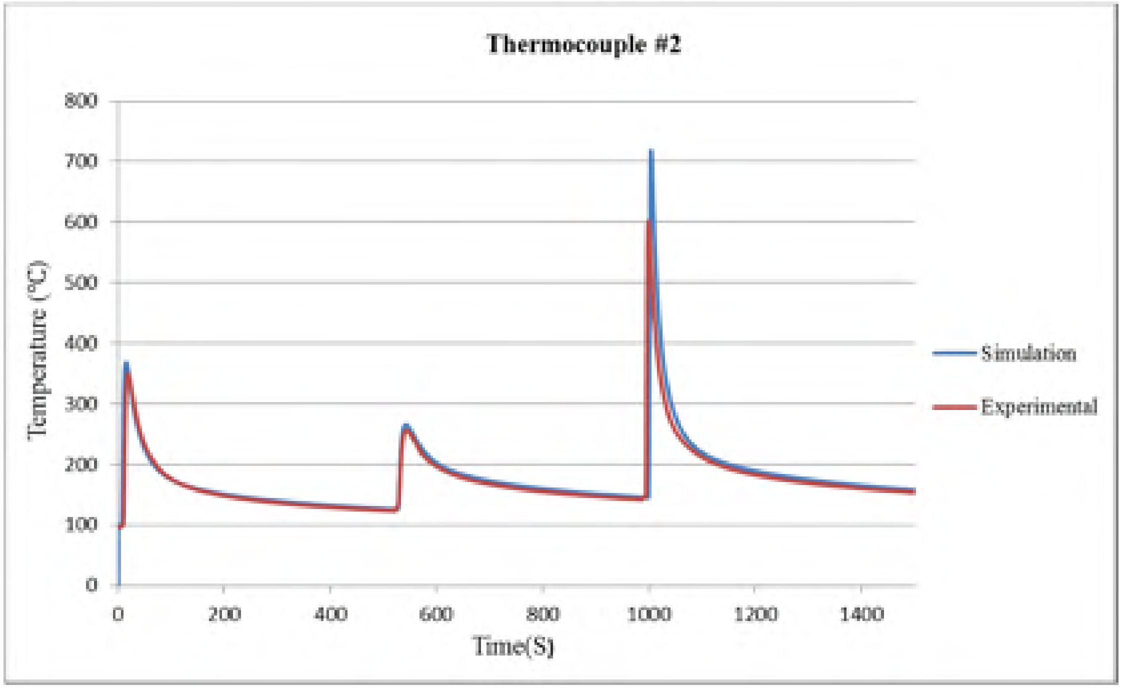

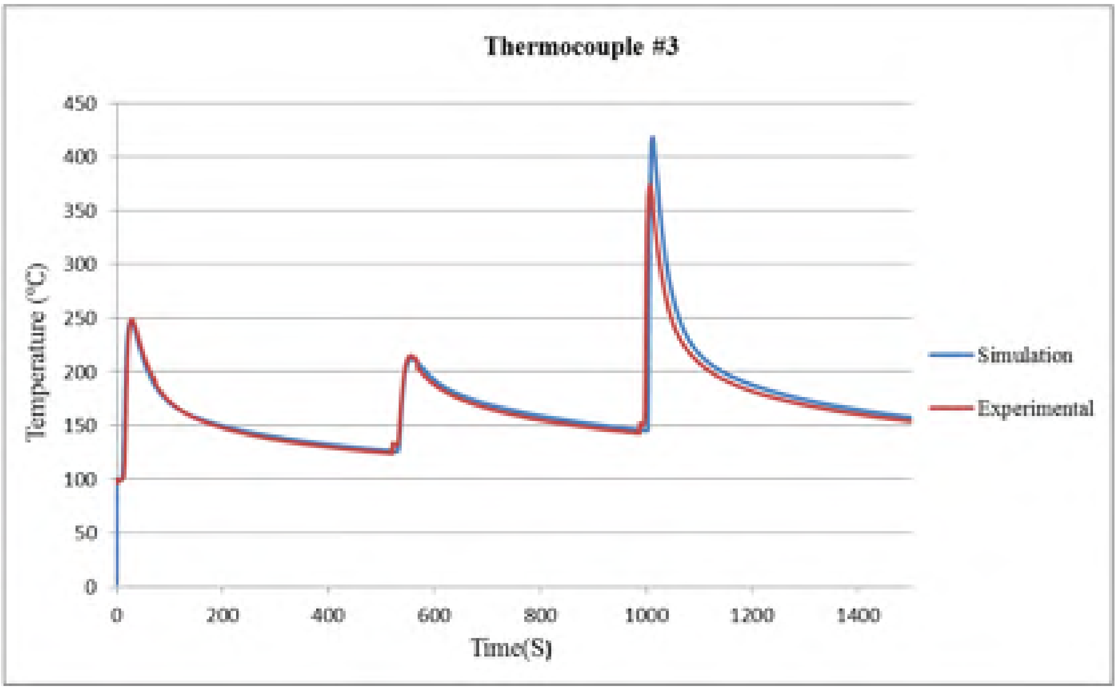
Thermocouple #3
Temperature (°C)
450
400
350
300
250
200
150
100
50
0
0
200
400
600
800
1000
1200
1400
Time(S)
Simulation
Experimental

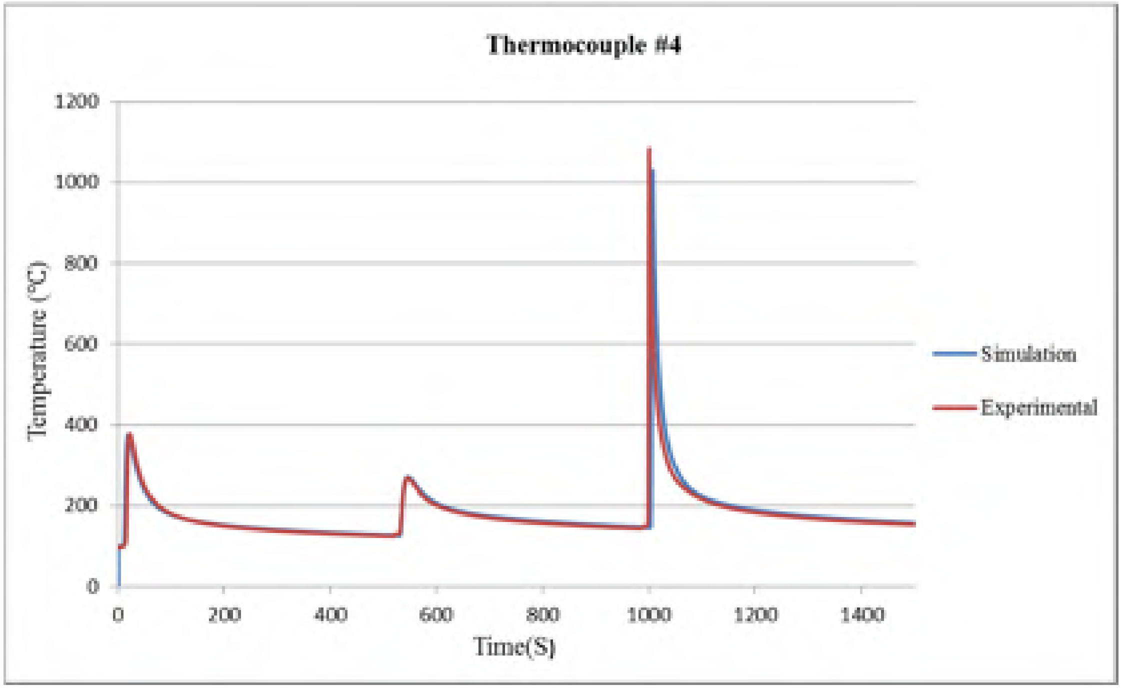
Thermocouple #4
Temperature (°C)
1200
1000
800
600
400
200
0
0
200
400
600
800
1000
1200
1400
Time(S)
Simulation
Experimental

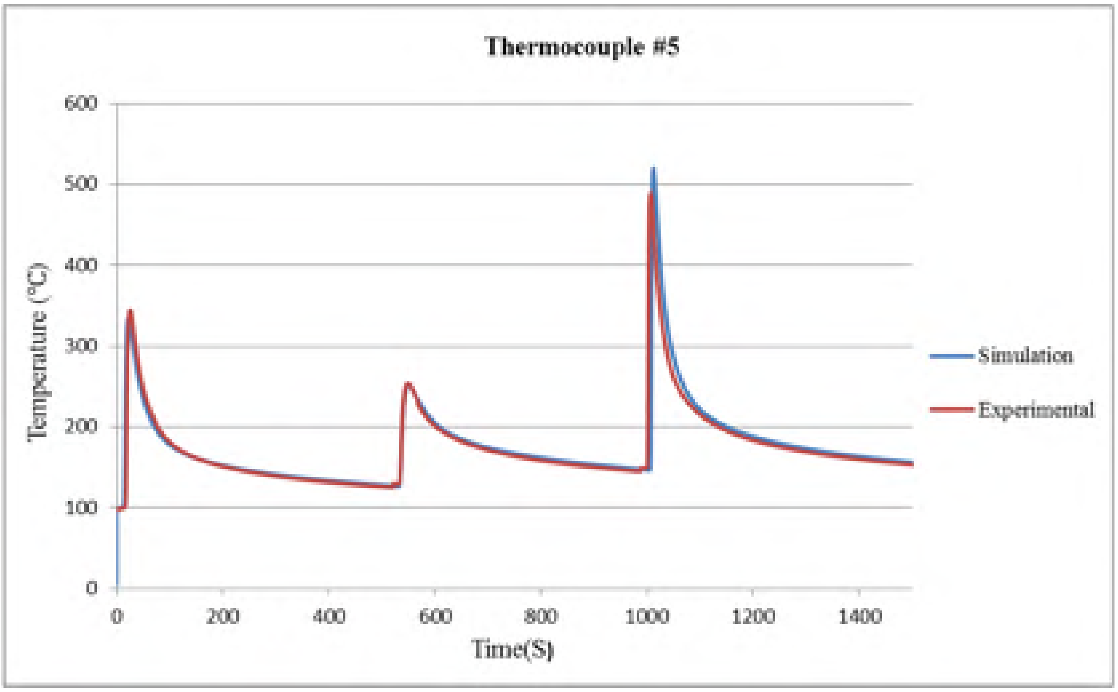
Thermocouple #5
Temperature (°C)
600
500
400
300
200
100
0
0
200
400
600
800
1000
1200
1400
Time(S)
Simulation
Experimental

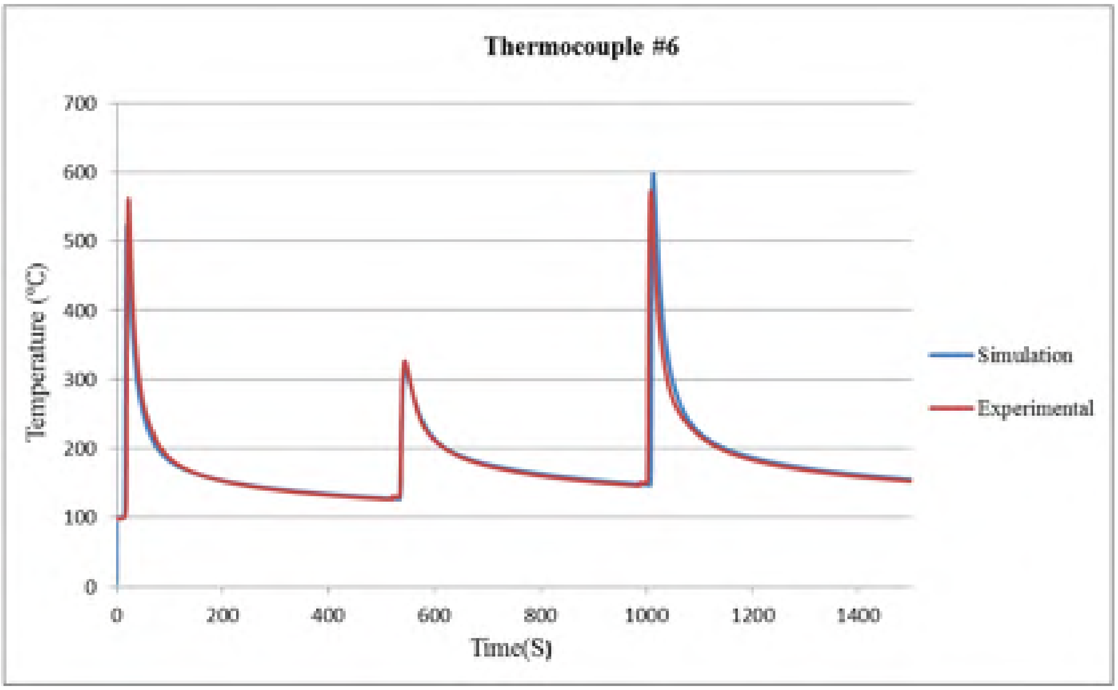
Thermocouple #6
Temperature (°C)
700
600
500
400
300
200
100
0
0
200
400
600
800
1000
1200
1400
Time(S)
Simulation
Experimental

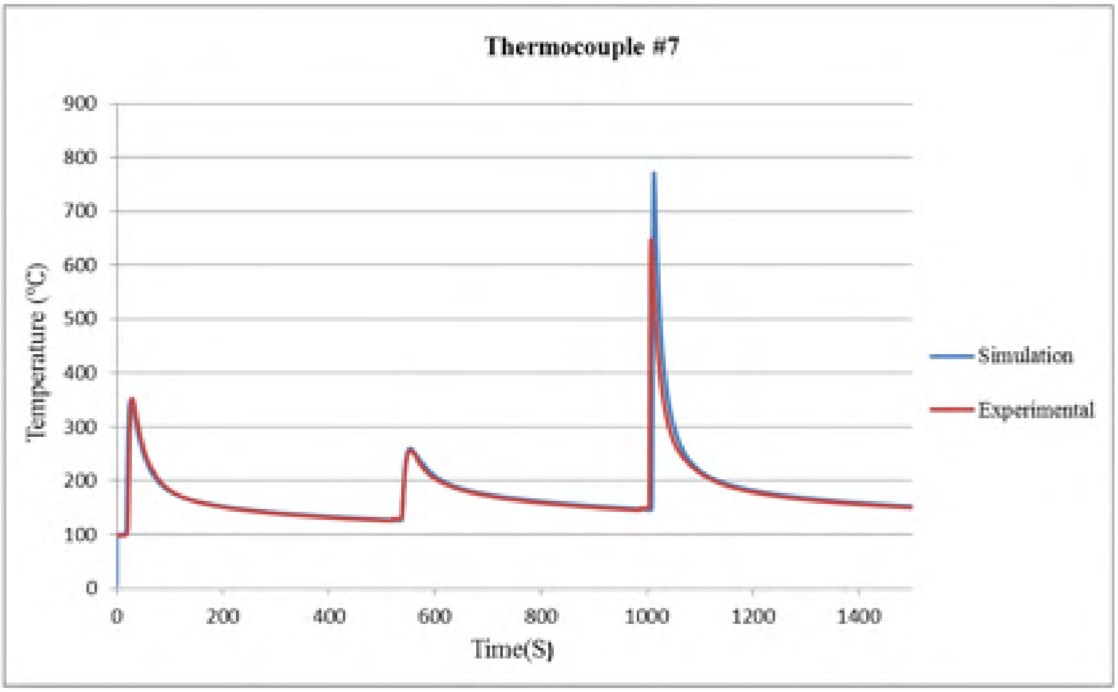
Thermocouple #7
900
800
700
600
500
400
300
200
100
0
Temperature (°C)
0
200
400
600
800
1000
1200
1400
Time(S)
Simulation
Experimental

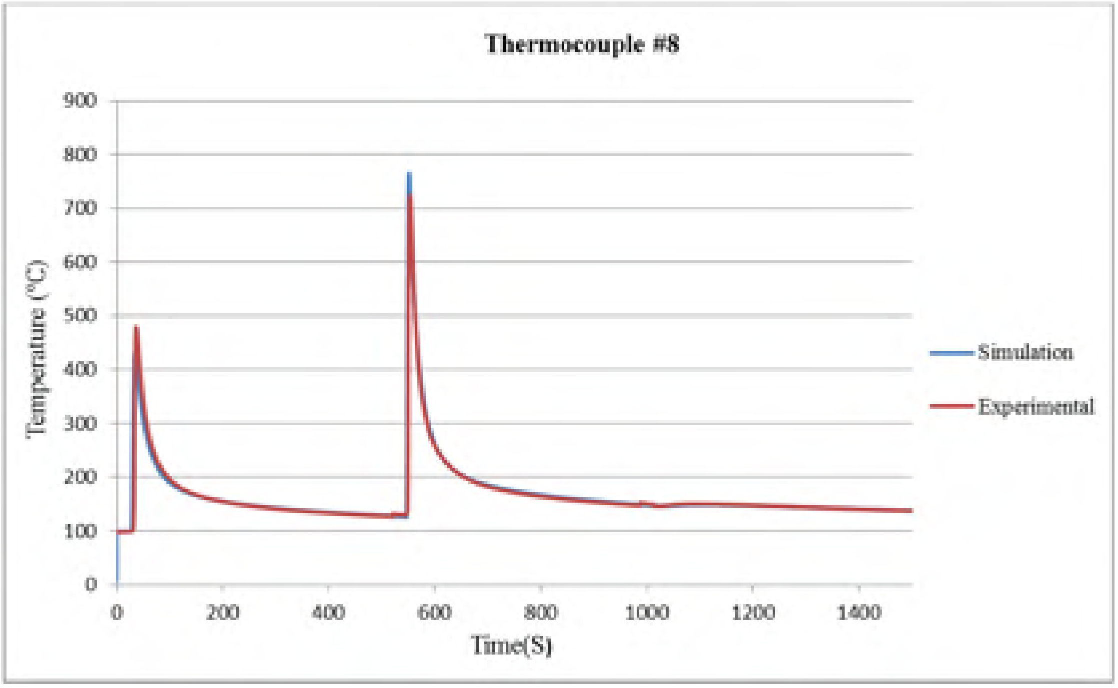
Thermocouple #8
900
800
700
600
500
400
300
200
100
0
Temperature (°C)
0
200
400
600
800
1000
1200
1400
Time(S)
Simulation
Experimental

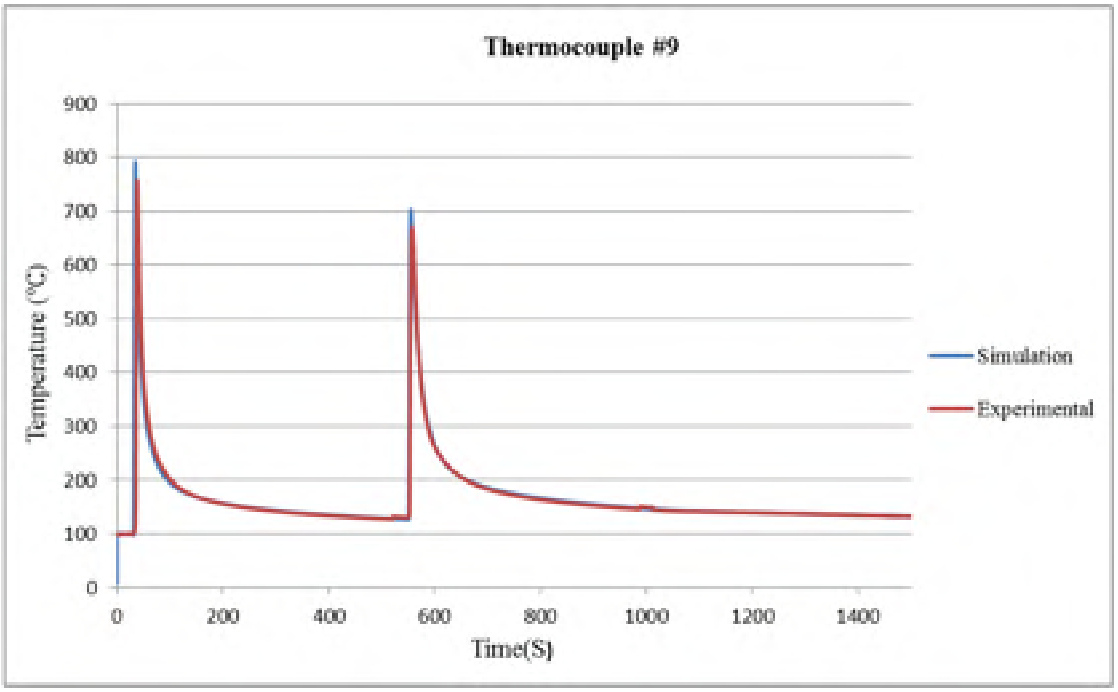
Thermocouple #9
Temperature (°C)
0
100
200
300
400
500
600
700
800
900
0
200
400
600
800
1000
1200
1400
Time(S)
Simulation
Experimental

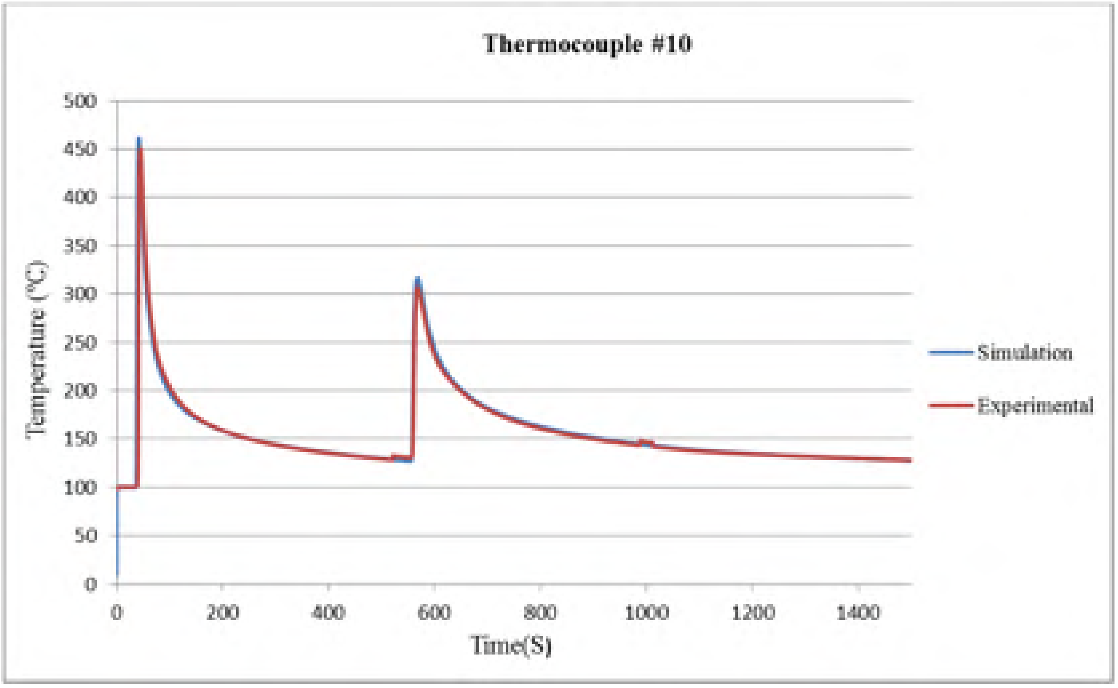
Thermocouple #10
Temperature (°C)
0
50
100
150
200
250
300
350
400
450
500
0
200
400
600
800
1000
1200
1400
Time(S)
Simulation
Experimental

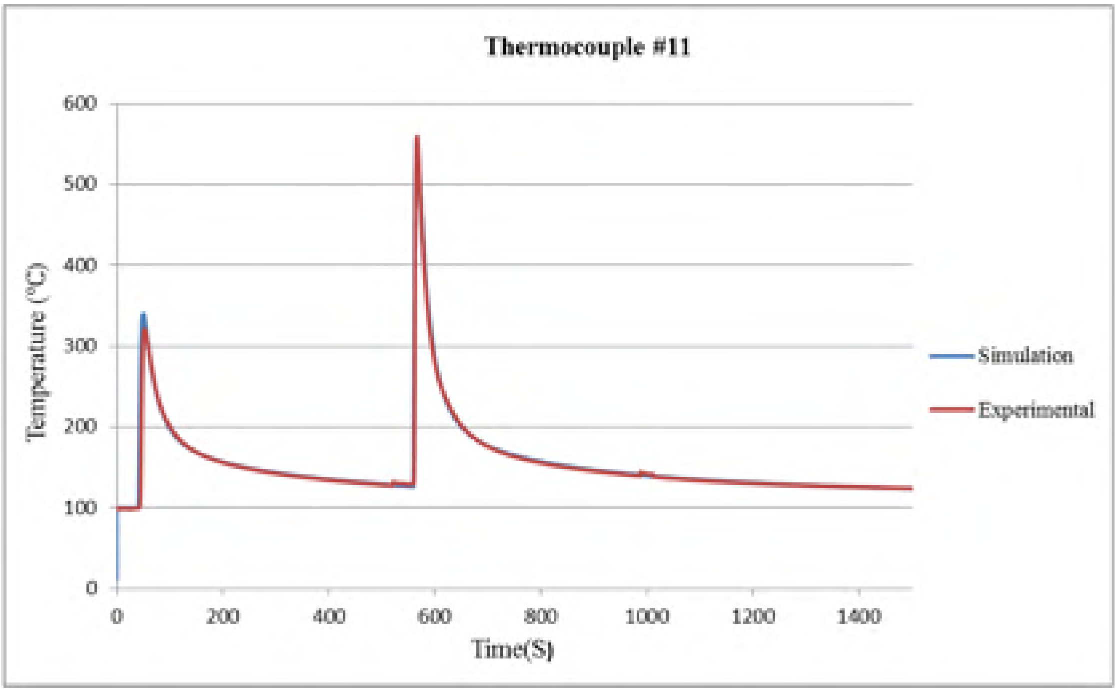
Thermocouple #11
Temperature (°C)
600
500
400
300
200
100
0
0
200
400
600
800
1000
1200
1400
Time(S)
Simulation
Experimental

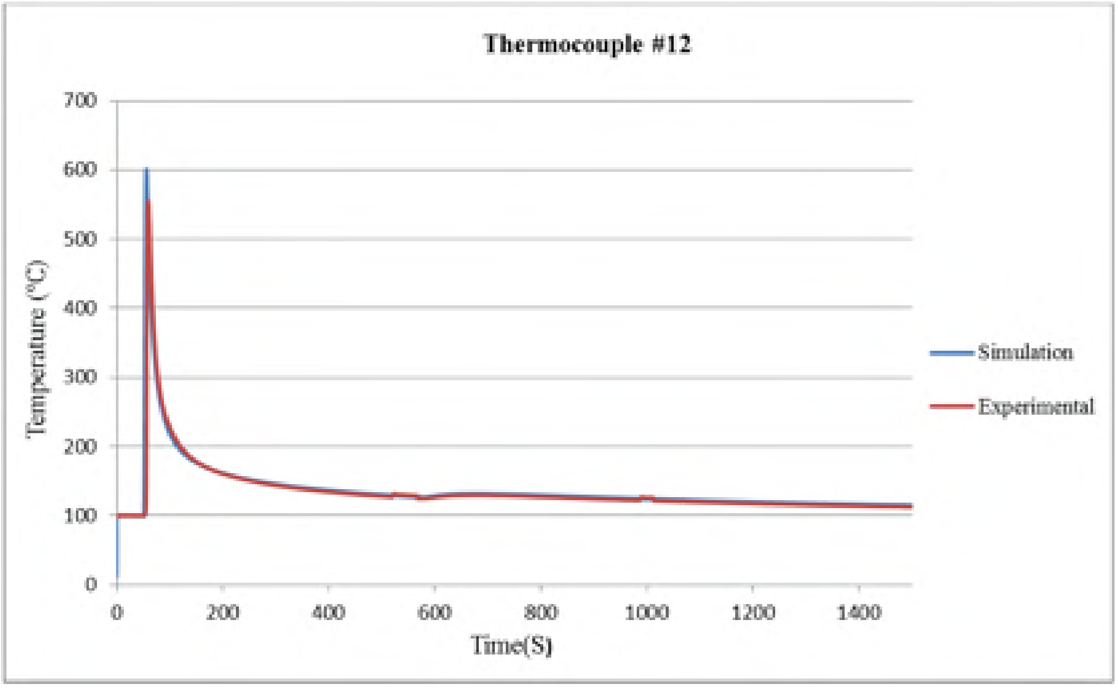
Thermocouple #12
Temperature (°C)
700
600
500
400
300
200
100
0
0
200
400
600
800
1000
1200
1400
Time(S)
Simulation
Experimental

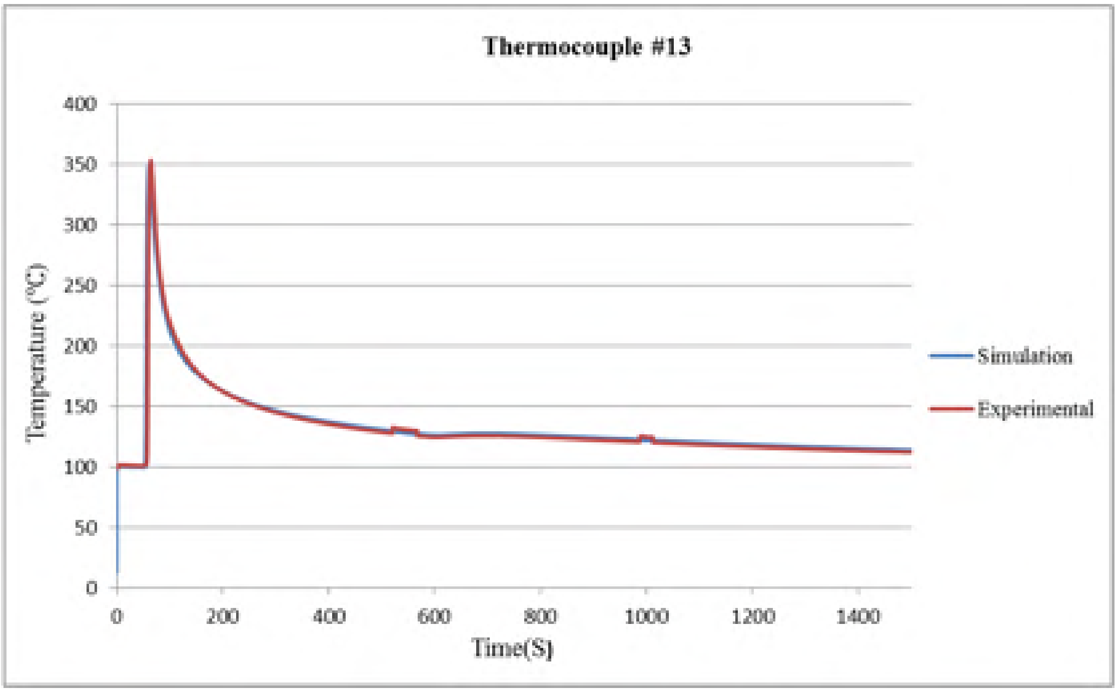
Thermocouple #13
400
350
300
250
200
150
100
50
0
Temperature (°C)
0
200
400
600
800
1000
1200
1400
Time(S)
Simulation
Experimental

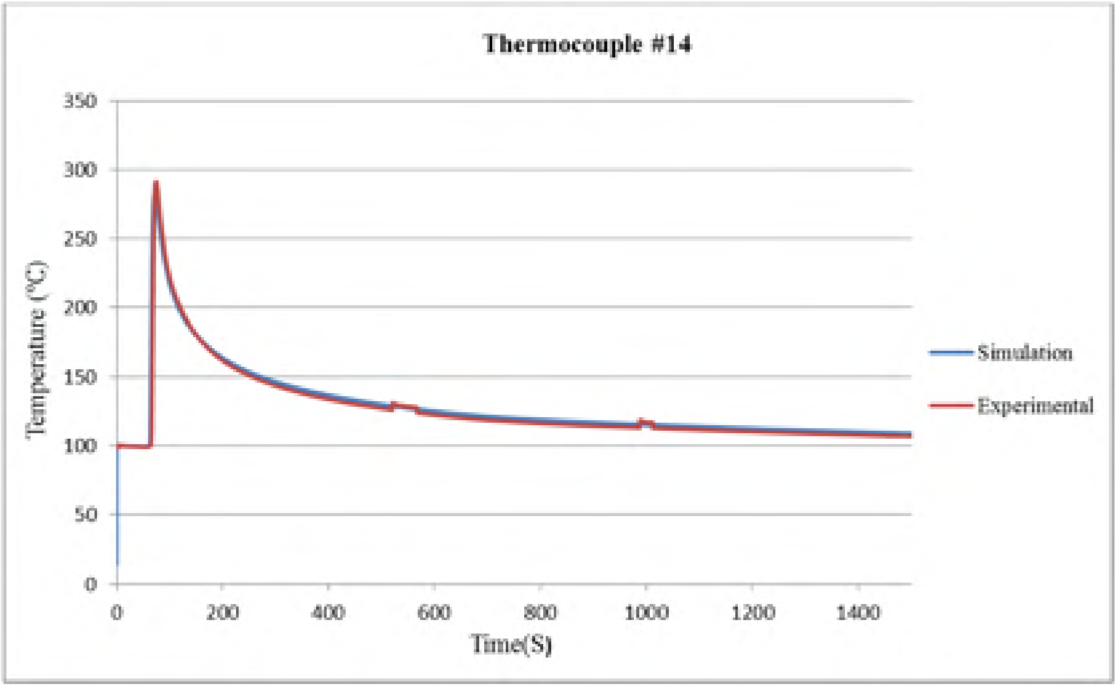
Thermocouple #14
350
300
250
200
150
100
50
0
Temperature (°C)
0
200
400
600
800
1000
1200
1400
Time(S)
Simulation
Experimental

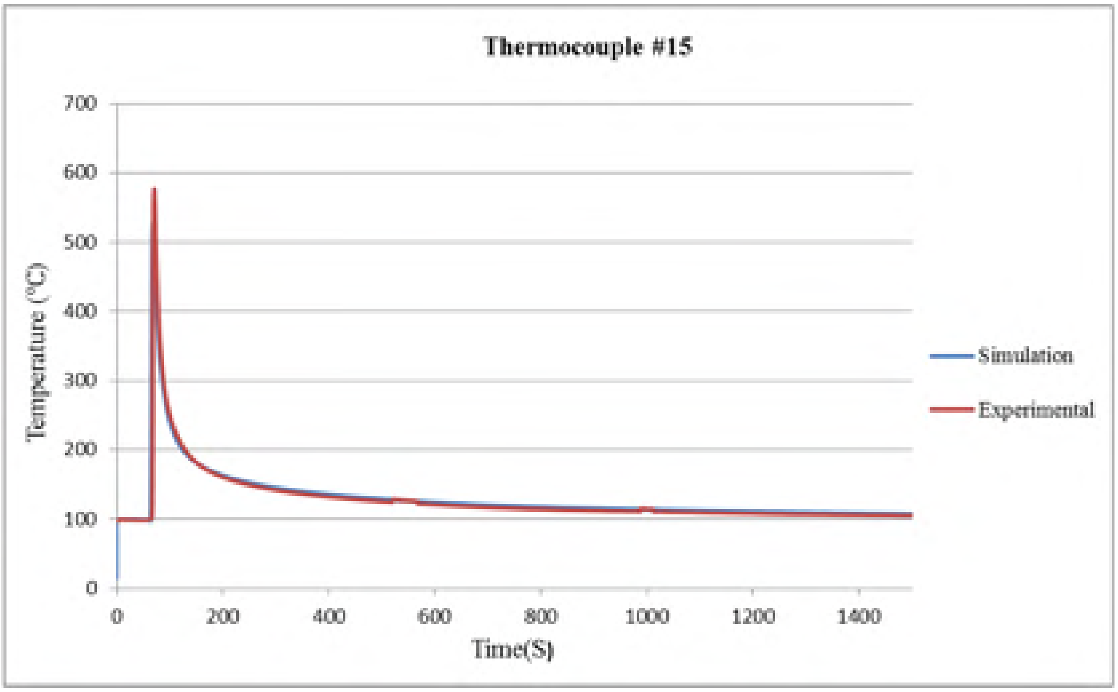
Thermocouple #15
Temperature (°C)
700
600
500
400
300
200
100
0
0
200
400
600
800
1000
1200
1400
Time(S)
Simulation
Experimental

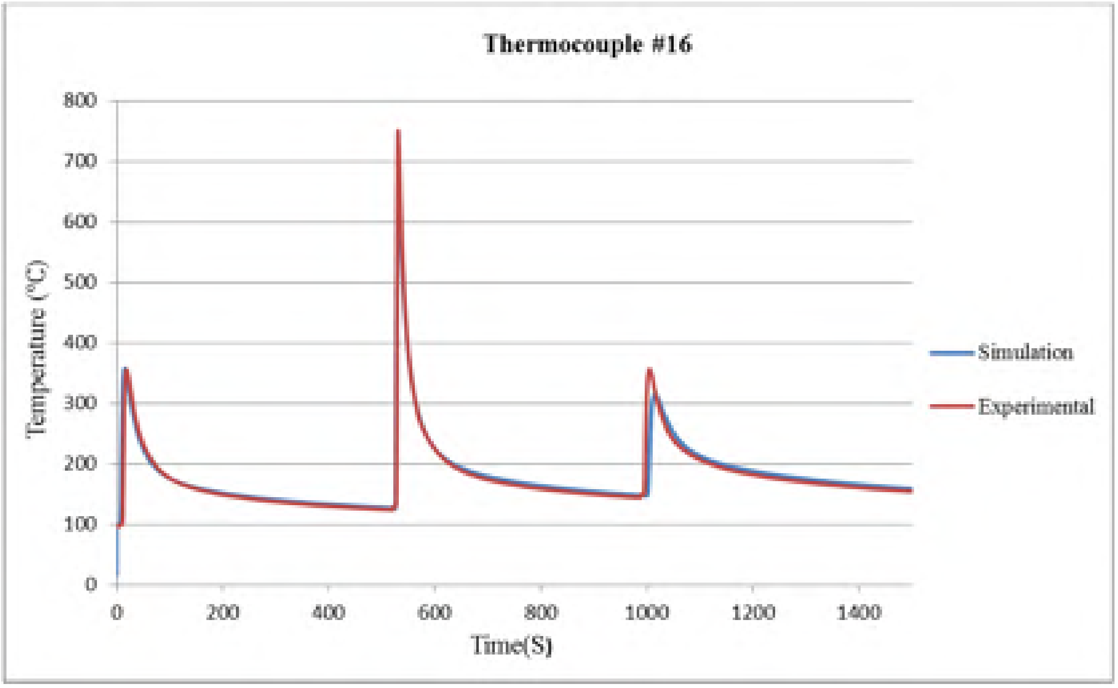
Thermocouple #16
Temperature (°C)
800
700
600
500
400
300
200
100
0
0
200
400
600
800
1000
1200
1400
Time(S)
Simulation
Experimental

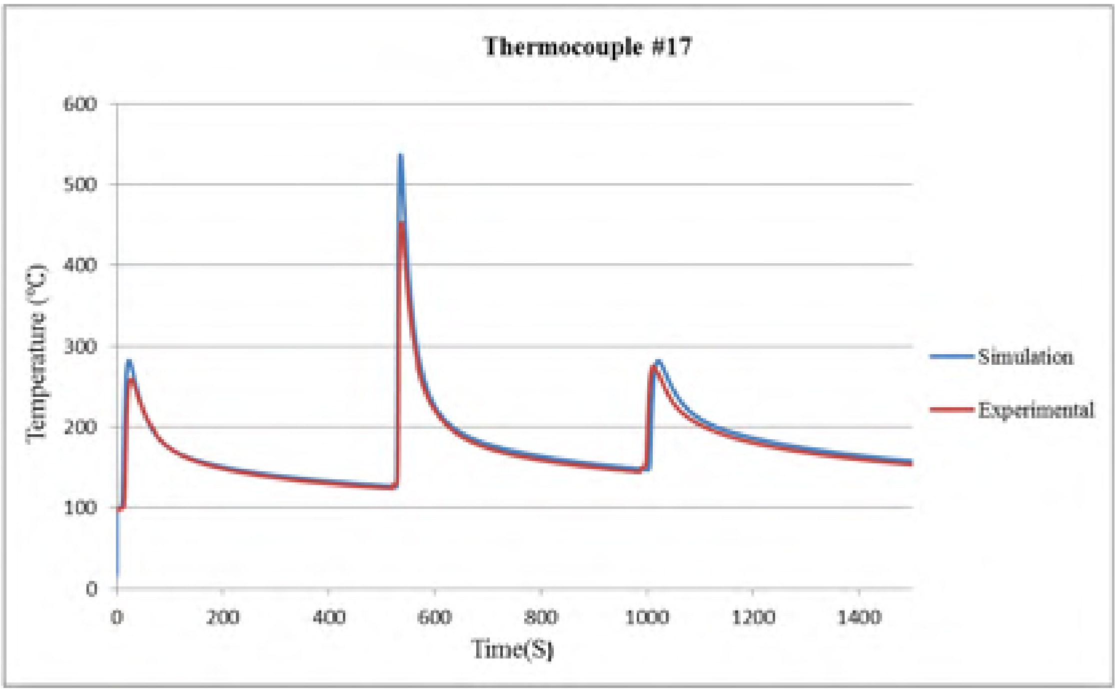

Thermocouple #17
600
500
400
300
200
100
0
Temperature (°C)
0
200
400
600
800
1000
1200
1400
Time(S)
Simulation
Experimental

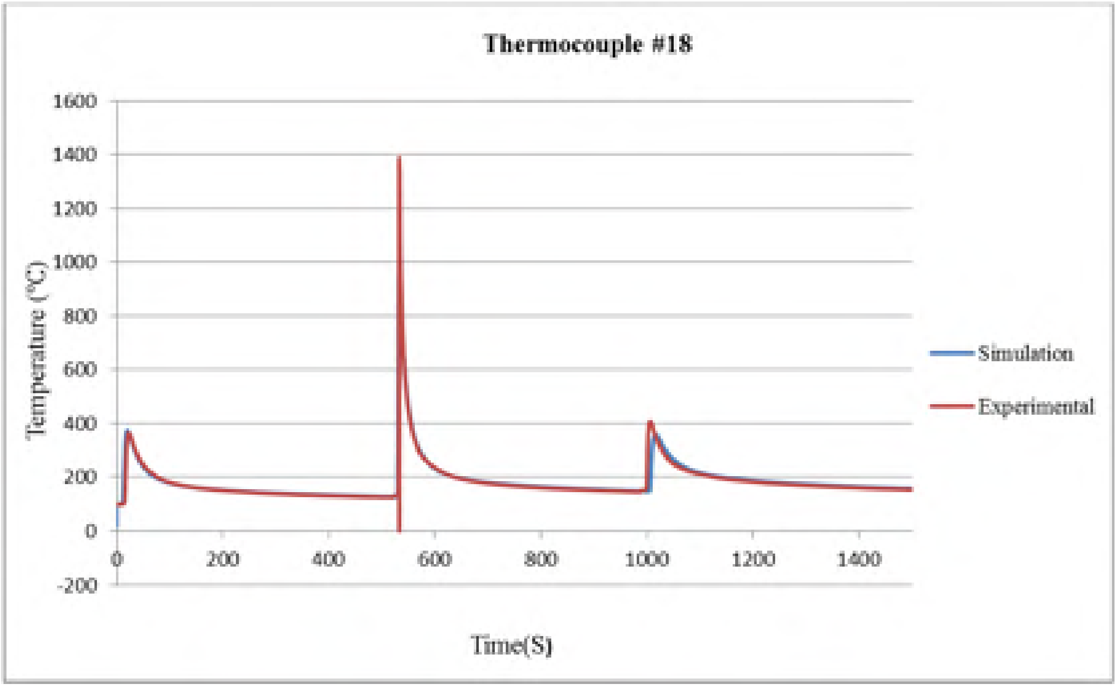

Thermocouple #18
1600
1400
1200
1000
800
600
400
200
0
-200
Temperature (°C)
0
200
400
600
800
1000
1200
1400
Time(S)
Simulation
Experimental

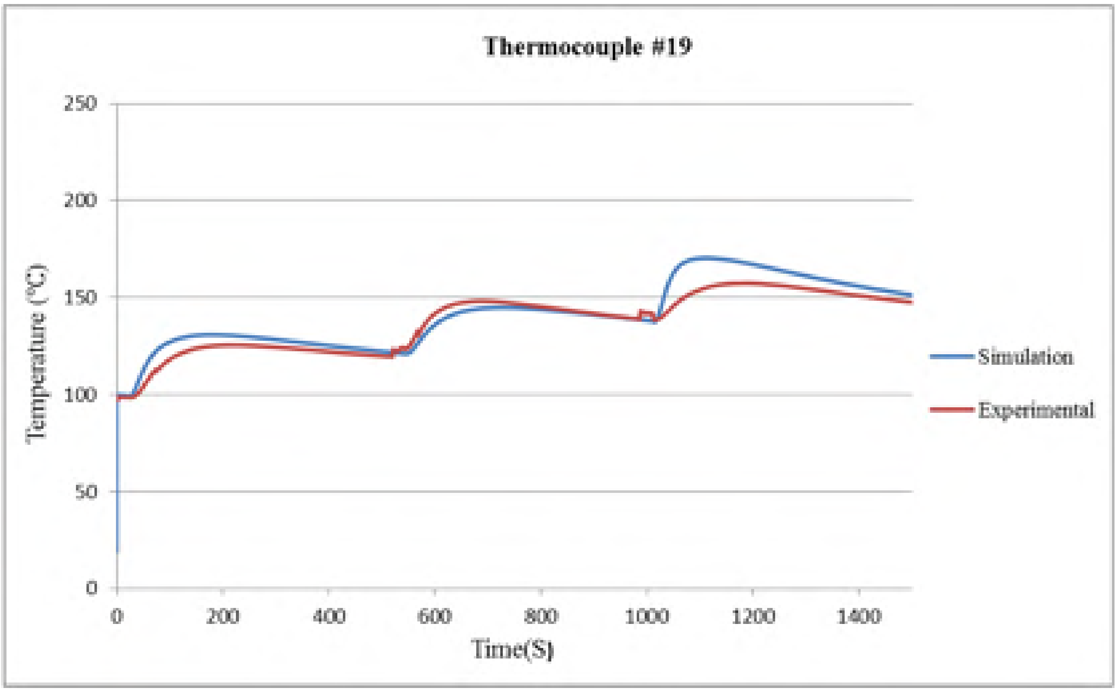
Thermocouple #19
250
200
150
100
50
0
0
200
400
600
800
1000
1200
1400
Time(S)
Temperature (°C)
Simulation
Experimental

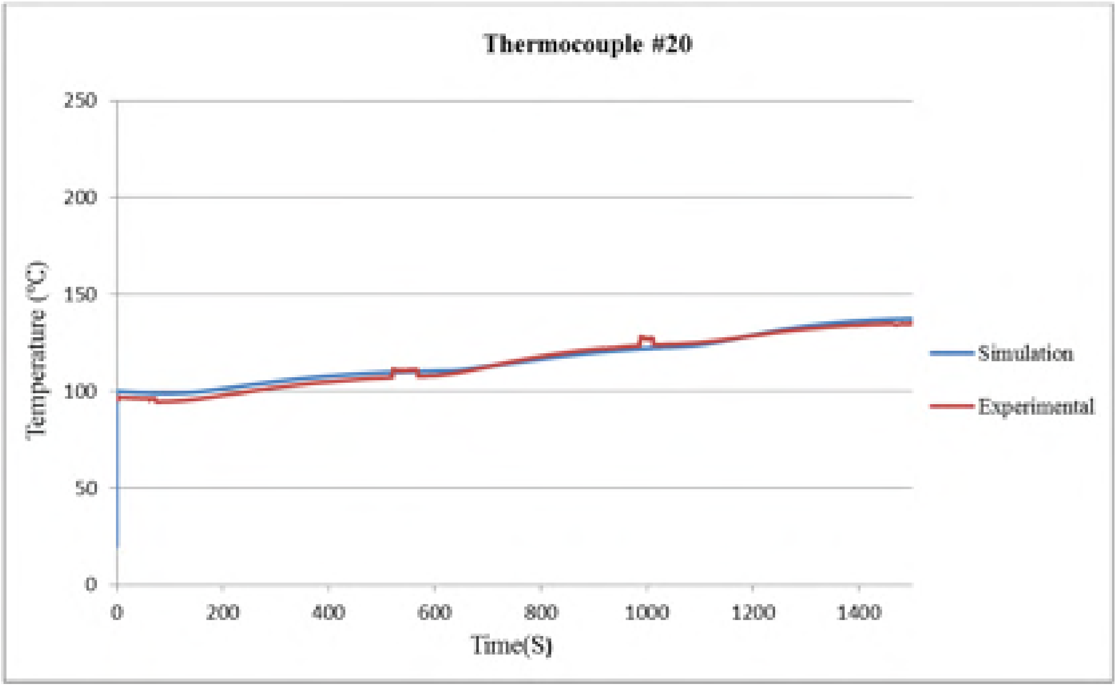
Thermocouple #20
250
200
150
100
50
0
0
200
400
600
800
1000
1200
1400
Time(S)
Temperature (°C)
Simulation
Experimental

REFERENCES

1. Krutz, G. and L. Segerlind, *Finited Element Analysis of Welded Structures*, 1976, SAE Technical Paper.

2. Jeffus, L.F., *Welding: principles and applications*. 2002: Cengage Learning.

3. Radhakrishnan, V., *Welding technology and design*. 2005: New Age International.

4. Fan, H. and R. Kovacevic, *Three-dimensional model for gas tungsten arc welding with filler metal.* Proceedings of the Institution of Mechanical Engineers, Part B: Journal of Engineering Manufacture, 2006. **220**(7): p. 1107-1115.

5. Lyttle, K.A., *Gases for Welding, Welding, Brazing, and Soldering*, 1993, ASM International: ASM Handbook. p. 64-69.

6. Goldak, J., A. Chakravarti, and M. Bibby, *A new finite element model for welding heat sources.* Metallurgical Transactions B, 1984. **15**(2): p. 299-305.

7. Wahab, M.A. and M. Painter, *Numerical models of gas metal arc welds using experimentally determined weld pool shapes as the representation of the welding heat source.* International journal of pressure vessels and piping, 1997. **73**(2): p. 153-159.

8. Zhang, Y.M., *Arc Physics of Gas Tungsten and Gas Metal Arc Welding* in *Welding Fundementals and Procsses*2011, ASM International: ASM Handbook. p. 249-259.

9. Bushey, R.A., *Welding of Cast Irons, Welding, Brazing and Soldering*, in *ASM Handbook* 1993, ASM International. p. 708-721.

10. Mohamat, S.A., et al., *The Effect of Flux Core Arc Welding (FCAW) Processes On Different Parameters.* Procedia Engineering, 2012. **41**(0): p. 1497-1501.

11. Kannan, T. and N. Murugan, *Effect of flux cored arc welding process parameters on duplex stainless steel clad quality.* Journal of Materials Processing Technology, 2006. **176**(1–3): p. 230-239.

12. Linnert, G.E., *Welding metallurgy*. Vol. 1. 1994: American Welding Society Miami (FL).

13. Zinn, W. and B. Scholtes, *Residual Sress Formation Processes Durig Welding and Joining*, G. Totten, M. Howes, and T. Inoue, Editors. 2002, ASM International: Handbook of Residual Stress and Deformation. p. 361-396.

14. Pilipenko, A., *Computer Simulation of residual stress and distortion of thick plates in multi-electrode submerged arc welding. their mitigation techniques*, in *machine design and materials technology*2001, Norweign University of Science and Technology: Tondheim, Norway. p. 222.

15. Belchuk, G.A., K.M. Gatovskii, and B.A. Kokh, *Welding of Ship Structure.* Sudostroenie, 1980.

16. Totten, G.E., *Handbook of residual stress and deformation of steel*. 2002: ASM international.

17. Bilmes, P., M. Solari, and C. Llorente, *Characteristics and effects of austenite resulting from tempering of 13Cr–NiMo martensitic steel weld metals.* Materials Characterization, 2001. **46**(4): p. 285-296.

18. Côté, M., *Étude des cinétiques de transformation de phase d'un acier inoxydable martensitique 13% Cr-4% Ni*, 2007, École de technologie supérieure.

19. Porter, D.A. and K.E. Easterling, *Phase Transformations in Metals and Alloys, (Revised Reprint)*. 1992: CRC press.

20. Bhadeshia, H., *Material factors.* ASM International, Materials Park, OH 44073-0002, USA, 2002., 2002: p. 3-10.

21. Moein, H. and I. Sattari-Far, *Different finite element techniques to predict welding residual stresses in aluminum alloy plates.* Journal of Mechanical Science and Technology, 2014. **28**(2): p. 679-689.

22. Fanous, I.F., M.Y. Younan, and A.S. Wifi, *3-D finite element modeling of the welding process using element birth and element movement techniques.* Journal of pressure vessel technology, 2003. **125**(2): p. 144-150.

23. Hong, J., C. Tsai, and P. Dong, *Assessment of numerical procedures for residual stress analysis of multipass welds.* Welding Journal-New York-, 1998. **77**: p. 372-s.

24. Bae, D.H., et al., *Numerical analysis of welding residual stress using heat source models for the multi-pass weldment.* KSME international journal, 2002. **16**(9): p. 1054-1064.

25. lee, S.G., *Modelin of Residual Stress In Thick Section Weldment* 1992, The Ohio State University.

26. Atkins, G., et al., *Welding process effects in weldability testing of steels.* Welding journal, 2002. **81**(4): p. 61s-68s.

27. Bouffard, D.-A., *Simulation par éléments finis des contraintes résiduelles de soudage en fonction des paramètres de soudage robotisé*, *Département de génie mécanique*2007, École polytechnique de Montréal.

28. Moore, J., et al. *A comparison of the point source and finite element schemes for computing weld cooling*. in *Welding Research: The State of the Art, Proc. of 1985 Int. Welding Congress in junction with ASM Materials Week'85*. 1985.

29. Bouffard, D.-A. and J. Lanteigne, *Détermination de l'historique thermique du passage d'un arc de soudage par la méthode des éléments finis*, in *Diffusion Hydro-Québec*2004: IREQ-2004-158.

30. Morin, O., *Calcul des contraintes résiduelles dues au soudage par la méthode des éléments finis*, 2006, École de technologie supérieure.

31. Chen, B.-Q., *Prediction of Heating Induced Temperature Fields and Distortions in Steel Plates*, 2011, Dissertation to obtain the degree of Master in Naval Architecture and Marine Engineering.

32. Levésque, J.-B. and J. Lanteigne, *Influence des propriétés thermiques, des paramètres définissants l'apport énergétique et des paramètres numériques*, Institut de recherche d'Hydro-Québec.

33. Peckner, D. and I.M. Bernstein, *Handbook of stainless steels*. 1977: McGraw-Hill New York, NY.

34. Smithells, C.J., *Metals reference book*. Vol. 2. 1962: Butterworths.

35. Touloukian, Y.S. and D.P. DeWitt, *Thermophysical Properties of Matter-The TPRC Data Series. Volume 7. Thermal Radiative Properties-Metallic Elements and Alloys*, 1970, DTIC Document.

36. Lanteigne, J. and D.-A. Bouffard, and C. Baillageon, *Simulation du soudage par la méthode des éléments finis, Prédiction des distorsions et des contraines résidualles Partie 1. Validation théorique et expérimentale du module 'analyse thermique' du programme, IREQ,* 2002, IREQ: Varennes.

37. Whitaker, S. and S. Whitaker, *Fundamental principles of heat transfer*. Vol. 12. 1977: Pergamon Press New York.

38. Wahab, M.A., M. Painter, and M. Davies, *The prediction of the temperature distribution and weld pool geometry in the gas metal arc welding process*. Journal of Materials Processing Technology, 1998. **77**(1): p. 233-239.

39. Qureshi, M.E., *Analysis of Residual Stresses and Distortions in Circumferentially Welded Thin-Walled Cylinders*, 2008, National University of Sciences and Technology.

40. Rosenthal, D. *The theory of moving sources of heat and its application to metal treatments*. 1946. ASME.

41. Goldak, J.A. and M. Akhlaghi, *Computational Welding Mechanics*. 2005: Springer.
42. Cheng, W., *In-plane shrinkage strains and their effects on welding distortion in thin-wall structures*, 2005, The Ohio State University.

43. Paley, Z. and P. Hibbert, *Computation of temperatures in actual weld designs.* Welding journal, 1975. **54**(11): p. 385s-392s.

44. Eagar, T. and N. Tsai, *Temperature fields produced by traveling distributed heat sources.* Welding journal, 1983. **62**(12): p. 346-355.

45. Bass, M., *Laser materials processing*. Vol. 3. 1983: Elsevier.
46. Goldak, J., et al., *Computer modeling of heat flow in welds.* Metallurgical Transactions B, 1986. **17**(3): p. 587-600.

47. Yadaiah, N. and S. Bag, *Development of egg-configuration heat source model in numerical simulation of autogenous fusion welding process.* International Journal of Thermal Sciences, 2014. **86**(0): p. 125-138.

48. Ghosh, A., *Analytical Modeling of Moving Heat Source for GMAW.*

49. Abid, M. and M.J. Qarni, *3D thermal finite element analysis of single pass girth welded low carbon steel pipe-flange joints.* Turkish Journal of Engineering and Environmental Sciences, 2010. **33**(4): p. 281-294.

50. Nguyen, N., et al., *Analytical solutions for transient temperature of semi-infinite body subjected to 3-D moving heat sources.* WELDING JOURNAL-NEW YORK-, 1999. **78**: p. 265-s.

51. Rykalin, N., *The calculation of Thermal Processes in Welding.* 1951.

52. Westby, o., *Temperature distribution in the weld piece by welding*, in *Department of metallurgy and material working* 1968, Trondheim: Norway.

53. Klobčar, D., J. Tušek, and B. Taljat, *Finite element modeling of GTA weld surfacing applied to hot-work tooling.* Computational Materials Science, 2004. **31**(3): p. 368-378.

54. Casalino, G., et al. *FEM simulation of metal sheets laser welding with wire filler material*. in *Congress on Optics and Optoelectronics*. 2005. International Society for Optics and Photonics.

55. Reddy, A.A., B. Guha, and D. Achar, *Finite element modeling of three-dimensional transient heat transfer in stainless steel (304) pulsed GTA weldments.* Numerical Heat Transfer: Part A: Applications, 2002. **41**(1): p. 41-64.

56. Pavelic, V., et al., *Experimental and computed temperature histories in gas tungsten-arc welding of thin plates.* WELD J, 1969. **48**(7): p. 295.

57. Myers, P.S., O.A. Uyehara, and G. Borman, *Fundamentals of heat flow in welding.* Welding Research Council Bulletin, 1967(123): p. 1-&.

58. Lundbäck, A., *Finite element modelling and simulation of welding of aerospace components.* Luleå tekniska universitet, 2003. **27**.

59. Ohms, C., et al., *NET TG1: Residual stress assessment by neutron diffraction and finite element modeling on a single bead weld on a steel plate.* International Journal of Pressure Vessels and Piping, 2009. **86**(1): p. 63-72.

60. Folkhard, E. and G. Rabensteiner, *Welding metallurgy of stainless steels*. 1988: Springer.

61. *Alloy Digest-Data on World Wide Metals and Alloys*. 1972: ASM International.

62. Thibault, D., et al., *Reformed austenite transformation during fatigue crack propagation of 13% Cr–4% Ni stainless steel.* Materials Science and Engineering: A, 2011. **528**(21): p. 6519-6526.

63. Liu, Y.-R., et al., *Effect of heat treatment on microstructure and property of Cr13 super martensitic stainless steel.* Journal of Iron and Steel Research, International, 2011. **18**(11): p. 60-66.

64. Thibault, D., P. Bocher, and M. Thomas, *Residual stress and microstructure in welds of 13% Cr–4% Ni martensitic stainless steel.* Journal of Materials Processing Technology, 2009. **209**(4): p. 2195-2202.

65. Song, Y., et al., *The influence of tempering temperature on the reversed austenite formation and tensile properties in Fe–13% Cr–4% Ni–Mo low carbon martensite stainless steels.* Materials Science and Engineering: A, 2011. **528**(12): p. 4075-4079.

66. Song, Y., et al., *Anomalous phase transformation from martensite to austenite in Fe-13% Cr-4% Ni-Mo martensitic stainless steel.* Journal of Materials Science & Technology, 2010. **26**(9): p. 823-826.

67. ROBICHAUD, P. and S.À.L.F. OLIGOCYCLIQUE, *COMME EXIGENCE PARTIELLE À L'OBTENTION DE LA MAÎTRISE EN GÉNIE MÉCANIQUE M. Ing.*

68. E, F., *Welding metallurgy of stainless steel* Springer- Verlag, 1988.

69. Rajan, T. and A. Sharma, *Heat treatment: principles and techniques*. 2012: PHI Learning Pvt. Ltd.

70. Totten, G.E. and M.A. Howes, *Steel heat treatment handbook*. 1997: CRC Press.

71. Cook, R., et al., *Concepts and applications of finite element analysis.* 2002.

72. Vemanaboina, H., S. Akella, and R.K. Buddu, *Welding Process Simulation Model for Temperature and Residual Stress Analysis.* Procedia Materials Science, 2014. **6**: p. 1539-1546.